Numerical studies of thermal and compressible convection in rotating spherical shells: an application to the giant planets

Dissertation
zur Erlangung des Doktorgrades
der Mathematisch-Naturwissenschaftlichen Fakultäten
der Georg-August-Universität zu Göttingen

vorgelegt von
Denise Aida Tortorella
aus Buenos Aires (Argentinien)

Göttingen 2005

Bibliografische Information Der Deutschen Bibliothek

Die Deutsche Bibliothek verzeichnet diese Publikation in der Deutschen Nationalbibliografie; detaillierte bibliografische Daten sind im Internet über `http://dnb.ddb.de` abrufbar.

D7
Referent: Prof. Dr. Ulrich Christensen
Korreferent: Prof. Dr. Andreas Tilgner
Tag der mündlichen Prüfung: 5. Juli 2005

Copyright © Copernicus GmbH 2005

ISBN 3-936586-43-8

Copernicus GmbH, Katlenburg-Lindau
Druck: Schaltungsdienst Lange, Berlin

Printed in Germany

A mi familia de aquí y de allá.
Für meine Familie, hier und dort.

Non puoi insegnare niente a un uomo,
puoi solo aiutarlo a scoprirlo in sé stesso.

You cannot teach a man anything,
you can only help him to find it within himself.

Galileo Galilei

Contents

Motivation **15**

1 Thermal convection formulation in rotating spherical shells **19**
- 1.1 Fully compressible formulation . . . 19
- 1.2 Boussinesq approximation . . . 20
- 1.3 Anelastic approximation . . . 21
  - 1.3.1 Basic assumptions . . . 21
  - 1.3.2 Reference state . . . 23
- 1.4 Anelastic formulation with zero Grüneisen parameter . . . 27
  - 1.4.1 Scale separation and perturbation equations . . . 27
  - 1.4.2 Non-dimensional description . . . 30
  - 1.4.3 Non-dimensional linearised equations . . . 33
- 1.5 Numerical technique . . . 33
  - 1.5.1 Poloidal-toroidal decomposition . . . 33
  - 1.5.2 Code implementation . . . 35
  - 1.5.3 Testing the anelastic code . . . 35

2 Onset of convection **37**
- 2.1 Fundamentals on linear stability theory . . . 37
  - 2.1.1 Convective instability . . . 37
  - 2.1.2 Analytical description . . . 38
- 2.2 Onset of convection in rapidly rotating incompr. spherical systems . . 39
  - 2.2.1 Taylor-Proudman theorem . . . 39
  - 2.2.2 Asymptotic studies and style of convection . . . 39
- 2.3 Numerical marginal stability simulations for compressible fluids . . . 43
  - 2.3.1 Results for $\hat{\nu}$ constant, cases A and B . . . 44
  - 2.3.2 Results for $\hat{\mu}$ constant, cases C and D . . . 53
  - 2.3.3 Flow structure . . . 54
- 2.4 Summary and conclusions . . . 58

3 3D structure close to onset **59**
3.1 Reformulating the Taylor-Proudman theorem 59
3.2 Is the mass flux geostrophic? 60
3.3 Velocity vs. mass flux 62
3.4 Column bending 66
3.5 Summary and conclusions 71

4 Finite amplitude convection **73**
4.1 General features of incompressible convection 73
4.2 Supercritical compressible convection 74
4.2.1 Global measures of the solution 74
4.2.2 Starting conditions and numerical resolution 75
4.2.3 Numerical simulations 77
4.3 Flow structure in compressible convection 77
4.3.1 Weak compressibility 77
4.3.2 Intermediate to strong compressibility 81
4.4 Effects of depth dependent thermal diffusivity 85
4.5 Global properties of compressible convection 94
4.5.1 Constant dimensionless numbers, case A 94
4.5.2 Depth dependent thermal diffusivity, case BI 97
4.6 Tables with results 102
4.7 Summary and conclusions 104

Conclusions and perspectives **105**

A Fully compressible equations in spherical coordinates **109**
A.1 Continuity equation 109
A.2 Navier-Stokes equation 109
A.2.1 Viscous force 109
A.3 Energy equation 111
A.3.1 Viscous dissipation 111

B Anelastic approximation: Detailed scale analysis **113**
B.1 Equation of state 114
B.2 Continuity equation 114
B.3 Navier-Stokes equation 115
B.4 Energy equation 115

C Derivations in spectral space **117**
C.1 Viscous force 117
C.1.1 Preliminaries 117

C.1.2 $\hat{\nu}$ constant 117
C.1.3 $\hat{\mu}$ constant 118
C.2 Kinetic energy density 118

Bibliography **119**

Acknowledgements **127**

List of Figures

0.1 True colour mosaic of Jupiter, and black and white image of Saturn . 15
0.2 Zonal velocity vs. latitude after the Voyager missions 16

1.1 Sketch of the spherical shell model with its coordinates 20

2.1 Onset of convection in a rotating sphere according to Busse (1970) . . 40
2.2 Background density profile for different stratification degrees. 45
2.3 Modified critical Rayleigh number $Ra_c E^{4/3}$ vs. Co 47
2.4 Modified critical wave number $m_c E^{1/3}$ vs. Co 48
2.5 Modified critical oscillation frequency $\omega_c E^{2/3}$ vs. Co 49
2.6 Critical Rayleigh number Ra_c vs. Co for $\hat{\nu} = 1$ 50
2.7 Equatorial z-vorticity and temperature for $\hat{\nu} = 1$: cases A and BO . . 51
2.8 Equatorial z-vorticity and temperature for $\hat{\nu} = 1$: case BI 52
2.9 Equatorial z-vorticity and temperature for $\hat{\mu} = 1$: cases C and DO . . 55
2.10 Equatorial z-vorticity and temperature for $\hat{\mu} = 1$: case DI 55
2.11 Static conductive temperature profile T_s for different Co 57

3.1 Sketch of the spherical shell for a stratified fluid 61
3.2 Zonal flow for the velocity and the mass flux 62
3.3 Equatorial velocity and mass flux at $Ra = 1.1 Ra_c$: case A 64
3.4 Equatorial velocity and mass flux at $Ra = 1.1 Ra_c$: cases BI and BO . 65
3.5 Equatorial velocity and mass flux at $Ra = 1.1 Ra_c$: case C 65
3.6 Azimuthal average flow: case A 67
3.7 Azimuthal average flow: cases BO, C and DO 68
3.8 Column bending to the poles: case A 69
3.9 Column bending to the poles: cases BI and BO 70

4.1 Time-averaged spectrum of kinetic energy density 77
4.2 Time series for $Co = 0$ and $Co = 1.5$: case A 79
4.3 Equatorial z-vorticity for $Co = 0$ and $Co = 1.5$: case A 80
4.4 Meridional convective velocity for $Co = 0$ and $Co = 1.5$: case A . . . 81
4.5 North-polar views of radial velocity for $Co = 1.5$: case A 82
4.6 Time series for $Co = 3$ and $Co = 5$: case A 83

4.7 Equatorial z-vorticity for $Co = 3$ and $Co = 5$: case A 84
4.8 Meridional convective velocity for $Co = 3$ and $Co = 5$: case A 85
4.9 North-polar views of radial velocity for $Co = 3$ and $Co = 5$: case A . 86
4.10 Time series for $Co = 1.5$ and $Co = 3$: case BI 87
4.11 Equatorial z-vorticity for $Co = 1.5$ and $Co = 3$: case BI 88
4.12 Meridional convective velocity for $Co = 1.5$ and $Co = 3$: case BI . . . 89
4.13 Equatorial z-vorticity for $Co = 5$ at $Ra = 2.2Ra_c$: case BI 90
4.14 Time series for $Co = 5$: case BI 91
4.15 Equatorial z-vorticity for $Co = 5$ at $Ra = 4Ra_c$: case BI 92
4.16 Meridional slices of convective velocity for $Co = 5$: case BI 92
4.17 North-polar views of radial velocity for $Co = 1.5$ and $Co = 3$: case BI 93
4.18 North-polar views of radial velocity for $Co = 5$: case BI 93
4.19 Time-averaged $E_{tor}^{m=0}/E_k$ vs. Ra/Ra_c and E_{pol}/E_k vs. Ra/Ra_c: case A 95
4.20 Time-averaged $E_{tor}^{m=0}/E_k$ vs. Co and E_{pol}/E_k vs. Co: case A 95
4.21 Time-averaged Nu vs. Ra/Ra_c: case A 96
4.22 Time-averaged Nu vs. Co: case A 96
4.23 Time-averaged E_k vs. Ra/Ra_c: case A 98
4.24 Time-averaged E_k vs. Co: case A 98
4.25 Time-averaged $E_{tor}^{m=0}/E_k$ vs. Ra/Ra_c and E_{pol}/E_k vs. Ra/Ra_c: case BI 99
4.26 Time-averaged $E_{tor}^{m=0}/E_k$ vs. Co and E_{pol}/E_k vs. Co: case BI 99
4.27 Time-averaged Nu vs. Ra/Ra_c: case BI 100
4.28 Time-averaged Nu vs. Co: case BI 100
4.29 Time-averaged E_k vs. Ra/Ra_c: case BI 101
4.30 Time-averaged E_k vs. Co: case BI 101

List of Tables

1.1 Fluid properties symbols and their reference state expressions 25
1.2 Variation of dimensionless numbers with density stratification. 32

2.1 Values of shell density ratios $\hat{\rho}_i/\hat{\rho}_o$ associated to Co 45
2.2 Critical values for onset of convection for $\hat{\nu} = 1$ at $E = 1 \times 10^{-3}$ . . . 45
2.3 Critical values for onset of convection for $\hat{\nu} = 1$ at $E = 3 \times 10^{-4}$, *i)* . 46
2.4 Critical values for onset of convection for $\hat{\nu} = 1$ at $E = 3 \times 10^{-4}$, *ii)* . 46
2.5 Critical values for onset of convection for $\hat{\mu} = 1$, *i)* 53
2.6 Critical values for onset of convection for $\hat{\mu} = 1$, *ii)* 54

4.1 Resolution test for the compressible case 76
4.2 Time-averaged properties in the supercritical regime: Boussinesq case 102
4.3 Time-averaged properties in the supercritical regime: case A 103
4.4 Time-averaged properties in the supercritical regime: case BI 103

B.1 Order in ϵ for all quantities and operators 114

Motivation

The latitudinal banded appearance of the clouds in the uppermost atmosphere of Jupiter and Saturn (figure 0.1) is a surface manifestation of strong tropospheric zonal (east-west) winds (figure 0.2), as it was established after the observations by the Voyager missions in the 80's (Ingersoll et al., 1981; Limaye, 1986; Smith et al., 1981; Smith et al., 1982). The origin of these winds is controversial. One theory assumes that they are driven by absorbed sunlight in a shallow upper atmospheric layer (Williams, 1985) while the other assumes that they originate in the interior and are driven by thermal convection in the molecular hydrogen envelope (Busse, 1976; Busse, 1983). The in-situ measurements in Jupiter's atmosphere by the Galileo probe in the 90's give some credibility to the latter, showing that the wind speed do not vanish nor decrease below the cloud deck (Atkinson et al., 1998).

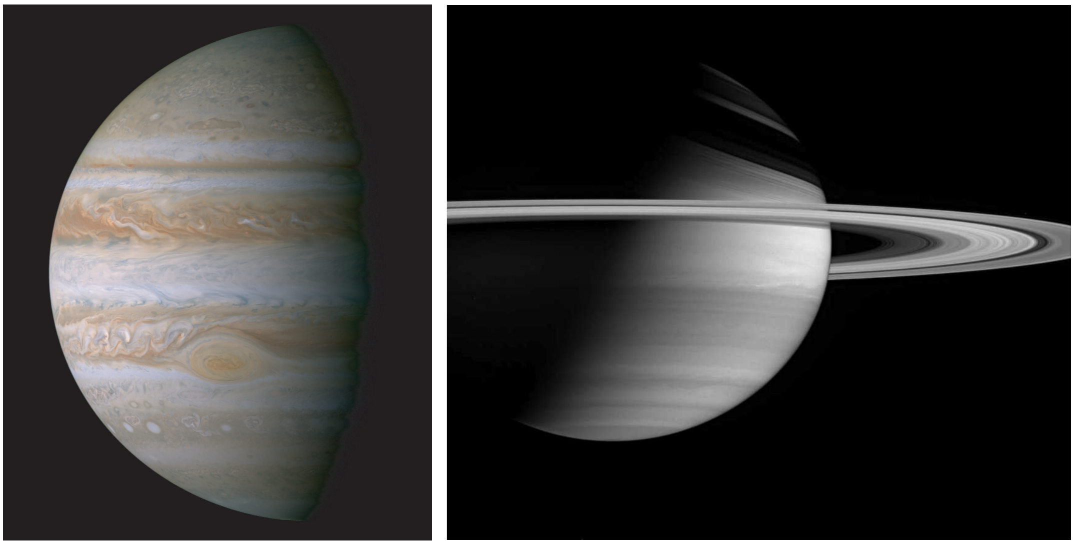

Fig. 0.1: Left: True colour mosaic of Jupiter constructed from images taken by the narrow angle camera on board Cassini spacecraft on December 29, 2000 during the closest approach at a distance of approximately 10 million kilometres.
Right: Image of Saturn taken with the Cassini spacecraft wide angle camera on January 23, 2005 at a distance of approximately 2.8 million kilometres.

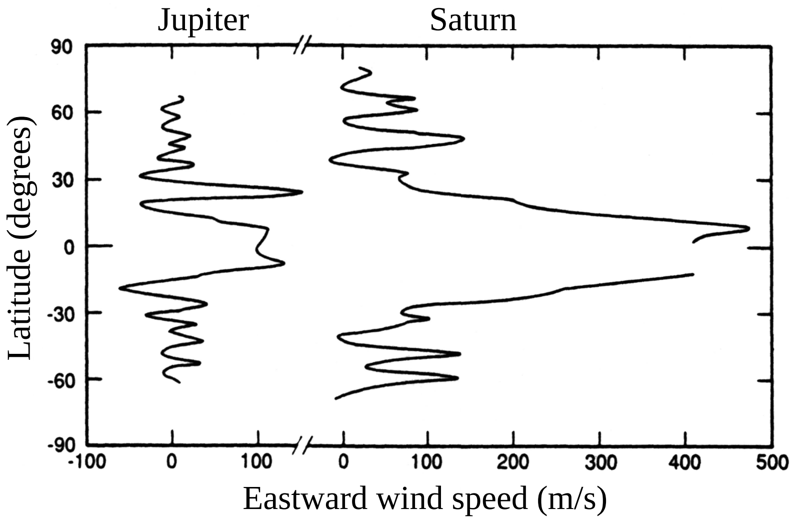

Fig. 0.2: Zonal velocity vs. latitude after the Voyager missions as given in Ingersoll (1990). The velocities were measured relative to the interior (System III) tracking features in the upper cloud layer.

Numerical simulations of thermal convection in rotating spherical shells applied to the giant planets succeeded in the generation and maintenance of zonal flow. However, the models present difficulties to reproduce the zonal winds as observed in the giant planets. For example, Christensen (2001) found strong alternating zonal wind but the number of bands were less than observed in Jupiter. Studies with different mechanical boundary conditions (Aurnou and Olson, 2001; Aurnou and Heimpel, 2004) showed that strong zonal flow is driven when both boundaries are mechanically stress-free although a non-slip condition at the inner boundary might be more adequate to model giant planets' dynamics (Starchenko and Jones, 2002).

The Boussinesq approximation was widely employed for this kind of simulations. It assumes that the fluid is incompressible but allows small density changes in the buoyancy force in order to retain convection. In the molecular hydrogen envelope the density increases inwards by about two orders of magnitude (Guillot et al., 1994a). Therefore, the Boussinesq models are certainly limited to describe the dynamics in the molecular envelope where density stratification is significant.

The anelastic approximation (Ogura and Phillips, 1962; Gough, 1969) provides a more realistic representation of a stratified fluid compared to the Boussinesq approximation while reducing the complexity of the fully compressible case. Its main advantage is that the effects of compressibility are retained while filtering out fast acoustic waves which would require a very small numerical time-step. Previous anelastic models have been focused in studies of mantle convection (e.g. Jarvis and McKenzie, 1980; Glatzmaier 1988; Bercovici et al., 1992) as well as thermal convection in the Sun (e.g. Gilman and Glatzmaier, 1981; Glatzmaier, 1984; Elliott et al., 2000; Miesch et al., 2000). However, these models do not describe adequately the physics of rapid rotating spherical systems as the giant planets.

The problem of thermal convection for a compressible fluid in rapidly rotating spherical systems has drawn little attention because of computational limitations as well as mathematical convenience. A few anelastic studies have been performed on the linear onset (Glatzmaier and Gilman, 1981a; Drew et al., 1995) while recent anelastic non-linear simulations were focused on applications to Jupiter's atmosphere but in the two-dimensional case (Evonuk and Glatzmaier, 2004). The study of this thesis is devoted to time-dependent, three-dimensional simulations in the linear and non-linear regime under the anelastic approximation in the limit of vanishing Grüneisen parameter. This limit simplifies the traditional anelastic approximation leading to a problem with a nearly unmodified temperature equation and the same number of non-linearities with respect to the Boussinesq case.

The structure of this thesis comprises four chapters, conclusions and three appendix sections. In chapter 1 the theoretical formulation of thermal convection for rotating spherical systems is presented. Special emphasis is put on the anelastic approximation with negligible Grüneisen parameter as well as the choice of the reference state. A study of linear onset for different fluid properties is given in chapter 2 while in chapter 3, the Taylor-Proudman theorem is reformulated to the compressible case. Results in the non-linear regime are presented in chapter 4 followed by the conclusions of the work and some additional theoretical details given in the appendix sections.

1 Thermal convection formulation in rotating spherical shells

1.1 Fully compressible formulation

The general equations describing thermal convection of a rotating compressible fluid are the starting point from which the assumptions of the anelastic or Boussinesq approximations will be done.

The spherical shell rotates at uniform angular velocity $\boldsymbol{\Omega}$ with respect to an inertial reference frame. The spherical coordinate system (r, θ, φ) describing radius, colatitude and longitude respectively of each fluid element in the shell is illustrated in Fig. 1.1.

The continuity equation

$$\frac{\partial \rho}{\partial t} + \boldsymbol{\nabla} \cdot (\rho \boldsymbol{u}) = 0 \ , \tag{1.1}$$

the Navier-Stokes equation

$$\rho\Big(\frac{\partial \boldsymbol{u}}{\partial t} + \underbrace{(\boldsymbol{u} \cdot \boldsymbol{\nabla})\boldsymbol{u}}_{inertia}\Big) = \underbrace{-\boldsymbol{\nabla} p}_{pressure\ grad.} + \underbrace{\rho \boldsymbol{g}}_{gravity} \underbrace{-2\rho\boldsymbol{\Omega} \times \boldsymbol{u}}_{Coriolis} + \underbrace{\boldsymbol{F}}_{friction} \ , \tag{1.2}$$

and the energy equation

$$\rho C_p\Big(\frac{\partial T}{\partial t} + \underbrace{\boldsymbol{u} \cdot \boldsymbol{\nabla} T}_{advection}\Big) \underbrace{-\alpha T\Big(\frac{\partial p}{\partial t} + \boldsymbol{u} \cdot \boldsymbol{\nabla} p\Big)}_{adiabatic\ heating} = \underbrace{\boldsymbol{\nabla} \cdot (k \boldsymbol{\nabla} T)}_{diffusion} + \underbrace{\Phi}_{viscous\ heating} \ , \tag{1.3}$$

describe the conservation of mass, momentum and internal energy, respectively. The symbols $\boldsymbol{u}$, p, T and $\boldsymbol{g}$ represent velocity, pressure, temperature and gravity acceleration fields respectively. The rest of the symbols, ρ, C_p, α and k, represent fluid properties, respectively, density, specific heat at constant pressure, thermal expansivity and thermal conductivity.

The observed polar flattening is $(6.5 \pm 0.1)\%$ for Jupiter (Hubbard, 1977) and $(8.8 \pm 0.8)\%$ for Saturn (Gehrels et al., 1980), values which are significant compared to 0.34% polar flattening for Earth. To keep the model geometrically simple, we explicitly ignore the centrifugal force, although if the density of the fluid is constant it can be proven that the centrifugal force becomes unimportant (e.g. Tritton, 1988).

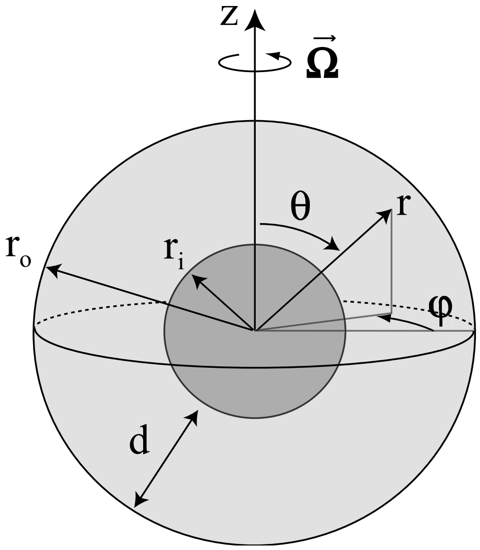

Fig. 1.1: Sketch of the spherical shell model with its coordinates.

The fluid is heated differentially with prescribed constant temperatures at the boundaries. Furthermore, there are no internal heat sources due to decay of radioactive elements.

A Newtonian fluid with zero bulk viscosity is assumed, so that the viscous force is given by

$$\boldsymbol{F} = \mu \boldsymbol{\nabla}^2 \boldsymbol{u} + \frac{1}{3}\mu \boldsymbol{\nabla}(\boldsymbol{\nabla} \cdot \boldsymbol{u}) + \boldsymbol{D}(\boldsymbol{\nabla}\mu, \boldsymbol{u}, \partial \boldsymbol{u}). \tag{1.4}$$

Here, μ is the dynamic or shear viscosity of the fluid, and $\boldsymbol{D}$ is a vector which components are given in (A.10) and depends on $\boldsymbol{\nabla}\mu$, velocity and their spatial derivatives.

The viscous heating Φ is a non-linear contribution whose expression can be found in §A.3.1 in Appendix A.

To complete the system of equations, a constitutive relation between p, T and ρ is needed as well as mechanical and thermal boundary conditions. For simplicity, we consider a perfect gas with equation of state

$$p = \rho R^* T \tag{1.5}$$

where R^* is the universal gas constant per unit mass.

1.2 Boussinesq approximation

Compressibility effects are neglected in the Boussinesq approximation and therefore the density is constant. However, in order to retain convection, some degree of density variation has to be allowed. The Boussinesq approximation thus, allows for small density variations due to temperature perturbations in the buoyancy term:

$$\rho = \rho_0\big(1 - \alpha(T - T_0)\big) = \rho_0 + \delta\rho \qquad (\delta\rho \ll \rho_0) \tag{1.6}$$

where ρ_0 and T_0 are the constant density and temperature reference values and $\delta\rho$ is the density perturbation. Density variations due to pressure perturbations are neglected in this approximation. Since relation (1.6) links density and temperature it may be considered as the equation of state for a Boussinesq fluid.
In the Boussinesq approximation the continuity equation (1.1) becomes

$$\boldsymbol{\nabla} \cdot \boldsymbol{u} = 0 \tag{1.7}$$

which describes the incompressible nature of the fluid. The general Navier-Stokes and energy equations (1.2) and (1.3) transform to

$$\rho_0\Big(\frac{\partial \boldsymbol{u}}{\partial t} + \underbrace{(\boldsymbol{u}\cdot\boldsymbol{\nabla})\boldsymbol{u}}_{inertia}\Big) = \underbrace{-\boldsymbol{\nabla} p}_{pressure\ grad.} + \underbrace{\delta\rho\boldsymbol{g}}_{buoyancy} \underbrace{-2\rho_0\boldsymbol{\Omega}\times\boldsymbol{u}}_{Coriolis} + \underbrace{\mu\boldsymbol{\nabla}^2\boldsymbol{u}}_{friction} \tag{1.8}$$

and

$$\rho_0 C_p\Big(\frac{\partial T}{\partial t} + \underbrace{\boldsymbol{u}\cdot\boldsymbol{\nabla} T}_{advection}\Big) = \underbrace{\boldsymbol{\nabla}\cdot(k\boldsymbol{\nabla} T)}_{diffusion}\ , \tag{1.9}$$

where in addition the dynamic viscosity μ was assumed constant leading to the usual expression for the viscous force. The definition of p here differs from the one in equation (1.2) although the symbol is the same[1]. The viscous and adiabatic heatings are negligible compared to the other terms in the energy equation (1.3) since the fluid is incompressible (see §1.3.2 for details).
The Boussinesq approximation does not imply any additional conditions other than incompressible fluid with small density variations in the buoyancy term. However, fluid properties like μ, k and C_p often are assumed to be constant to further simplify the problem. The details how this approximation applies to the general equations can be found in many textbooks (e.g. Tritton, 1988).

1.3 Anelastic approximation

1.3.1 Basic assumptions

The anelastic approximation lies somewhere between the fully compressible formalism and the Boussinesq approximation. It has been derived in slightly different ways by different authors, depending on the specific problem (Ogura and Phillips, 1962; Gough, 1969; Latour et al., 1976; Gilman and Glatzmaier, 1981; Braginsky and Roberts, 1995). Following Ogura and Phillips (1962) and Gough (1969), the basic assumptions are

---

[1] The definition of p in (1.8) is given by p in (1.2) $+\rho_0\Phi$, where $\boldsymbol{g} = -\boldsymbol{\nabla}\Phi$.

i) that the departures of the thermodynamic state variables due to convection are small with respect to a reference state, and

ii) that the short-period acoustic waves are filtered out.

Filtering out acoustic waves allows larger numerical time steps since the time scale of the fast acoustic waves is typically much smaller than the convective time scales. The strict elimination of acoustic waves forces the system to evolve on convective rather than acoustic time scales. It is formally realized by taking

$$\frac{\partial \rho'}{\partial t} = 0 \tag{1.10}$$

in the continuity equation, where ρ' represents density perturbations of the reference state.

The reference state is a background state against which perturbations due to convection are described. For simplicity it is generally assumed that it depends only on one spatial variable, which is the radius in spherical models or the depth in cartesian models. It may as well be explicitly time dependent.

In accordance to i), each thermodynamic state variable f is expressed as a sum of a spherically symmetric, time independent quantity $\widetilde{f}$ and a fluctuating quantity f':

$$\begin{aligned} \rho(r,\theta,\varphi,t) &= \widetilde{\rho}(r) + \rho'(r,\theta,\varphi,t), \\ p(r,\theta,\varphi,t) &= \widetilde{p}(r) + p'(r,\theta,\varphi,t), \\ T(r,\theta,\varphi,t) &= \widetilde{T}(r) + T'(r,\theta,\varphi,t). \end{aligned} \tag{1.11}$$

The separation of variables given in (1.11) is introduced in the general equations (1.1)–(1.3) to perform a formal scale analysis taking into account that $f'/\widetilde{f} = \epsilon \ll 1$. All the dependent variables are expanded in power series in ϵ and only terms up to the lowest order in ϵ are retained. As a result, the anelastic equations describing the evolution of the fluctuating (or dynamic) quantities can cope with large density variations preserving at the same time the non-linearities of the model.

In summary, the anelastic approximation lives on filtering out acoustic waves which are inherent in a compressible medium, as well as an adequate linearisation of the fluctuating thermodynamic variables about some appropriate state. The resulting equations can be solved numerically with larger time steps since fast acoustic waves are not present. The Boussinesq approximation suppresses acoustic waves as well but imposes in addition a constant density background, condition that is unsuitable for most geophysical problems where motions can extend over several scale heights. Moreover, the Boussinesq approximation neglects variations of density due to pressure perturbations, which are present in anelastic problems.

Particularly for the case of the giant planets' atmospheres, the density stratification is very high (Guillot et al., 1994a) since the pressure varies by more than six orders of magnitude from top to bottom (Stevenson, 1982; Guillot, 1999). Thus, anelastic models provide a more realistic representation of these systems than the Boussinesq ones.

1.3.2 Reference state

The giant planets' atmospheres are believed to be mostly convective (Hubbard, 1968; Stevenson and Salpeter, 1977; Chabrier et al., 1992; Guillot et al., 1994b). In a vigorously convecting system the superadiabaticity is very small since transport of heat due to convection is highly efficient. Thus, all current interior models of giant planets are obtained under the assumption of convective transport and adiabatic stratification (Guillot et al., 1994b). Therefore, a stratified adiabatic reference state seems to be the appropriate one to describe the equilibrium state of the fluid in the spherical shell.

The determination of our reference state requires the integration of the hydrostatic equilibrium equation

$$\frac{d\widetilde{p}(r)}{dr} = -\widetilde{\rho}(r)\widetilde{g}(r) \tag{1.12}$$

using the fact that for an ideal gas in an adiabatic state, density and pressure are related by

$$\widetilde{p}\widetilde{\rho}^{\,-\widetilde{\gamma}} = \text{const} = \widetilde{p}_o\widetilde{\rho}_o^{\,-\widetilde{\gamma}}. \tag{1.13}$$

The constant value is fixed with a value of $\widetilde{p}$ and $\widetilde{\rho}$ at certain radius. The choice of the outer boundary r_o, i.e. $\widetilde{p}_o = \widetilde{p}(r_o)$ and $\widetilde{\rho}_o = \widetilde{\rho}(r_o)$, is in principle arbitrary for our purpose. However, in general the structure of the giant planets' atmospheres is fixed by their specific entropy determined from observations at the surface of the planet (Saumon and Guillot, 2004) supporting our initial choice. As it will become evident later (e.g. Fig. 2.2), the chosen radius to define the constant value corresponds to a shell surface where the values of the Boussinesq reference state are recovered.

The relation (1.13) was obtained under the assumption that $\widetilde{\gamma}$, defined as the ratio of specific heats $\widetilde{C}_p/\widetilde{C}_v$, is constant. For diatomic gases like H_2 which is the major component of the giant planets' atmospheres, in ideal gas conditions, namely low temperatures and pressures, $\widetilde{\gamma} = 7/5$. This assumption certainly breaks down as soon as we move deep into the atmospheres, where the temperatures and pressures are very high and the fluid behaves progressively non-ideal.

To complete the specification of the reference state, all the necessary fluid properties such as $\widetilde{\alpha}$, $\widetilde{k}$, $\widetilde{C}_p$, $\widetilde{\chi}_T$, etc., which may be a function of radius, have to be given in a consistent way (see Table 1.1).

Prescribing the gravity background $\widetilde{g}(r)$ as a constant value g, the integration of (1.12) using the expression of $\widetilde{\rho}(\widetilde{p}, \widetilde{p}_o, \widetilde{\rho}_o, \widetilde{\gamma})$ resulting from (1.13) leads to

$$\begin{aligned} \widetilde{\rho}(r) &= \widetilde{\rho}_o\Big(1+\frac{\widetilde{\gamma}-1}{\widetilde{\gamma}}\frac{g}{R^*\widetilde{T}_o}(r_o-r)\Big)^{\left(\frac{1}{\widetilde{\gamma}-1}\right)} \\ \widetilde{p}(r) &= \widetilde{p}_o\Big(1+\frac{\widetilde{\gamma}-1}{\widetilde{\gamma}}\frac{g}{R^*\widetilde{T}_o}(r_o-r)\Big)^{\left(\frac{\widetilde{\gamma}}{\widetilde{\gamma}-1}\right)} \\ \widetilde{T}(r) &= \widetilde{T}_o\Big(1+\frac{\widetilde{\gamma}-1}{\widetilde{\gamma}}\frac{g}{R^*\widetilde{T}_o}(r_o-r)\Big) \end{aligned} \qquad (1.14)$$

where the ideal gas equation of state $\widetilde{p} = \widetilde{\rho}R^*\widetilde{T}$ was used.

Taking advantage of some conventional thermodynamic parameters we can reformulate the previous relations into

$$\begin{aligned} \widetilde{\rho}(r) &= \widetilde{\rho}_o\Big(1+Co\varGamma\frac{(r_o-r)}{d}\Big)^{\left(\frac{1}{\varGamma}\right)} \\ \widetilde{p}(r) &= \widetilde{p}_o\Big(1+Co\varGamma\frac{(r_o-r)}{d}\Big)^{\left(\frac{\varGamma+1}{\varGamma}\right)} \\ \widetilde{T}(r) &= \widetilde{T}_o\Big(1+Co\varGamma\frac{(r_o-r)}{d}\Big) \end{aligned} \qquad (1.15)$$

where $\varGamma$ is the Grüneisen parameter, Co is the compressibility parameter, both non-dimensional, and $d = r_o - r_i$ is the shell thickness.

The Grüneisen parameter $\varGamma$ is defined as

$$\varGamma = \frac{1}{\widetilde{\rho}\widetilde{C}_v}\Big(\frac{\partial\widetilde{p}}{\partial\widetilde{T}}\Big)_v = \frac{\widetilde{\alpha}}{\widetilde{\rho}\widetilde{C}_v\widetilde{\chi}_T} = \frac{\widetilde{p}}{\widetilde{T}\widetilde{\rho}\widetilde{C}_v} = \frac{R^*}{\widetilde{C}_v} = \widetilde{\gamma}-1. \qquad (1.16)$$

The definition on the left of (1.16) shows that $\varGamma$ measures the increase of pressure with temperature (while volume is held constant) and therefore $\varGamma$ is a measure of thermal effects.

The non-dimensional Dissipation number Di defined as

$$Di = \frac{\widetilde{\alpha}gd}{\widetilde{C}_p} = \frac{\widetilde{\gamma}-1}{\widetilde{\gamma}}\frac{gd}{R^*\widetilde{T}} \qquad (1.17)$$

links the compressibility parameter Co and $\varGamma$ in the following way:

$$Co = \frac{Di}{\varGamma} = \frac{1}{\widetilde{\gamma}}\frac{gd}{R^*\widetilde{T}} \qquad (1.18)$$

where the Dissipation number Di_o defined at the outer boundary has to be used in (1.18) to rewrite (1.14) into (1.15). The choice of the outer boundary to fix the

Symbol	Fluid property	Ideal gas expression	Dimensionless expression in the reference state
ρ	Density	p/R^*T	$\hat{\rho} =$ see (1.23)
μ	Dynamic viscosity: $\rho\nu$		a) 1 ; b) $\hat{\rho}$
ν	Kinematic viscosity		a) $1/\hat{\rho}$; b) 1
k	Thermal conductivity: $\kappa\rho C_p$		c) 1 ; d) $\hat{\rho}$
κ	Thermal diffusivity		c) $1/\hat{\rho}$; d) 1
α	Thermal expansivity: $-\frac{1}{\rho}\left(\frac{\partial\rho}{\partial T}\right)_p$	$1/T$	1
χ_T	Isothermal compressibility: $\frac{1}{\rho}\left(\frac{\partial\rho}{\partial p}\right)_T$	$1/p$	$1/\hat{\rho}$
Γ	Grüneisen parameter: $\frac{1}{\rho C_v}\left(\frac{\partial p}{\partial T}\right)_v$	$\gamma - 1$	0
C_p	Specific heat at constant pressure	$\frac{\gamma}{\gamma-1}R^*$	1
C_v	Specific heat at constant volume	$\frac{R^*}{\gamma-1}$	1
γ	$C_p/C_v = 1 + \alpha\Gamma T$		1

Table 1.1: Definition of fluid properties symbols and their expression in the reference state for the simplified anelastic approximation (case III in the following page). Any dimensionless reference state variable $\hat{f}$ is obtained by $\widetilde{f}/\widetilde{f}_o$.

constant value in (1.13) fixed as well the same level for Di in (1.15).

The Dissipation number Di is a measure of thermal effects due to compressibility, namely, adiabatic heating and viscous heating (Christensen and Yuen, 1985; Schmeling, 1989). Since both effects are scaled with the same dimensionless number, both terms are neglected in the temperature equation (1.3) when $Di = 0$, as it is the case in the Boussinesq approximation. Furthermore, Di is a ratio between two length scales: the thickness of the shell d as the characteristic convection length scale of the system, and the temperature scale height H_T defined as

$$H_T = \left(\frac{1}{\widetilde{T}}\left|\frac{d\widetilde{T}}{dr}\right|\right)^{-1} = \frac{\widetilde{\gamma}R^*\widetilde{T}}{(\widetilde{\gamma}-1)g} = \frac{\widetilde{C}_p}{g\widetilde{\alpha}} \tag{1.19}$$

as the vertical (or radial) distance over which a parcel of fluid must be moved in order to change its reference temperature by adiabatic expansion or compression by a factor of e. When

$$Di = \frac{d}{H_T} \ll 1 \tag{1.20}$$

the region where convection can develop has nearly constant reference temperature and thus, since there is no basic temperature stratification, viscous and adiabatic heatings which are a consequence of the thermal stratification due to compressibility are negligible in the convecting region.

The compressibility parameter Co, on the other hand, is a measure of the mechanical effects due to compressibility, namely, the density stratification. Similarly as Di, Co

is a ratio between d, and the density scale height H_ρ defined as

$$H_\rho = \left(\frac{1}{\widetilde{\rho}} \left| \frac{d\widetilde{\rho}}{dr} \right| \right)^{-1} = \frac{\widetilde{\gamma} R^* \widetilde{T}}{g}. \tag{1.21}$$

When

$$Co = \frac{d}{H_\rho} \ll 1 \tag{1.22}$$

the region where convection can develop has nearly constant density background and thus, since there is no basic density stratification, the continuity equation in (1.1) simplifies to $\boldsymbol{\nabla} \cdot \boldsymbol{u} = 0$. This simplified continuity equation is characteristic for a system with constant density, as in the Boussinesq approximation.

Approximations resulting from *Co* and *Di*

The values or asymptotic limits of Co and Di, which univocally establish the value or asymptotic limit of $\mathit{\Gamma}$ through (1.18), determine whether the Boussinesq approximation or the anelastic approximation is valid. Between them, there are two intermediate cases of particular interest.

I)	Boussinesq approximation:	$Co \to 0$,	$Di \to 0$,	$\Gamma > 0$
II)	Extended Boussinesq approximation:	$Co \to 0$,	$Di > 0$,	$\Gamma \to \infty$
III)	Simplified anelastic approximation:	$Co > 0$,	$Di \to 0$,	$\Gamma \to 0$
IV)	Anelastic approximation:	$Co > 0$,	$Di > 0$,	$\Gamma > 0$

In the cases I) and II) as it was previously explained there is no density stratification or it is negligible in the convecting region, leading to the classical condition of incompressibility $\boldsymbol{\nabla} \cdot \boldsymbol{u} = 0$. However, in II) the reference temperature is stratified since $Di > 0$ and therefore, the adiabatic and viscous heatings, referred in the literature as "non-boussinesq effects", have to be taken into account in the energy equation.

In the cases III) and IV) the density stratification is not negligible and as a consequence $\boldsymbol{\nabla} \cdot \boldsymbol{u} \neq 0$. However, in the case III), since $Di \to 0$ or equally said $\mathit{\Gamma} \to 0$, the adiabatic and viscous heatings can be neglected leading to a similar temperature equation as in the Boussinesq case.

The extended Boussinesq approximation has been applied to study Earth mantle convection (Schmeling, 1989; Steinbach et al., 1989; Steinbach and Yuen, 1998). Since the density of silicates increases by 60% from the top to the bottom (taking into account phase and compositional changes) (Dziewonski and Anderson, 1981), the density stratification of Earth mantle is moderate to slight. Furthermore, the latent heat effects of phase transitions scale also with Di (Christensen and Yuen, 1985), and therefore, the "non-boussinesq effects" including the phase transitions can be

studied ignoring the effects of density changes except in the gravity term.
Considering the simplified anelastic approximation, there has been no work published yet. Its main advantage is that the effects of compressibility arising from the density stratification can be studied in an isothermal rather than adiabatic reference state. Thus, the amount of non-linearities in the problem remains the same as in the Boussinesq case (recall that the viscous and adiabatic heatings are non-linear terms in the temperature equation (1.3)).
Since gas giant planets' atmospheres display high density stratification, the simplified anelastic approximation seems to provide an appropriate starting model to study compressible thermal convection in these systems.

Reference state for the simplified anelastic approximation

The hydrostatic, adiabatic reference state (1.15) is valid for any arbitrary, finite Co and Γ. Taking the asymptotic limit $\Gamma \to 0$, the dimensionless reference state for the simplified anelastic approximation yields

$$\hat{\rho} = \frac{\widetilde{\rho}}{\widetilde{\rho}_o} = \exp\left(Co\frac{(r_o - r)}{d}\right) \quad , \quad \hat{p} = \frac{\widetilde{p}}{\widetilde{p}_o} = \exp\left(Co\frac{(r_o - r)}{d}\right) \quad , \quad \hat{T} = \frac{\widetilde{T}}{\widetilde{T}_o} = 1, \tag{1.23}$$

which corresponds to an isothermal state with exponential density variation. The Boussinesq reference state

$$\hat{\rho} = \frac{\widetilde{\rho}}{\widetilde{\rho}_o} = 1 \quad , \quad \hat{p} = \frac{\widetilde{p}}{\widetilde{p}_o} = 1 \quad , \quad \hat{T} = \frac{\widetilde{T}}{\widetilde{T}_o} = 1. \tag{1.24}$$

is recovered taking $Co = 0$ in (1.23).

1.4 Anelastic formulation with zero Grüneisen parameter

1.4.1 Scale separation and perturbation equations

One of the assumptions imposed in the anelastic approximation is that the fluctuations due to convection are much smaller than the reference state. In other words, the anelastic approximation lives on the assumption that two different scale sizes coexist in the system making possible the explicit separation of the spherically symmetric state from its perturbations.
Gilman and Glatzmaier (1981) performed the formal scale analysis on the fully compressible equations for a rotating spherical shell for solar applications. Braginsky and Roberts (1995) did formally a similar scale analysis for the case of the Earth's

outer core. In both cases, the reference state was adiabatic and no further assumptions were done on the Grüneisen parameter $\mathit{\Gamma}$ resulting in the usual equations for the anelastic approximation.

The scale separation as given in (1.11) can also be expressed in terms of a small parameter ϵ taken as a measure of the relative magnitude of the perturbations $\epsilon = f'/\widetilde{f} \ll 1$. Gilman and Glatzmaier (1981) considered ϵ as the measure of the slight superadiabaticity of the fluid. Since departures from the adiabatic temperature gradient are responsible for driving the global convection, they stated that this definition of ϵ should also be a measure of the relative magnitude of the perturbations:

$$\epsilon \approx \frac{\rho'}{\widetilde{\rho}} \approx \frac{p'}{\widetilde{p}} \approx \frac{T'}{\widetilde{T}} \ll 1. \tag{1.25}$$

Following Gough (1969), and Gilman and Glatzmaier (1981) another interpretation to ϵ is given by

$$\epsilon \approx \frac{u^2}{{c_s}^2} = Ma^2 \tag{1.26}$$

where u is the characteristic convective velocity, c_s is the characteristic adiabatic sound speed and Ma is the Mach number. Then, as (1.26) suggests, $\epsilon \ll 1$ is achieved when the characteristic convective velocities are subsonic.

Characteristic convective velocities estimated from the convective flux are of the order $0.1ms^{-1}$ for Jupiter's molecular hydrogen envelope (Guillot et al., 2004). However, at the surface, the characteristic velocities are much larger reaching values of the order of $120ms^{-1}$ for the zonal winds (Ingersoll et al., 1981). Characteristic values of the sound speed c_s for Jupiter are $1200 - 1500ms^{-1}$ at $10 - 100bar$, which correspond to the uppermost region of its molecular hydrogen envelope (Lorenz, 1999). Since for an ideal gas the adiabatic and isothermal sound speeds are related as $c_s = \sqrt{\gamma}c_T$, with $\gamma = 7/5 = 1.4$ for a diatomic gas, it results $c_s \sim c_T$. Taking $1500ms^{-1}$ as a representative value of c_T gives an estimate of $\epsilon \sim 6 \times 10^{-3}$ taking $120ms^{-1}$ at the surface as characteristic velocity. Taking $u \sim 0.1ms^{-1}$ gives $\epsilon \sim 10^{-9}$, estimate which is even smaller in deeper atmospheric regions since sound velocities are larger (Duffy et al., 1994).

Provided that the fluid motions cause only small departures from the reference state, the equation of state may be written as a linear expansion of ρ about the reference state $\widetilde{\rho}$ in the following way:

$$\begin{aligned}
\rho = \widetilde{\rho}(\widetilde{p},\widetilde{T}) + \rho' &= \widetilde{\rho}(\widetilde{p},\widetilde{T}) + \widetilde{\left(\frac{\partial \rho}{\partial p}\right)}_T p' + \widetilde{\left(\frac{\partial \rho}{\partial T}\right)}_p T' \\
&= \widetilde{\rho}(\widetilde{p},\widetilde{T}) + \widetilde{\rho}\widetilde{\chi}_T p' - \widetilde{\rho}\widetilde{\alpha}T' \\
&= \widetilde{\rho}(\widetilde{p},\widetilde{T}) + \widetilde{\rho}\frac{p'}{\widetilde{p}} - \widetilde{\rho}\frac{T'}{\widetilde{T}_o}
\end{aligned} \tag{1.27}$$

from which arises that

$$\frac{\rho'}{\widetilde{\rho}} \approx \frac{p'}{\widetilde{p}} \approx \frac{T'}{\widetilde{T}_o} \approx \epsilon. \tag{1.28}$$

To obtain the perturbation equations the dependent variables are expanded in power series of ϵ and the resulting expansion is introduced in the fully compressible formalism. The terms ordered ϵ^0 give the reference state equations while the terms up to the next lowest order in ϵ give the perturbation equations. We ignore perturbations in the diffusivities, i.e. ν' and κ', since the uncertainty in these fluid properties is great (Gilman and Glatzmaier, 1981). The details of the scale analysis and the derivation of the perturbation equations are given in Appendix B.

The continuity equation (1.1), Navier-Stokes equation (1.2) and energy equation (1.3) take respectively the following form in the simplified anelastic approximation:

$$\boldsymbol{\nabla} \cdot (\widetilde{\rho}\boldsymbol{u}) = 0, \tag{1.29}$$

$$\widetilde{\rho}\Big(\frac{\partial \boldsymbol{u}}{\partial t} + \big(\boldsymbol{u} \cdot \boldsymbol{\nabla}\big)\boldsymbol{u}\Big) = -\boldsymbol{\nabla} p' + \rho'\widetilde{\boldsymbol{g}} + \widetilde{\rho}\boldsymbol{g'} - 2\widetilde{\rho}\boldsymbol{\Omega} \times \boldsymbol{u} + \boldsymbol{F}_a, \tag{1.30}$$

and

$$\widetilde{\rho}C_p\Big(\frac{\partial T'}{\partial t} + \boldsymbol{u} \cdot \boldsymbol{\nabla} T'\Big) = \boldsymbol{\nabla}\big(\widetilde{k}\boldsymbol{\nabla} T'\big), \tag{1.31}$$

where $\boldsymbol{F}_a$ is the viscous force given by

$$\boldsymbol{F}_a = \widetilde{\mu}\boldsymbol{\nabla}^2\boldsymbol{u} + \frac{1}{3}\widetilde{\mu}\boldsymbol{\nabla}(\boldsymbol{\nabla} \cdot \boldsymbol{u}) + \frac{d\widetilde{\mu}}{dr}\left[\frac{1}{r}\boldsymbol{\nabla}(ru_r) + r\frac{\partial}{\partial r}\Big(\frac{\boldsymbol{u}}{r}\Big) - \frac{2}{3}(\boldsymbol{\nabla} \cdot \boldsymbol{u})\hat{r}\right]. \tag{1.32}$$

The continuity equation (1.29) resembles the Boussinesq continuity equation (1.7) but with the mass-flux field $\widetilde{\rho}\boldsymbol{u}$ instead of the velocity field $\boldsymbol{u}$. The resemblance between the energy equation (1.31) and its Boussinesq counterpart (1.9) is a consequence of neglecting Γ. Without this assumption, the viscous and adiabatic heatings would have remained in the anelastic energy equation (see §B.4 for further discussion).

Inserting in (1.30) the expression of ρ' given in the linearised equation of state (1.27) we obtain

$$\widetilde{\rho}\Big(\frac{\partial \boldsymbol{u}}{\partial t} + \big(\boldsymbol{u} \cdot \boldsymbol{\nabla}\big)\boldsymbol{u}\Big) = -\boldsymbol{\nabla} p' + \underbrace{\widetilde{\rho}\widetilde{\chi}_T p'\widetilde{\boldsymbol{g}} - \widetilde{\rho}\widetilde{\alpha}T'\widetilde{\boldsymbol{g}}}_{buoyancy} + \widetilde{\rho}\boldsymbol{g'} - 2\widetilde{\rho}\boldsymbol{\Omega} \times \boldsymbol{u} + \boldsymbol{F}_a \tag{1.33}$$

which contains buoyancy due to temperature and pressure perturbations. The Navier-Stokes equation given in this way can be rewritten following Braginsky and Roberts (1995). They introduced a "reduced pressure" P defined as

$$P = \frac{p' + \widetilde{\rho}\Phi'}{\widetilde{\rho}} \tag{1.34}$$

where $\boldsymbol{g'} = -\boldsymbol{\nabla}\Phi'$. The pressure defined in this way transforms (1.33) in

$$\widetilde{\rho}\Big(\frac{\partial \boldsymbol{u}}{\partial t} + \big(\boldsymbol{u}\cdot\boldsymbol{\nabla}\big)\boldsymbol{u}\Big) = -\widetilde{\rho}\boldsymbol{\nabla}P - \widetilde{\rho}\widetilde{\alpha}T'\widetilde{\boldsymbol{g}} - 2\widetilde{\rho}\boldsymbol{\Omega}\times\boldsymbol{u} + \boldsymbol{F}_a \tag{1.35}$$

making use of $\boldsymbol{\nabla}\widetilde{\rho} = \frac{\boldsymbol{\nabla}\widetilde{p}}{c_T^2}$ with $c_T^2 = R^*\widetilde{T}_o$.

The remarkable point in Braginsky and Roberts' pressure-transformation is that the buoyancy force associated with pressure variations does not contribute explicitly, leading to an anelastic Navier-Stokes equation which resembles the Boussinesq counterpart (1.8).

1.4.2 Non-dimensional description

The Navier-Stokes equation (1.35) and the energy equation (1.31) will be solved numerically in non-dimensional form with the constraint (1.29) of solenoidal mass flux. The gravity is assumed constant, i.e. $\widetilde{\boldsymbol{g}} = -g\hat{\boldsymbol{r}}$. The dimensionless reference density $\hat{\rho}$ is given in (1.23). Using the shell thickness d as length scale, $d^2/\widetilde{\nu}_o$ as time scale, the temperature contrast ΔT between the inner and the outer boundary as temperature scale and $\widetilde{\rho}_o$ as density scale we obtain:

$$\boldsymbol{\nabla}\cdot(\hat{\rho}\boldsymbol{u}) = 0, \tag{1.36}$$

$$E\Big(\frac{\partial \boldsymbol{u}}{\partial t} + \underbrace{(\boldsymbol{u}\cdot\boldsymbol{\nabla})\boldsymbol{u}}_{inertia}\Big) = \underbrace{-\boldsymbol{\nabla}P}_{pressure\ grad.} + \underbrace{\frac{RaE}{Pr}T\hat{\boldsymbol{r}}}_{buoyancy} \underbrace{-2\hat{\boldsymbol{z}}\times\boldsymbol{u}}_{Coriolis} + \underbrace{E\boldsymbol{F}_v}_{friction}, \tag{1.37}$$

and

$$Pr\hat{\rho}\Big(\frac{\partial T}{\partial t} + \underbrace{\boldsymbol{u}\cdot\boldsymbol{\nabla}T}_{advection}\Big) = \underbrace{\boldsymbol{\nabla}(\hat{k}\boldsymbol{\nabla}T)}_{diffusion} \tag{1.38}$$

where $\hat{k}$ is related to $\hat{\rho}$ according to (1.41).

$\boldsymbol{F}_v$ in the viscous force in (1.37) is given by

$$\boldsymbol{F}_v = \frac{1}{\hat{\rho}}\left[\hat{\mu}\boldsymbol{\nabla}^2\boldsymbol{u} + \frac{1}{3}\hat{\mu}\boldsymbol{\nabla}(\boldsymbol{\nabla}\cdot\boldsymbol{u}) + \frac{d\hat{\mu}}{dr}\left[\frac{1}{r}\boldsymbol{\nabla}(ru_r) + r\frac{\partial}{\partial r}\Big(\frac{\boldsymbol{u}}{r}\Big) - \frac{2}{3}(\boldsymbol{\nabla}\cdot\boldsymbol{u})\hat{r}\right]\right] \tag{1.39}$$

where $\hat{\mu}$ is related to $\hat{\rho}$ according to (1.40). From here on (except in Appendix B) the primes are omitted for clarity.

The temperature contrast ΔT between inner and outer boundary is set to 1. The subscript "o" indicates in all cases the value at the outer boundary, which is 1 for dimensionless variables and dimensionless fluid properties.

The equations in non-dimensional form introduce three dimensionless numbers that act as control parameters of the model. They are

$$\begin{aligned} \text{Rayleigh number:} \qquad Ra &= \frac{g\alpha\Delta T d^3}{\widetilde{\nu}_o\widetilde{\kappa}_o} \\ \text{Ekman number:} \qquad E &= \frac{\widetilde{\nu}_o}{\Omega d^2} \\ \text{Prandtl number:} \qquad Pr &= \frac{\widetilde{\nu}_o}{\widetilde{\kappa}_o} \end{aligned}$$

The Rayleigh number represents a measure of the strength of the buoyancy force. It is defined as the ratio of the factors driving convection relative to the ones that inhibit it. Ra determines not only the strength of convection but also its occurrence: convection starts when the Rayleigh number reaches a threshold value called the critical Rayleigh number Ra_c. When $Ra < Ra_c$ the heat is transported only by conduction, when $Ra > Ra_c$ also by convection. The Ekman number is the ratio of viscous to Coriolis forces and therefore is a measure of the effects of viscosity relative to rotation. The Prandtl number depends only on fluid properties and indicates the relative importance between viscous and thermal diffusion.

Together with these three numbers we have to indicate the degree of density stratification which is given by Co as previously discussed. Co is usually a function of radius, however the assumptions of vanishing Γ and gravity constant results in Co constant throughout the shell as follows from (1.18).

The dimensionless reference shear viscosity $\hat{\mu}$ is related to $\hat{\rho}$ through the dimensionless reference kinematic viscosity $\hat{\nu}$ by

$$\hat{\nu} = \frac{\hat{\mu}}{\hat{\rho}}. \tag{1.40}$$

Similarly, the dimensionless reference thermal conductivity $\hat{k}$ is related to $\hat{\rho}$ through the dimensionless reference thermal diffusivity $\hat{\kappa}$ by

$$\hat{\kappa} = \frac{\hat{k}}{\hat{\rho}C_p}. \tag{1.41}$$

We have the freedom to choose the profile of one of the two fluid properties related to $\hat{\rho}$ in (1.40) and in (1.41). We will consider four possible cases:

	$\hat{\kappa}$ = const	$\hat{k}$ = const
$\hat{\nu}$ = const	Case A	Case B
$\hat{\mu}$ = const	Case C	Case D

The dimensionless numbers as previously given are defined according to the values of the diffusivities at the outer boundary. When one or both diffusivities are radially

Case	Ra	E	Pr
A	$\frac{g\alpha\Delta T d^3}{\nu\kappa}$	$\frac{\nu}{\Omega d^2}$	$\frac{\nu}{\kappa}$
B	$\frac{\widetilde{\rho} g\alpha\Delta T d^3 C_p}{\nu k}$	$\frac{\nu}{\Omega d^2}$	$\widetilde{\rho} C_p \frac{\nu}{k}$
C	$\frac{\widetilde{\rho} g\alpha\Delta T d^3}{\mu\kappa}$	$\frac{\mu}{\widetilde{\rho}\Omega d^2}$	$\frac{\mu}{\widetilde{\rho}\kappa}$
D	$\frac{\widetilde{\rho}^2 g\alpha\Delta T d^3 C_p}{\mu k}$	$\frac{\mu}{\widetilde{\rho}\Omega d^2}$	$\frac{\mu}{k} C_p$

Table 1.2: Variation of dimensionless numbers with density stratification.

dependent, the dimensionless numbers will have a different value throughout the shell depending on the radius chosen to define them. Therefore, they change locally with radius in a fashion that depends on the case to study as table 1.2 shows.

The case A is particularly important since every dimensionless number does not change across the shell. In the case B Pr increases towards the interior while in the case C its behaviour is opposite. In the cases C and D, the local Ekman number decreases inwards but Pr does not change across the shell in the case D.

Further simplifications can be applied to the equations (1.37) and (1.38) assuming that $\hat{\mu}$ or $\hat{k}$ are constant. The assumption of $\hat{\mu}$ constant leads to a viscous force in which the terms including the gradient of $\hat{\mu}$ in $\boldsymbol{F}_v$ vanish:

$$\boldsymbol{F}_v = \frac{1}{\hat{\rho}}\Big[\boldsymbol{\nabla}^2\boldsymbol{u} + \frac{1}{3}\boldsymbol{\nabla}(\boldsymbol{\nabla}\cdot\boldsymbol{u})\Big], \tag{1.42}$$

The assumption of $\hat{k}$ constant leads to an energy equation that reads

$$Pr\hat{\rho}\Big(\frac{\partial T}{\partial t} + \boldsymbol{u}\cdot\boldsymbol{\nabla}T\Big) = \nabla^2 T. \tag{1.43}$$

Boundary conditions

The fluid cannot flow beyond r_i and r_o in the radial direction, condition known as "non-penetration". In the tangential direction, we impose the stress-free (or free-slip) condition. These two conditions can be summarised as

$$u_r = 0 \quad \text{and} \quad \tau_{r\theta} = \tau_{r\varphi} = 0 \quad \text{at} \quad r_i \equiv \frac{\eta}{1-\eta} \quad \text{and} \quad r_o \equiv \frac{1}{1-\eta} \tag{1.44}$$

where $\eta = r_i/r_o$, and $\tau_{r\theta}$ and $\tau_{r\varphi}$ are given in §A.2.1 taking $\hat{\mu}$ instead of μ.

The stress-free condition is appropriate at the outer boundary while at the inner boundary, a non-slip condition might be more adequate to model giant planets (Starchenko and Jones, 2002). Modelling with non-slip boundary condition introduces to the problem boundary layers, whose influence was studied for the Boussinesq case by Zhang (1993). To keep the model simple we consider in our studies

both boundaries mechanically stress-free.
The temperature at the boundaries is prescribed such that $T_i = 1$ at r_i and $T_o = 0$ at r_o.

1.4.3 Non-dimensional linearised equations

Under the assumption that at onset of convection the dependent variables undergo infinitesimal disturbances, the non-linear terms can be neglected since they are of higher order in disturbances. Additionally, reformulating the problem in terms of $\Theta = T - T_s$, the deviation of temperature T from the conductive static temperature profile T_s, the non-dimensional linearised equations governing perturbations to the basic state are:

$$E\frac{\partial \boldsymbol{u}}{\partial t} = -\boldsymbol{\nabla} P + \frac{RaE}{Pr}\Theta\hat{\boldsymbol{r}} - 2\hat{\boldsymbol{z}} \times \boldsymbol{u} + E\boldsymbol{F}_v \tag{1.45}$$

and

$$Pr\hat{\rho}\frac{\partial \Theta}{\partial t} = -u_r\frac{dT_s}{dr} + \boldsymbol{\nabla}\big(\hat{k}\boldsymbol{\nabla}\Theta\big) \tag{1.46}$$

together with the constraint of solenoidal mass flux (1.36).

1.5 Numerical technique

1.5.1 Poloidal-toroidal decomposition

The code used to simulate thermal convection in rotating spherical shells is a modified version from the original code implemented by Glatzmaier (1984), which takes advantage of the property that a solenoidal field, the mass flux, can be represented by poloidal (W) and toroidal (Z) scalar potentials:

$$\hat{\rho}\boldsymbol{u} = \boldsymbol{\nabla} \times \boldsymbol{\nabla} \times (W\hat{r}) + \boldsymbol{\nabla} \times (Z\hat{r}) = (\hat{\rho}\boldsymbol{u})_{pol} + (\hat{\rho}\boldsymbol{u})_{tor}. \tag{1.47}$$

This decomposition automatically satisfies the conservation of mass (1.36) and reduces three dependent variables, the three components of the flow, to two, W and Z. The poloidal and toroidal parts of the mass flux contain mixed horizontal flow components, but the radial component of the flow enters only in the poloidal part. From (1.47), the components of the mass flux take the form

$$\hat{\rho}u_r = -\frac{1}{r^2}\mathcal{L}^2 W \tag{1.48}$$

$$\hat{\rho}u_\theta = \frac{1}{r}\frac{\partial}{\partial r}\Big(\frac{\partial W}{\partial \theta}\Big) + \frac{1}{r\sin\theta}\frac{\partial Z}{\partial \varphi} \tag{1.49}$$

$$\hat{\rho}u_\varphi = \frac{1}{r}\frac{\partial}{\partial r}\Big(\frac{1}{\sin\theta}\frac{\partial W}{\partial \varphi}\Big) - \frac{1}{r}\frac{\partial Z}{\partial \theta} \tag{1.50}$$

where $\mathcal{L}^2$ is an operator defined by

$$\mathcal{L}^2 = \frac{1}{\sin\theta}\frac{\partial}{\partial\theta}\Big(\sin\theta\frac{\partial}{\partial\theta}\Big) + \frac{1}{\sin^2\theta}\frac{\partial^2}{\partial\varphi^2}. \tag{1.51}$$

The poloidal and toroidal potentials together with the temperature field T and the pressure perturbation field P are expanded in spherical harmonics functions $Y_\ell^m(\theta,\varphi)$ in angular coordinates. Introducing this expansion in (1.48)-(1.50) the three components of the mass flux are given in spectral space by

$$\hat{\rho}u_r = \frac{1}{r^2}\sum_{\ell,m}\ell(\ell+1)W_\ell^m Y_\ell^m \tag{1.52}$$

$$\hat{\rho}u_\theta = \frac{1}{r\sin\theta}\sum_{\ell,m}\left(\frac{\partial W_\ell^m}{\partial r}\sin\theta\frac{\partial Y_\ell^m}{\partial\theta} + Z_\ell^m\frac{\partial Y_\ell^m}{\partial\varphi}\right) \tag{1.53}$$

$$\hat{\rho}u_\varphi = \frac{1}{r\sin\theta}\sum_{\ell,m}\left(\frac{\partial W_\ell^m}{\partial r}\frac{\partial Y_\ell^m}{\partial\varphi} - Z_\ell^m\sin\theta\frac{\partial Y_\ell^m}{\partial\theta}\right) \tag{1.54}$$

where it is used the property of the spherical harmonics that

$$\mathcal{L}^2 Y_\ell^m(\theta,\varphi) = -\ell(\ell+1)Y_\ell^m(\theta,\varphi). \tag{1.55}$$

The complex coefficients W_ℓ^m and Z_ℓ^m are further expanded in Chebyshev polynomials $T_n(r)$ up to a degree n_c in the radial direction and the Chebyshev coefficients are calculated separately for each harmonic mode (ℓ,m) by a collocation method on n_r grid points given by

$$r_k = \frac{r_o + r_i}{2} + \frac{1}{2}\cos\Big(\frac{k\pi}{n_r}\Big) \quad \text{with } k = 0, 1, \ldots, n_r.$$

The system of equations solved by the code are the equation for the temperature, the radial component of (1.37) and the horizontal divergence of (1.37) which give two coupled equations for W and P, and the radial component of the curl of (1.37) which gives the equation for Z using that

$$\Big(\boldsymbol{\nabla}\times(\hat{\rho}\boldsymbol{u})\Big)_r = -\frac{1}{r^2}\mathcal{L}^2 Z = \frac{1}{r^2}\sum_{\ell,m}\ell(\ell+1)Z_\ell^m Y_\ell^m. \tag{1.56}$$

The advection and the Coriolis terms are treated explicitly in the physical space and the result is projected on the different harmonic modes (ℓ,m). All the remaining linear terms decouple in (ℓ,m) and are treated implicitly. The solution is advanced in time in spectral space with a combination of an explicit Adams-Bashforth scheme with an implicit Crank-Nicholson treatment of the diffusion terms, both schemes second order accurate. The time step is limited by the Courant criterion which in other words means, that the time step has to be less than the time the fluid needs to flow from one grid point to another. A detailed description of the numerical technique is given in Glatzmaier (1984) and Tilgner (1999).

1.5.2 Code implementation

The modification of the Boussinesq code to compressible anelastic is straightforward since the scalar potentials describe mass flux field instead of velocity. However, the anelastic viscous force is more complex and requires to be expressed in spectral representation to be included in the code. The derivations in spectral space of the radial component of (1.39) and (1.42) as well as their respective horizontal divergence and radial curl are cumbersome and therefore their final expressions are given in §C.1 of Appendix C.

The free-slip boundary condition in spectral space is modified in the anelastic case. Since the scalar potentials describe mass flux and the free-slip boundary condition given in (1.44) applies to the velocity field, the condition in spectral space writes slightly different from the Boussinesq case:

$$\frac{\partial}{\partial r}\Big(\frac{1}{r^2\hat{\rho}}\frac{\partial W}{\partial r}\Big)=\frac{\partial}{\partial r}\Big(\frac{1}{r^2\hat{\rho}}Z\Big)=0. \tag{1.57}$$

When there is no density stratification, i.e. $\hat{\rho}=1$, (1.57) recovers the expression of the boundary condition for the Boussinesq case.

The non-penetration as well as non-slip boundary conditions are not affected in the anelastic case and remain the same as in the Boussinesq case in spectral space.

1.5.3 Testing the anelastic code

Before performing any simulation with the modified code, we have to test that the modifications were correctly implemented. The idea behind is simple: we take the output solution given by the code and check if it satisfies the equations (1.37) and (1.38) at a certain time and grid point. To accomplish this, finite differences methods were used to approximate the radial gradient of fluid properties as well as the temporal and spatial derivatives of P, T, and the three components of velocity in the equations (1.37) and (1.38).

Approximation of derivatives by finite differences is a common and well-known practice specially if the grid is evenly spaced as it is the case for θ, φ and t. However, the code solves the equations in an unequally spaced radial grid which has to be taken into account when approximating derivatives.

For evenly and unevenly spaced grid we approximate first and second-order derivatives with three grid points. Except for the second-order radial derivatives which are first order accurate, all the other derivatives have an accuracy of second order. Mixed derivatives are approximated with three grid points in each direction resulting in a mesh of nine grid points.

Finite differences representations have the clear disadvantage compared to spectral methods of less accuracy for the same resolution. Two to four times more grid points are required to obtain numerical accuracy comparable to spectral collocation methods (Orszag, 1971; Christensen et al., 2001). We have to keep this in mind since the grid to discretise the derivatives is the same as the grid used by the code to solve the equations.

The code was tested for the cases A, B, C and D setting the aspect ratio r_i/r_o in 0.35 which is representative of a thick shell. The Rayleigh number was always chosen supercritical. The Prandtl and Ekman numbers were taken respectively as $Pr_o = 1$ and $E_o = 10^{-2}$ in all the four cases. The value chosen for the Ekman number is relatively high compared to the values normally used in the simulations because for smaller E higher resolution is needed but finite differences require much higher resolution than spectral methods for the same accuracy. Therefore, to test the code with finite differences, the resolution used to obtain a solution of the equations with the code was much higher than the one actually needed to resolve adequately the calculations.

The choice of the grid point to test if the solution satisfies the equations is arbitrary as well as the choice of the time. However, the radial grid point was chosen at mid-depths of the shell since the radial grid is evenly spaced in that region resulting in an increase of the accuracy of the radial second order derivative.

The number of grid points and times tested were enough to be sure that for every equation, the left hand side (LHS) having only time derivatives, and the right hand side (RHS) having the rest of the terms, were equal within the accepted error.

The code for the incompressible case was verified against other codes in a benchmark test (Christensen et al., 2001). For this reason, our finite differences testing method for the anelastic code was first probed for the Boussinesq case. Taking 49 radial grid points, 64 grid points in θ and 128 points in φ the relative error between LHS and RHS was around 30% for the components of the Navier-Stokes equation and around 7% for the energy equation. With a finer grid consistent of 81 radial grid points, 200 grid points in θ and 400 grid points in φ the relative error between LHS and RHS decreased to 2% for the components of the Navier-Stokes equation and to less than 1% for the energy equation. The anelastic code was considered successfully tested for every case when the previous relative errors for the finer grid were obtained.

2 Onset of convection

2.1 Fundamentals on linear stability theory

2.1.1 Convective instability

Let us consider a fluid plane layer as an illustrative example. The gravity force is directed downwards and the temperature decreases with height. Let us imagine that a hot fluid parcel from below moves upwards a distance dz. If the fluid is incompressible, the parcel is always lighter than the colder environment[1] and will rise indefinitely. This necessary criterion of convective instability can be summarised as:

$$\frac{dT}{dz} < 0. \tag{2.1}$$

If the fluid is compressible the previous criterion is not sufficient. The fluid parcel in the new position will expand adiabatically since the hydrostatic pressure is lower and as a result it will cool down. The parcel will continue moving upwards if its local temperature is higher than the local adiabatic temperature in every new position. This criterion can be written as

$$\frac{dT}{dz} < \frac{dT_{ad}}{dz} = -\frac{g\alpha T}{C_p} \tag{2.2}$$

where $\frac{dT_{ad}}{dz}$ is the adiabatic temperature gradient.

The instability criterion (2.2) converts to (2.1) when there is no adiabatic temperature gradient. This is the case when the fluid is incompressible or when the fluid is compressible but the Grüneisen parameter is zero since in both cases the adiabatic heating effect is neglected.

The previous instability criteria are necessary conditions. However, when viscosity and thermal conduction are present, the convective instability will take place if the buoyancy force as the driving force of convection can overcome the frictional action of viscosity and the homogenising effect on temperature resulting from thermal conduction, factors that inhibit convection. In terms of the Rayleigh number, convection will take place when $Ra > Ra_c$: the higher the value of Ra_c, the higher the driving force has to be to destabilise the system to have convective motions.

---

[1] Assuming that the thermal expansivity coefficient is positive. If it is negative the convective instability criterion is reversed.

2.1.2 Analytical description

The stability of a system is studied through its reaction to small disturbances: if they gradually die down the system recovers the initial state and in this sense it is stable with respect to these particular disturbances. If they grow in amplitude in a way that the system progressively departs from the initial state, the system becomes unstable (Chandrasekhar, 1961). Disturbances of the variables are infinitesimal increments and therefore, the non-linear terms, which are terms of higher order in the disturbances, are neglected in the formalism resulting for our problem the equations given in §1.4.3.

Assuming the time dependence of the unknown variables, W, Z, P and Θ, as $e^{\sigma t}$, the system of equations is reduced to a characteristic value problem for σ. Expanding the unknowns in spherical harmonics functions, one finds that every term in the linearised equations (1.45) and (1.46) is decoupled in every (ℓ, m) mode, aside from the Coriolis force which couples the degree ℓ with its neighbouring degrees $\ell \pm 1$. Thus, each mode m evolves in time independently from the others and the equations can be solved for each m separately.

In general the characteristic value σ is complex. The first mode m_c that becomes unstable when the control parameter Ra reaches the "critical" value Ra_c will be the one verifying that it is

- stable if $Ra < Ra_c$: the disturbances for the mode m_c decrease in amplitude, condition satisfied by $Re(\sigma_{m_c}) < 0$,
- marginal stable if $Ra = Ra_c$: the disturbances for the mode m_c don't increase nor decrease, condition satisfied by $Re(\sigma_{m_c}) = 0$, and all the other modes are stable, i.e. $Re(\sigma_m) < 0 \ \forall m \neq m_c$, and
- unstable if $Ra > Ra_c$: the disturbances increase in amplitude, condition satisfied by $Re(\sigma_{m_c}) > 0$.

The critical mode can evolve in time during the transition from stability to instability in two different ways. It can be

- stationary if $Im(\sigma_{m_c}) = \omega_c = 0$, or
- oscillatory if $Im(\sigma_{m_c}) = \omega_c \neq 0$,

where ω_c is the oscillation frequency. Thus, Ra_c, ω_c and m_c characterise, respectively, the occurrence of the marginal state, its temporal dependence and azimuthal symmetry.

2.2 Onset of convection in rapidly rotating incompressible spherical systems

2.2.1 Taylor-Proudman theorem

Let us consider the Navier-Stokes equation (1.37) in the Boussinesq limit of constant density (i.e. $\hat{\rho} = 1$). Under the assumptions that the motions are infinitesimal and steady, and the fluid is inviscid and highly rotating, the equation reduces to the geostrophic balance

$$2\hat{\boldsymbol{z}} \times \boldsymbol{u} = -\boldsymbol{\nabla} p. \tag{2.3}$$

By taking the curl of (2.3) and using the incompressibility condition $\boldsymbol{\nabla} \cdot \boldsymbol{u} = 0$, it follows that

$$\frac{\partial \boldsymbol{u}}{\partial z} = 0. \tag{2.4}$$

This result is known as the Taylor-Proudman theorem and it expresses that under the conditions mentioned above the flow of a rotating fluid is z-independent. If the system has solid boundaries perpendicular to the rotation axis, (2.4) implies that $u_z = 0$ everywhere, i.e. the flow is two-dimensional.

In terms of dimensionless numbers, the limit of fast rotation and low viscosity is expressed as $E \ll 1$, and the limit of infinitesimal motions as $Ro = \frac{U}{d\Omega} \ll 1$, where Ro is known as Rossby number and U is a characteristic convective velocity. The atmospheres of the giant planets are believed to obey these conditions. Taking the case of Jupiter, the estimate of the order of magnitude of E and Ro is 10^{-15} and 10^{-4} respectively, values obtained from mixing length theory (Guillot et al., 2004). Therefore, the Taylor-Proudman theorem requires z-independent fluid motions in the atmospheres of the giant planets if the fluid is incompressible.

Looking closer at the problem of thermal convection in a sphere or spherical shell in fast rotation, the non-penetration boundary condition $u_r = 0$ imposes z-dependence to the components u_r and u_θ of the motion. Thus, convection in a sphere or spherical shell is never geostrophic and additional terms in the geostrophic balance must enter to set up convection. The only motion that can be truly geostrophic is azimuthal.

2.2.2 Asymptotic studies and style of convection

The physically relevant limit for convection in giant planets' atmospheres is $E \to 0$. Asymptotic theoretical studies are focused mainly on the behaviour of Ra_c, m_c and ω_c while experimental and numerical studies try to reach as low values of E as possible to confirm or discard these theories.

The asymptotic theory for convection in a rapidly rotating sphere was obtained by Roberts (1968) and modified later by Busse (1970), who predicted that convection

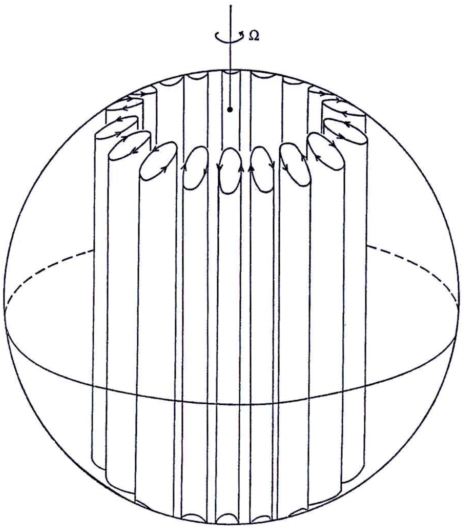

Fig. 2.1: Onset of convection in a fast rotating sphere according to Busse (1970).

develops in the form of nearly two-dimensional rolls confined to a cylindrical shell coaxial to the rotation axis, as it is shown in figure 2.1.

Numerical and theoretical studies afterwards (Zhang and Busse, 1987; Zhang, 1992b; Zhang, 1994) showed that the preferred mode of convection can differ from the columnar one expected from the Roberts-Busse's theory. The preferred style of convection in rapidly rotating spherical systems is determined by the Prandtl number:

a) Large Pr ($Pr \gg 1$): Columnar convection

b) Moderate Pr ($Pr \sim 1$): Spiralling convection

c) Small Pr ($Pr \ll 1$): Wall-attached convection

Columnar convection

The asymptotic laws for onset of convection in a rapidly rotating sphere from the Roberts-Busse's asymptotic theory are

$$Ra_c \sim \left(\frac{Pr}{1+Pr}\right)^{4/3} E^{-4/3}, \; m_c \sim \left(\frac{Pr}{1+Pr}\right)^{1/3} E^{-1/3}, \; \omega_c \sim \left(\frac{1}{(1+Pr)^2}\right)^{1/3} E^{-2/3} \tag{2.5}$$

as $E \to 0$. They express that the critical values Ra_c, m_c and ω_c increase with increasing rotation rate, and describe as well their dependence with Pr.

The onset of convection is such that the most unstable mode is usually non-axisymmetric ($m_c \neq 0$), time-dependent ($\omega_c \neq 0$), and exhibits equatorial symmetry

(Busse, 1970) as figure 2.1 shows.

The time dependence of the columnar convection pattern appears as an azimuthal drift in the eastwards (or prograde) direction. Describing the linear solution for onset of convection as

$$\boldsymbol{u} = \boldsymbol{u}(r, \theta) e^{i m_c \varphi + i \omega_c t}, \tag{2.6}$$

eastwards drift corresponds to $\omega_c < 0$. The two-dimensionality condition imposed by the Taylor-Proudman theorem cannot be achieved when the boundaries are not strictly perpendicular to the rotation axis. In addition, the non-penetration boundary condition imposes z-dependence to u_r and u_θ. Thus, some time-dependence appears in the convection pattern because the motion can no longer satisfy the geostrophic balance due to the inclined outer boundary.

The preferred eastwards direction of the drift is related to the inclination of the confining boundary (Busse, 1994; Busse, 2002). When the height[2] of the fluid decreases with the distance s from the rotation axis, as it is the case for a sphere or spherical shell, the drift is prograde. When the height of the fluid increases with s, as might be the case for example, of an annulus with shorter inner cylinder than the outer one, the drift is in the opposite sense.

The asymptotic laws have been confirmed numerically (Zhang, 1991; Zhang, 1992b) and experimentally (Busse and Carrigan, 1976; Carrigan and Busse, 1983). However, the influence of the outer boundary was not fully taken into account in the original sketch of Busse as it was revealed by these studies: the convex curvature of the spherical outer boundary induces a prograde tilt in the columns. A retrograde tilt can be induced in other kind of systems that allow the opposite concavity, like an annulus with concave top and bottom boundaries (Busse, 2002).

Spiralling convection

At high Prandtl number the effect of viscosity is stronger than thermal diffusivity and the columnar pattern of convection is well confined to a thin cylindrical layer, as predicted by the asymptotic laws. However, when the Prandtl number decreases, the relative effect of the thermal diffusivity increases and convection columns can extend to the equatorial region (Zhang, 1992b).

According to Zhang (1992b) a columnar convection roll is forced to spiral progradely since the phase speed of the Rossby-type wave that arises from the change of height of the fluid column is approximately proportional to the slope of the spherical boundary. The change from columnar roll to spiralling columnar convection occurs continuously as the Prandtl number decreases since they constitute the same branch in phase space (Yano, 1992).

---

[2] Height in this context refers to the column of fluid parallel to the rotation axis.

From the previous discussion in spiralling-columnar convection, it can be concluded that the curved outer boundary in spherical systems plays a fundamental role in controlling the structure of the convection pattern and its time evolution at onset. As well, it is responsible for the existence of prograde drift, eastwards tilt, and columnar or spiralling structure depending on the value of the Prandtl number, as different analytical, numerical and experimental studies revealed.

Thermal inertial waves

Further decrease of the Prandtl number leads to marginal convection modes with different characteristics compared to the spiralling-columnar convection. The first evidence of this is that the convective motions are trapped in the equatorial outer region (called therefore wall-attached convection). As a consequence, the inner spherical boundary does not have much influence on the convection (Zhang, 1993). There are however, other fundamental differences. In the case of the columnar convection, the viscous force enters in the geostrophic balance to break the constraint imposed by rotation. In the equatorial trapped modes the convection oscillates fast and the constraint imposed by rotation is broken by $\frac{\partial \boldsymbol{u}}{\partial t}$ instead. Thus, the viscous force does not enter in the leading-order problem and its role is purely dissipative (Zhang, 1994; Zhang, 1995).

These fast convection modes are inertial oscillation modes of the Poincaré equation. They are symmetric with respect to the equator and are usually known as thermal inertial waves. There are two different classes of inertial oscillations: eastwards propagating ($\omega < 0$) and westwards propagating ($\omega > 0$). Whether the eastwards or the westwards propagating modes are most unstable depends on the Prandtl number. The convection modes eastwards propagating are most unstable however, further decrease of the Prandtl number leads to a transition from eastwards to westwards propagating modes (Zhang, 1994).

The value of the Prandtl number at which the transition from spiralling-columnar convection to equatorially trapped convection takes place depends on the Ekman number (Zhang, 1994).

The asymptotic laws at low Prandtl number for stress-free boundary conditions are

$$Ra_c \sim E^0,\ m_c \sim E^0,\ \omega_c \sim E^0, \quad \text{as} \ \ E \to 0 \tag{2.7}$$

according to Zhang (1995) . Thus, the scale of the convection is large (E^0) compared to the width of the columns that scales as $E^{1/3}$ according to (2.5). A complete analysis of thermal inertial waves and asymptotic laws at low Pr can be found in Zhang (1994; 1995).

2.3 Numerical marginal stability simulations for compressible fluids

The numerical simulations were performed for a thick spherical shell of aspect ratio $\eta = r_i/r_o = 0.35$. The shell thickness is normalised in the numerical model, $d = r_o - r_i = 1$. As a result the inner and outer radius in non-dimensional form are $r_i = \frac{\eta}{1-\eta}$ and $r_o = \frac{1}{1-\eta}$ with values 0.53846 and 1.53846 respectively for the chosen aspect ratio.

Actual interior models place the molecular/metallic hydrogen transition at 80% of the planetary radius in Jupiter, and at 50% in Saturn (Guillot, 1999). Our model describes a thicker atmosphere with the molecular/metallic hydrogen transition at 35% of the planetary radius r_o. This choice, though not very adequate at first glance, has the advantage of being numerically less expensive.

Our model has a sharp separation between the inner and the outer shell. However, how and where this transition takes place in the giant planets is still unclear. Theoretical models of high-pressure, low-temperature liquid hydrogen equation of state predicts a discontinuous (plasma) phase transition (Saumon et al., 1995), while shock compression experiments on liquid deuterium favour a continuous transition since the resistivity of liquid hydrogen decreases up to about 1.4Mbar pressure (Nellis et al., 1999).

The numerical results of marginal stability were obtained by a different approach than solving the characteristic value problem. Imposing a perturbation to the linearised system by choosing a value of the Rayleigh number, the characteristic values of the solution are studied after a sufficiently long integration time. With $e^{\sigma t}$ as time dependence, the linearised system is time stepped until a steady solution is reached. The stability of every mode m can be examined checking whether $Re(\sigma_m)$ is positive, negative or nearly zero. When there was only one unstable mode, we considered that the marginal state was reached for the value of the Rayleigh number at which $Re(\sigma_{m_c})$ differed from 0^+ in less than 5%.

The characteristic value σ_m is numerically approximated making use of the poloidal potential $W_\ell^m(r,t)$ at a degree $\ell = m$ and radial position fixed at mid-depth r_c as

$$\sigma_m \simeq \frac{1}{W^m(t)} \, \frac{W^m(t) - W^m(t-\delta t)}{\delta t} \tag{2.8}$$

where δt is the time step, $W^m(t) = W_m^m(r_c, t)$ depends as $e^{\sigma_m t}$, and $(W^m, \sigma_m) \in \mathcal{C}$. Additional details about this technique are given in Dormy (1997).

Glatzmaier and Gilman (1981a) studied numerically linear convection onset for a compressible fluid in a spherical shell assuming the standard anelastic approximation. Their results show for all the Taylor[3] numbers studied at different density stratifications, that the most unstable equatorially antisymmetric mode m_a is always excited after the most unstable symmetric one m_s. In other words, $(Ra_c)_a > (Ra_c)_s$. Therefore, we computed only characteristic values for the equatorially symmetric modes.

For each mode m, the associated degrees ℓ can belong to two independent families, $\ell + m$ even or $\ell + m$ odd, which correspond to the two possible symmetries with respect to the equator. The equatorially symmetric family of solutions exists for $W_\ell^m(r,t)$ when $\ell + m$ is even (Glatzmaier, 1984)[4]. Since for a certain mode m, all the degrees ℓ of the same family evolve in time in the same way, the characteristic values were calculated for a fixed ℓ. The choice of $\ell = m$ in $W_\ell^m(r,t)$ guarantees that $\ell + m = 2m$ is even for every m, which assures equatorially symmetric solution.

2.3.1 Results for $\hat{\nu}$ constant, cases A and B

The onset of convection is studied first for the cases where the kinematic viscosity is constant, i.e. $\hat{\nu} = 1$, since the Ekman number does not change throughout the shell (see table 1.2). From (1.40), constant kinematic viscosity leads to a shear viscosity $\hat{\mu}$ with the same radial dependence as the density $\hat{\rho}$. Examples of exponential background density profiles for different values of Co are shown in figure 2.2. The maximum density ratios $\hat{\rho}_i/\hat{\rho}_o$ corresponding to the values of Co used in the simulations are shown in table 2.1.

In the case A, the thermal diffusivity is constant, i.e. $\hat{\kappa} = 1$. Therefore, from (1.41) the thermal conductivity $\hat{k}$ has the same radial dependence as the density $\hat{\rho}$. Since Ra, E and Pr are defined in terms of viscous and thermal diffusivities, this case allows a more straight forward interpretation because all the control parameters of the problem remain constant throughout the simulated shell.

In the case B, the thermal conductivity is constant, i.e. $\hat{k} = 1$, which results from (1.41) in $\hat{\kappa}$ with radial dependence as $1/\hat{\rho}$. The variation with radius of the local Ra and the local Pr is revealed when they are reformulated in terms of $\hat{k}$. Thus, Ra and Pr increase inwards with the same radial dependence as $\hat{\rho}$.

Tables 2.2, 2.3 and 2.4 list the critical Rayleigh number Ra_c, critical wave number m_c, critical oscillation frequency ω_c and drift velocity $c = \omega_c/m_c$ with increasing stratification at $E = 1 \times 10^{-3}$ and $E = 3 \times 10^{-4}$ for the cases A and B. For the case B, the reference value of $\hat{\kappa}$ defining the dimensionless numbers was fixed at the inner and at the outer boundary, models accordingly labelled as BI and BO.

---

[3] The Taylor number is related to the Ekman number as $T = \left(\frac{2}{E}\right)^2$.

[4] If the toroidal potential $Z_\ell^m(r,t)$ is used to study linear onset, the family $\ell + m$ odd gives the symmetric solution with respect to the equator.

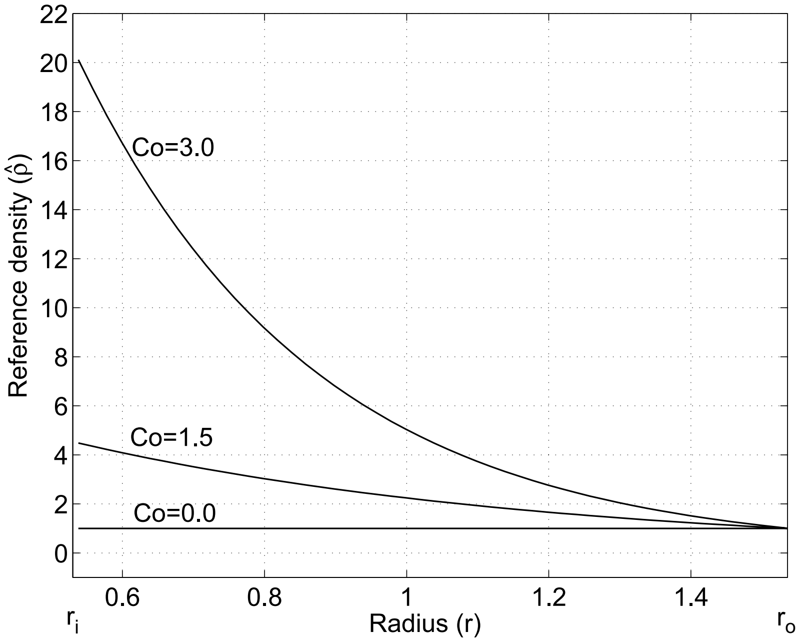

Fig. 2.2: Background density profile for different stratification degrees.

Co	0.0	0.5	1.0	1.5	2.0	2.5	3.0	3.5	4.0	4.5	5.0
$\hat{\rho}_i/\hat{\rho}_o$	1.00	1.65	2.72	4.48	7.39	12.2	20.1	33.1	54.6	90.0	148

Table 2.1: Values of shell density ratios $\hat{\rho}_i/\hat{\rho}_o$ associated to Co.

	Case A: $\hat{\nu} = 1$, $\hat{\kappa} = 1$				Case B: $\hat{\nu} = 1$, $\hat{k}$=1			
	$Pr = 1$				Case BO: $Pr_o = 1$			
Co	Ra_c	m_c	ω_c	c	$(Ra_c)_o$	m_c	ω_c	c
0.0	2.837×10^4	4	-33.94	-8.49	2.837×10^4	4	-33.94	-8.49
0.5	4.050×10^4	5	-51.83	-10.37	3.100×10^4	5	-36.63	-7.33
1.0	5.500×10^4	6	-69.80	-11.63	3.003×10^4	6	-31.49	-5.25
1.5	7.263×10^4	7	-89.23	-12.75	2.570×10^4	7	-23.64	-3.38
2.0	9.420×10^4	8	-112.42	-14.05	2.040×10^4	8	-17.56	-2.20
2.5	1.173×10^5	10	-141.68	-14.17	1.574×10^4	8	-13.77	-1.72
3.0	1.281×10^5	15	-176.34	-11.76	1.182×10^4	9	-10.37	-1.15
3.5	1.316×10^5	16	-201.37	-12.59	8.700×10^3	9	-7.63	-0.85
4.0	1.348×10^5	17	-220.45	-12.97	6.300×10^3	9	-5.44	-0.60
4.5	1.382×10^5	18	-235.63	-13.09	4.500×10^3	9	-3.79	-0.42
5.0	1.420×10^5	19	-248.35	-13.07	3.190×10^3	9	-2.60	-0.29

Table 2.2: Critical values for onset of convection for $\hat{\nu} = 1$ at $E = 1 \times 10^{-3}$.

	Case A: $\hat{\nu} = 1$, $\hat{\kappa} = 1$				Case B: $\hat{\nu} = 1$, $\hat{k}$=1				
	$Pr = 1$				Case BO: $Pr_o = 1$				
Co	Ra_c	m_c	ω_c	c	$(Ra_c)_o$	$(Ra_c)_i$	m_c	ω_c	c
0.0	9.920×10^4	6	-79.03	-13.17	9.920×10^4	9.920×10^4	6	-79.03	-13.17
0.5	1.560×10^5	7	-119.48	-17.07	1.161×10^5	1.916×10^5	7	-84.11	-12.02
1.0	2.268×10^5	8	-161.26	-20.16	1.167×10^5	3.174×10^5	8	-73.71	-9.21
1.5	3.163×10^5	10	-201.33	-20.13	1.007×10^5	4.511×10^5	10	-52.87	-5.29
2.0	4.292×10^5	11	-249.79	-22.71	7.980×10^4	5.897×10^5	12	-37.16	-3.10
2.5	5.653×10^5	19	-339.02	-17.84	6.110×10^4	7.454×10^5	12	-29.34	-2.45
3.0	6.103×10^5	23	-400.19	-17.40	4.580×10^4	9.206×10^5	13	-21.87	-1.68
3.5	6.240×10^5	27	-443.71	-16.43	3.360×10^4	1.112×10^6	13	-15.95	-1.23
4.0	6.266×10^5	28	-502.32	-17.94	2.420×10^4	1.321×10^6	13	-11.24	-0.86
4.5	6.286×10^5	30	-535.89	-17.86	1.720×10^4	1.548×10^6	14	-8.00	-0.57
5.0	6.319×10^5	31	-578.40	-19.66	1.205×10^4	1.783×10^6	14	-5.47	-0.39

Table 2.3: Critical values for onset of convection for $\hat{\nu} = 1$ at $E = 3 \times 10^{-4}$ for the cases A and BO.

	Case B: $\hat{\nu} = 1$, $\hat{k}$=1				
	Case BI: $Pr_i = 1$				
Co	$(Ra_c)_o$	$(Ra_c)_i$	m_c	ω_c	c
0.0	9.920×10^4	9.920×10^4	6	-79.03	-13.17
0.5	9.732×10^4	1.606×10^5	7	-125.93	-17.99
1.0	8.480×10^4	2.306×10^5	8	-177.12	-22.14
1.5	6.814×10^4	3.053×10^5	8	-239.19	-29.90
2.0	5.204×10^4	3.846×10^5	9	-307.09	-34.12
2.5	4.002×10^4	4.882×10^5	10	-360.52	-36.05
3.0	2.931×10^4	5.891×10^5	10	-429.08	-42.91
3.5	2.102×10^4	6.957×10^5	10	-501.75	-50.18
4.0	1.554×10^4	8.485×10^5	11	-530.59	-48.24
4.5	1.033×10^4	9.297×10^5	11	-635.15	-57.74
5.0	7.183×10^3	1.063×10^6	11	-697.53	-63.41

Table 2.4: Critical values for onset of convection for $\hat{\nu} = 1$ at $E = 3 \times 10^{-4}$ for the case BI.

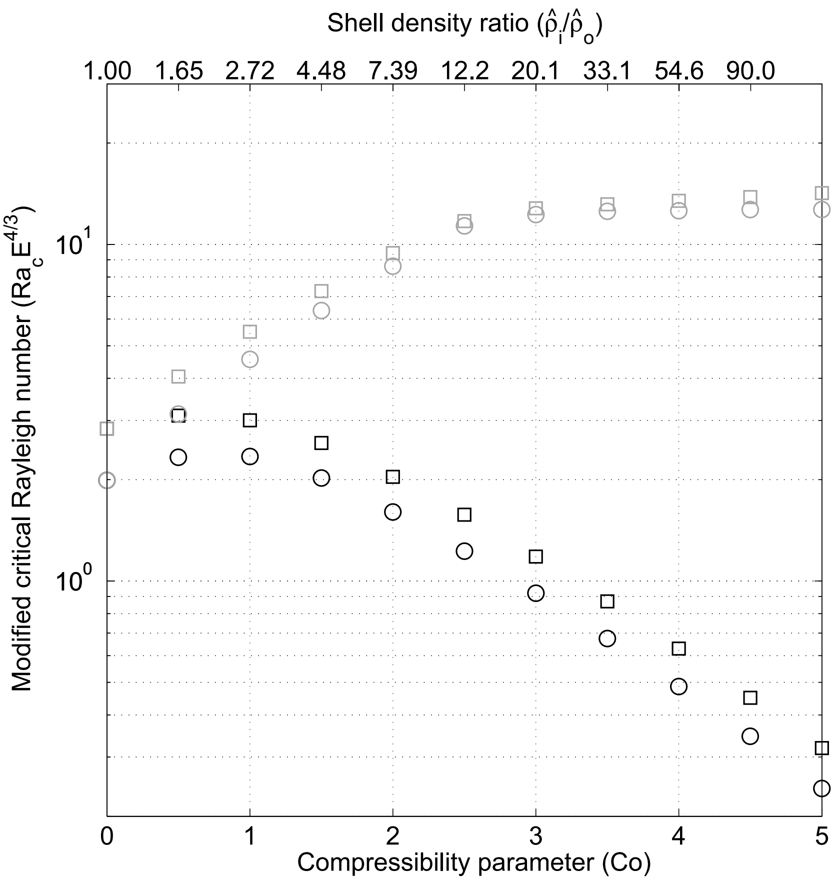

Fig. 2.3: Modified critical Rayleigh number $Ra_c E^{4/3}$ plotted as a function of Co. Squares: $E = 1 \times 10^{-3}$. Circles: $E = 3 \times 10^{-4}$. Gray: $\hat{\kappa} = 1$ (case A). Black: $\hat{k} = 1$ (case BO).

Ra_c, m_c and ω_c form for each value of E separate groups with similar variation with Co as shown for Ra_c in figure 2.6. This indicates that the dependence on E and Co is separable and then, Ra_c, m_c and ω_c may be rescaled as

$$Ra_c E^{4/3} = f(Co), \quad m_c E^{1/3} = g(Co), \quad \omega_c E^{2/3} = h(Co), \quad \text{as } \; E \to 0, \tag{2.9}$$

where f, g and h are functions that include as well the dependence with the Prandtl number. Figures 2.3, 2.4 and 2.5 display the respective rescaled curves, which show in most of the cases a striking collapse from two curves into one. It is not clear why for the case BO, $Ra_c E^{4/3}$ displays two curves with the same offset at each value of Co. Since $Pr > 1$ at every point of the shell for $Co > 0$, the asymptotic power 4/3 should be better satisfied than for the case A, where $Pr = 1$ (Zhang, 1991). Critical values at lower E are required to see whether this behaviour persists.

Figure 2.7 and 2.8 show equatorial cuts of z-vorticity and temperature at different Co. The increasing stratification confines the convection to increasingly narrower regions and the wave number increases accordingly. The most remarkable change

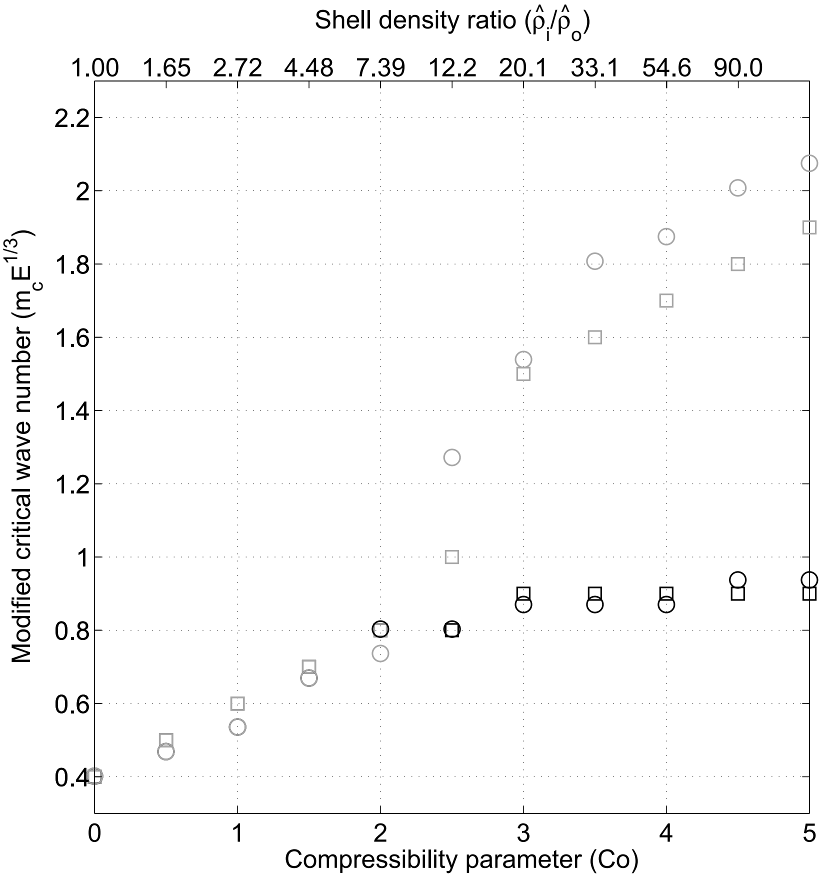

Fig. 2.4: Modified critical wave number $m_cE^{1/3}$ plotted as a function of Co. Squares: $E = 1 \times 10^{-3}$. Circles: $E = 3 \times 10^{-4}$. Gray: $\hat{\kappa} = 1$ (case A). Black: $\hat{k} = 1$ (case BO).

appears around $Co = 2.5$ for the case A. For smaller Co, convection remains attached to the inner boundary as it is also in the Boussinesq case. Beyond $Co = 2.5$, convection sets in close to the outer boundary. A sharp increase in the wave number marks this transition in figure 2.4. The separation of curves beyond $Co = 2.5$ somehow suggests that the power 1/3 may not be well suited when convection is localised closer to the outer boundary.

At smaller values of Co in the case A, density stratification has a stabilising effect on convection, indicated by the increase of Ra_c with Co. At larger Co, the steeper outer boundary slope stabilises the convection as well. How much is the contribution of the density stratification compared to the slope effect cannot be distinguished with this model. However, the nearly constant Ra_c suggests that the density stratification and the outer boundary inclination modify only slightly the convective instability.

The decrease of $(Ra_c)_o$ with Co in the case B is related to the variation of the radial profile of $\hat{\kappa}$ with different Co. As Co increases, the ratios $\hat{\kappa}_i/\hat{\kappa}_o$ decrease and

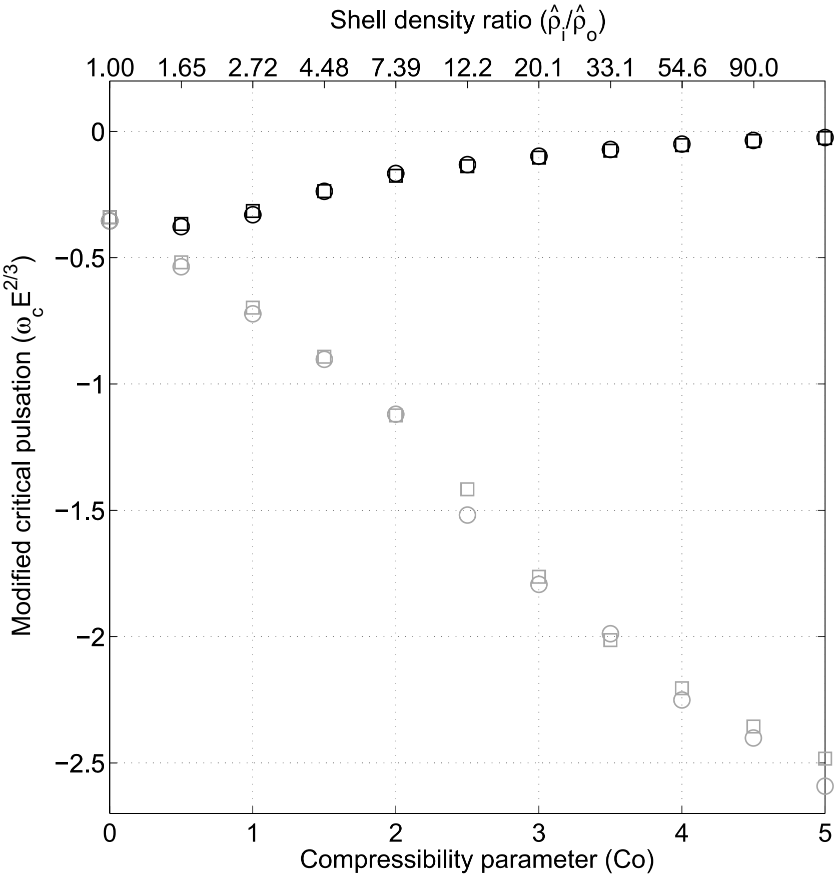

Fig. 2.5: Modified critical oscillation frequency $\omega_c E^{2/3}$ plotted as a function of Co. Squares: $E = 1 \times 10^{-3}$. Circles: $E = 3 \times 10^{-4}$. Gray: $\hat{\kappa} = 1$ (case A). Black: $\hat{k} = 1$ (case BO).

therefore, $(Ra_c)_o$ reflects the convective instability of a shell with smaller mean $\hat{\kappa}$ that results in the decrease of $(Ra_c)_o$ with Co. Thus, comparisons between $(Ra_c)_o$ for different values of Co don't give a clear picture whether density stratification stabilises the system or not.

When the Rayleigh number changes throughout the shell appears the problem of where to define it. Glatzmaier and Gilman (1981a) have in their anelastic linear models a local Rayleigh number that increases with radius. Although they have $\hat{\nu}$ and $\hat{\kappa}$ constant as in our case A, their gravity decreases slightly with radius and their superadiabatic temperature gradient increases very rapidly with radius for large stratifications. They found, evaluating the Rayleigh number in the centre of the shell, that Ra_c are essentially the same for a Boussinesq fluid and a compressible fluid with different levels of stratification. However, since the convective velocity is maximum in the region where the local Rayleigh number is large, i.e. at the outer boundary, evaluating Ra_c where the convective velocity peaks results in relatively more stable stratified fluid.

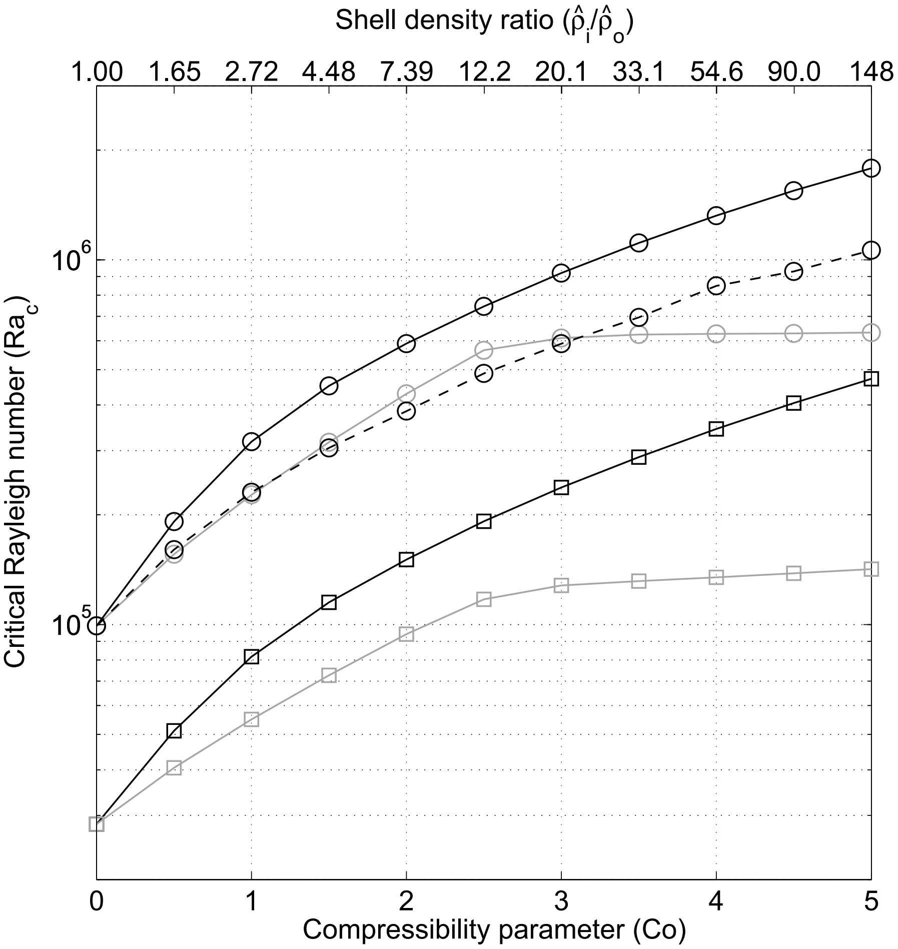

Fig. 2.6: Ra_c plotted as a function of Co for $\hat{\nu} = 1$. Squares: $E = 1 \times 10^{-3}$. Circles: $E = 3 \times 10^{-4}$. Gray: $\hat{\kappa} = 1$ (case A). Black: $\hat{k} = 1$ (case B); solid line: BO, broken line: BI.

In the case B, $(Ra_c)_o$ do not characterise the onset of convection since the flow is located adjacent to the inner boundary as figures 2.7 and 2.8 show. Evaluating the Rayleigh number at the inner boundary as $(Ra_c)_i = \hat{\rho}_i (Ra_c)_o$ leads to an increase of $(Ra_c)_i$ with Co as figure 2.6 shows. The radial change of the local Prandtl number adds further complexity in the comparisons. However, it can be concluded for the case BI that density stratification stabilises convection since for every Co the local Prandtl number remains unchanged where the flow peaks.

Drew, Jones and Zhang (1995) studied onset of convection for anelastic models with $\hat{\nu}$ and $\hat{k}$ constant. They, on the contrary to Glatzmaier and Gilman (1981a)'s study and this study, agreed to define the dimensionless numbers at mid-depth. They observed an increase of Ra_c with compressibility for the Prandtl numbers 1 and 10. On the other hand, for $Pr = 0.1$, at $Ta = 10^6$ ($\equiv E = 2 \times 10^{-3}$), they found a sharp decrease of Ra_c with growing compressibility becoming even negative. They

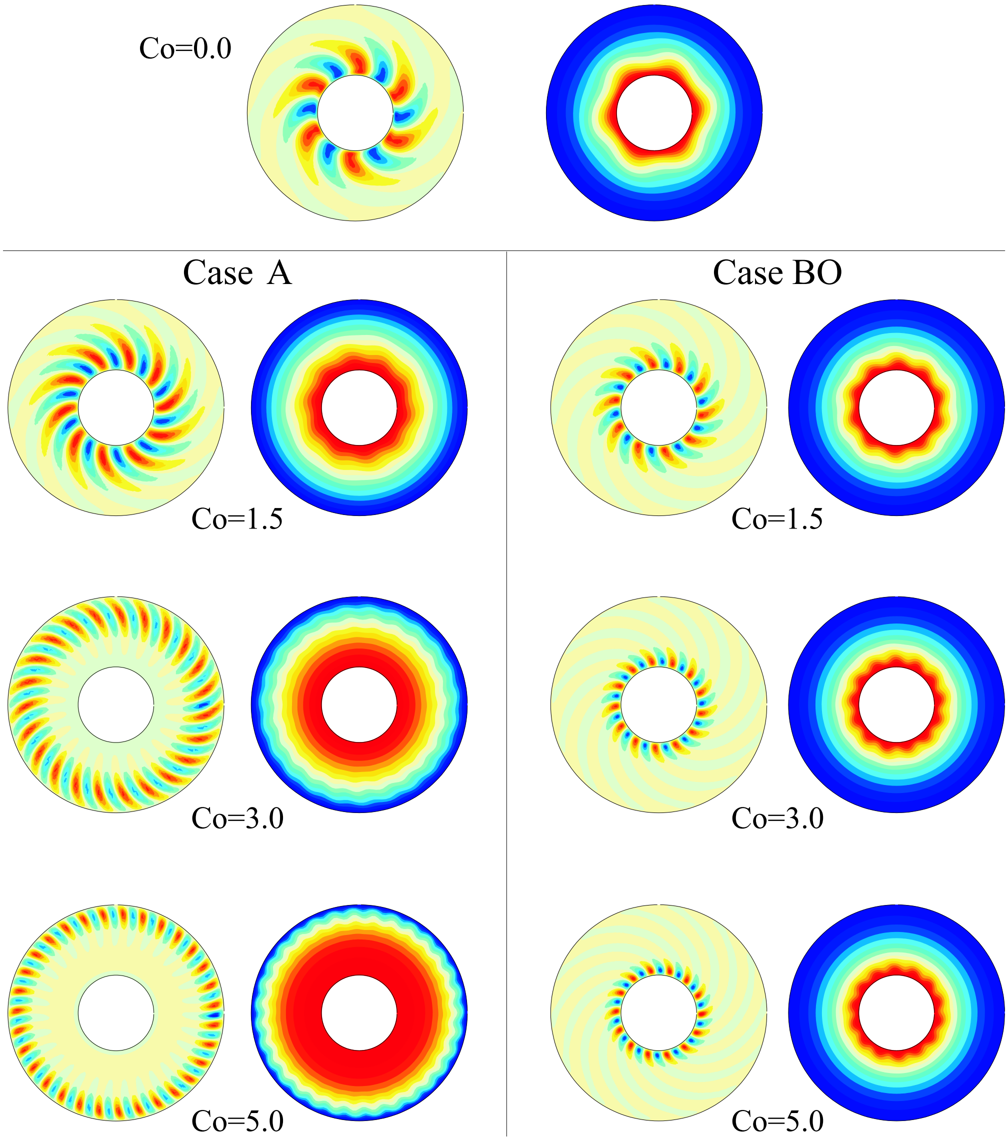

Fig. 2.7: Snapshots at the equatorial plane of z-vorticity (left) and temperature (right) at $E = 3 \times 10^{-4}$ and $Ra = 1.1 Ra_c$ for the cases A (left panel) and BO (right panel). The Boussinesq case for $Pr = 1$ is in the upper panel.

investigated this phenomenon through energy considerations and found out that negative Rayleigh numbers are not possible in the Boussinesq case since entropy and temperature are the same variable. According to this, in our anelastic models with vanishing Grüneisen parameter, we should not expect negative values of Ra_c at low values of Pr.

The prograde drift of the convection pattern in the incompressible case persists when the fluid is stratified. Glatzmaier and Gilman (1981a) found as well prograde drift in their anelastic models. In the Boussinesq case, the inclined outer boundary imposes a variation of the height of the fluid with the distance s to the rotation

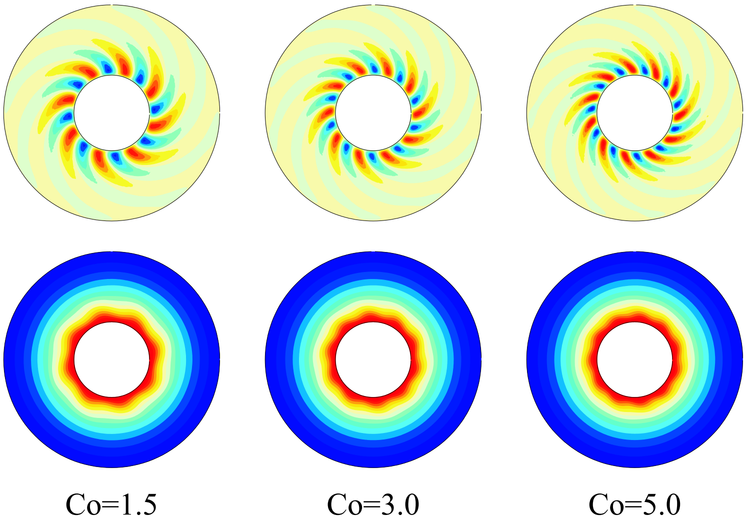

Fig. 2.8: Snapshots of equatorial z-vorticity (above) and temperature (below) at $E = 3 \times 10^{-4}$ and $Ra = 1.1Ra_c$ for the case BI.

axis which produces that convection columns shrink as they move away from the rotation axis and stretch as they move towards it, providing a mechanism to generate vorticity in the form of Rossby waves (Busse, 1994; Busse, 2002). For a stratified fluid, Glatzmaier and Gilman (1981b) showed with a simple analytical model of a rotating annulus concentric with the axis of rotation and with horizontal boundaries at top and bottom, that the oscillation frequency is prograde[5] and vanishes when there is zero density stratification. Thus, fluid columns expand as they move away from the rotation axis into lower ambient fluid density and compress as they move towards the axis where the density is higher providing a mechanism to generate "vorticity waves". Moreover, they argued that the effects of compressibility and boundary inclination are additive in the generation of vorticity and therefore, ω_c is influenced by both effects.

In the case A, ω_c increases in absolute value with Co, in agreement with Glatzmaier and Gilman (1981a)'s results. In the case BO, ω_c decreases in absolute value with Co, while the opposite behaviour results for the case BI. The asymptotic laws of Roberts-Busse predict that ω_c behaves inversely with Pr. Since for the case BO, Pr increases towards the interior, the mean Prandtl number along the column increases with Co and leads in a decrease of the absolute value of ω_c. The opposite behaviour in the case BI can be explained following similar arguments.

---

[5] Retrograde drift requires a change in the sign of both gravity and the radial density gradient as these authors claimed.

2.3.2 Results for $\hat{\mu}$ constant, cases C and D

The onset of convection for the cases where the dynamic viscosity is constant, i.e. $\hat{\mu} = 1$, presents the particularity that the local Ekman number changes with radius as $1/\hat{\rho}$. Therefore, the local Ekman number is lower in the regions where the density is larger. From (1.40), constant dynamic viscosity leads to kinematic viscosity $\hat{\nu}$ with $1/\hat{\rho}$ as radial dependence.

In the case C, the thermal diffusivity is constant, i.e. $\hat{\kappa} = 1$, which results in a local Rayleigh number that changes with radius as $\hat{\rho}$, and local Ekman number and local Prandtl number that change with radius as $1/\hat{\rho}$. Since this case has the highest amount of local dimensionless numbers that change with radius, makes it as well the most difficult to study. The dimensionless numbers were defined at the outer boundary choosing $E_o = 3 \times 10^{-4}$ and $Pr_o = 1$.

In the case D, the thermal conductivity is constant, i.e. $\hat{k} = 1$, which results in a local Prandtl number constant throughout the shell. Reformulating the local Rayleigh number in terms of $\hat{\mu}$ and $\hat{k}$ gives a radial dependence as $\hat{\rho}^2$ since both $\hat{\nu}$ and $\hat{\kappa}$ change with radius as $1/\hat{\rho}$.

Tables 2.5 and 2.6 list the results for Ra_c, m_c, ω_c and $c = \omega_c/m_c$ with increasing stratification for the cases C and D. The cases labelled as DO and DI indicate that E was defined at the outer and at the inner boundary respectively.

Figures 2.9 and 2.10 show z-vorticity and temperature at the equatorial plane for two different values of Co. In the case C, the flow is attached to the outer boundary at large Co in the same way as observed for the case A. In the case D, the convection sets in at the inner boundary at small and large Co likewise the case B. Therefore inner boundary values to define the dimensionless numbers are more appropriate in this case. Two solutions for the case DI are given in figure

	Case C: $\hat{\mu} = 1$, $\hat{\kappa} = 1$				Case D: $\hat{\mu} = 1$, $\hat{k} = 1$, $Pr = 1$				
	$Pr_o = 1$, $E_o = 3 \times 10^{-4}$				Case DO: $E_o = 3 \times 10^{-4}$				
Co	$(Ra_c)_o$	m_c	ω_c	c	$(Ra_c)_o$	$(Ra_c)_i$	m_c	ω_c	c
0.0	9.920×10^4	6	-79.03	-13.17	9.920×10^4	9.920×10^4	6	-79.03	-13.17
0.5	1.440×10^5	7	-130.13	-18.59	1.090×10^5	2.970×10^5	7	-94.03	-13.43
1.0	1.882×10^5	9	-192.57	-21.40	1.055×10^5	7.805×10^5	10	-93.88	-9.39
1.5	2.332×10^5	11	-264.44	-24.04	9.215×10^4	1.852×10^6	13	-87.28	-6.69
2.0	2.835×10^5	13	-341.27	-26.25	7.624×10^4	4.163×10^6	16	-88.14	-5.51
2.5	3.435×10^5	14	-422.97	-30.21	6.300×10^4	9.422×10^6	20	-91.22	-4.57
3.0	4.154×10^5	16	-497.22	-31.08	5.203×10^4	$2,102 \times 10^7$	24	-95.89	-4.00
3.5	4.353×10^5	27	-599.84	-22.21	4.243×10^4	4.648×10^6	30	-96.45	-3.22
4.0	4.403×10^5	30	-670.34	-22.33	3.405×10^4	1.015×10^8	37	-94.43	-2.55

Table 2.5: Critical values for onset of convection for $\hat{\mu} = 1$ for the cases C and DO.

	Case D: $\hat{\mu} = 1$, $\hat{k} = 1$, $Pr = 1$				
	Case DI: $E_i = 3 \times 10^{-4}$				
Co	$(Ra_c)_o$	$(Ra_c)_i$	m_c	ω_c	c
0.0	9.920×10^4	9.920×10^4	6	-79.03	-13.17
0.5	6.221×10^4	1.694×10^5	6	-66.13	-11.13
1.0	3.350×10^4	2.478×10^5	7	-47.80	-6.83
1.5	1.612×10^4	3.235×19^5	8	-30.88	-3.86
2.0	7.420×10^3	4.053×10^5	9	-21.45	-2.38
2.5	3.293×10^3	4.901×10^5	9	-16.16	-1.80
3.0	1.477×10^3	5.967×10^5	9	-11.94	-1.33
3.5	6.478×10^2	7.097×10^5	9	-8.47	-0.94
4.0	2.810×10^2	8.684×10^5	9	-5.86	-0.65

Table 2.6: Critical values for onset of convection for $\hat{\mu} = 1$ for the case DI.

2.10. Using outer boundary values to define the dimensionless numbers in the case DO means that the convection at the inner boundary sees a much lower effective Ekman number than in the DI model. Consequently, the scale of the convection is significantly smaller in case DO than in case DI.

2.3.3 Flow structure

In the cases with $\hat{k}$ constant, namely B and D, increasing the stratification degree Co leads to convection more concentrated towards the inner boundary. Therefore, the convection pattern does not exhibit the global character typical of the Boussinesq solutions (see figure 2.7). For global character of convection we imply that there is a large part of the shell where the fluid is in motion. The extreme localisation of convection at large stratifications in the case DO is a consequence of the very low local Ekman numbers in the region where convection develops. For $Co = 4$, E_i is as low as $\sim 3 \times 10^{-6}$.

In the cases with $\hat{\kappa}$ constant, namely A and C, the convection pattern exhibits somewhat a more global character at intermediate to large Co than in the cases B and D. As soon as convection localises closer to the outer boundary, the fluid motion losses its global character.

The spiralling pattern observed in the Boussinesq case is not present when the convection rolls are very much confined towards one of the boundaries, independent of the local Prandtl number. The cases BI and C show clear spirals in the equatorial cuts of z-vorticity since in these cases the local Prandtl number is 1 or less than 1. The prograde tilt is evident in all the cases.

Correlating where convection takes place with its local Rayleigh number, reveals that

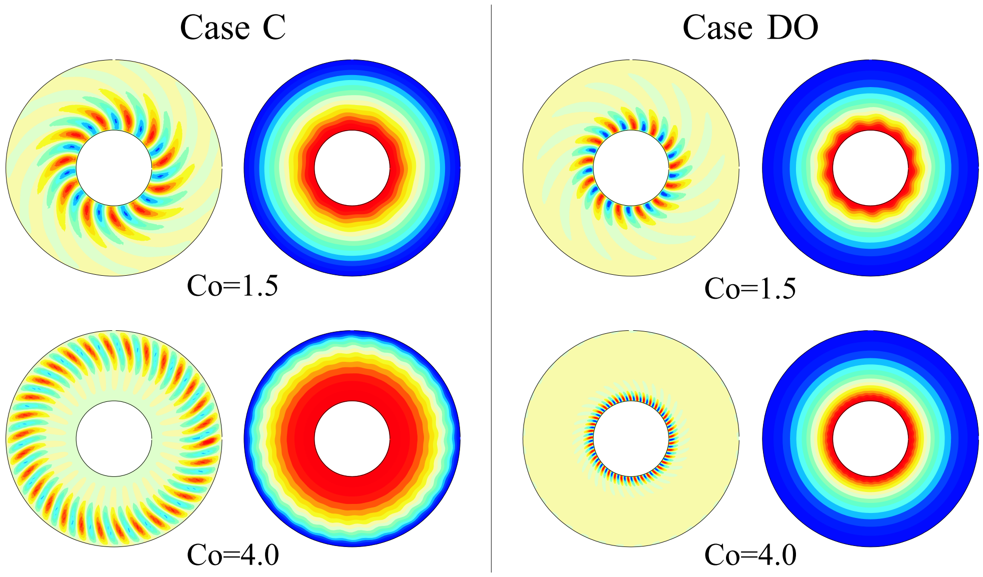

Fig. 2.9: Snapshots of equatorial z-vorticity and temperature at $Ra = 1.1Ra_c$ for the cases C and DO.

for all the cases where convection sets in near the inner boundary the local Rayleigh number is not lowest. In fact, as table 1.2 shows, the local Rayleigh number increases towards the interior as $\hat{\rho}$ for the cases B and C, and as $\hat{\rho}^2$ for the case D. Moreover, the Rayleigh number has the same value throughout the shell for the case A and even there, the preferred pattern of convection for larger stratifications is not adjacent or closer to the inner boundary as one usually obtains in the Boussinesq models. Therefore, there must be another mechanism determining where convection sets in which must be related with the choice of the radial profile of $\hat{k}$.

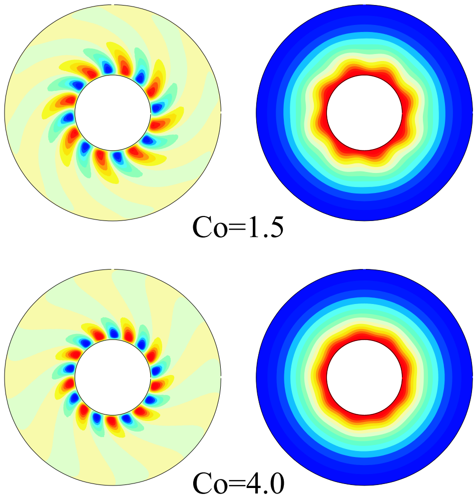

Fig. 2.10: Snapshots of equatorial z-vorticity and temperature at $Ra = 1.1Ra_c$ for the case DI.

Static conductive temperature profile

The location of the convection pattern at onset is governed by the gradient of the static conductive temperature T_s. The term proportional to $\frac{dT_s}{dr}$ in the linearised equation (1.46) inputs energy into the system against its diffusivities, and therefore, the fluid is convectively most unstable where $\frac{dT_s}{dr}$ is steepest.
The static conductive state of the system is described by $\nabla \cdot \left(\hat{k}\nabla T_s\right) = 0$. It has spherical symmetry when $\hat{k} = \hat{k}(r)$ and the imposed boundary conditions have no angular dependence. Fixed temperature $(T_s|_{(r_i,r_o)})$ or fixed heat flux $(\frac{dT_s}{dr}|_{(r_i,r_o)})$ as thermal boundary conditions, don't break the spherical symmetry of the static conductive state and thus, $\frac{\partial T_s}{\partial \theta} = 0$ and $\frac{\partial T_s}{\partial \varphi} = 0$.
The equation

$$\frac{1}{r^2}\frac{d}{dr}\left(r^2\hat{k}\frac{dT_s}{dr}\right) = 0 \tag{2.10}$$

governs the form of $T_s(r)$ for a given thermal conductivity $\hat{k}(r)$ and boundary conditions. With fixed boundary conditions, $T_s|_{r_i} = 1$ and $T_s|_{r_o} = 0$, the analytical solution of (2.10) for $\hat{k} = 1$, i.e. for the Boussinesq case or the anelastic cases B and D is

$$T_s = \frac{r_o r_i}{(r_o - r_i)}\frac{1}{r} - \frac{r_i}{r_o - r_i}. \tag{2.11}$$

This profile decreases as $1/r$ and depends on the geometry of the system through the non-dimensional radii r_i and r_o.

The analytical solution of (2.10) for $\hat{k} = \exp\left(Co\frac{(r_o - r)}{d}\right)$, i.e. for the cases A and C, is much more complicated:

$$\begin{aligned} T_s = B \quad + \quad & A\left\{\frac{Co}{(r_o - r_i)}\exp\left(-Co\frac{r_o}{r_o - r_i}\right)\left[\ln(r) + \sum_{n\geq 1}\left(\frac{Co}{r_o - r_i}\right)^n \frac{r^n}{n\,n!}\right]\right. \\ - \quad & \left.\frac{1}{r}\exp\left[-Co\frac{(r_o - r)}{(r_o - r_i)}\right]\right\} \end{aligned} \tag{2.12}$$

where

$$\begin{aligned} \frac{1}{A} \quad = \quad & \frac{1}{r_o} - \frac{1}{r_i}\exp(-Co) \\ + \quad & \frac{Co}{(r_o - r_i)}\exp\left(-Co\frac{r_o}{r_o - r_i}\right)\left[\ln\left(\frac{r_i}{r_o}\right) + \sum_{n\geq 1}\left(\frac{Co}{r_o - r_i}\right)^n \frac{((r_i)^n - (r_o)^n)}{n\,n!}\right] \end{aligned} \tag{2.13}$$

and

$$B = A\left[\frac{1}{r_o} - \frac{Co}{(r_o - r_i)}\exp\left(-Co\frac{r_o}{r_o - r_i}\right)\left[\ln(r_o) + \sum_{n\geq 1}\left(\frac{Co}{r_o - r_i}\right)^n \frac{(r_o)^n}{n\,n!}\right]\right]. \tag{2.14}$$

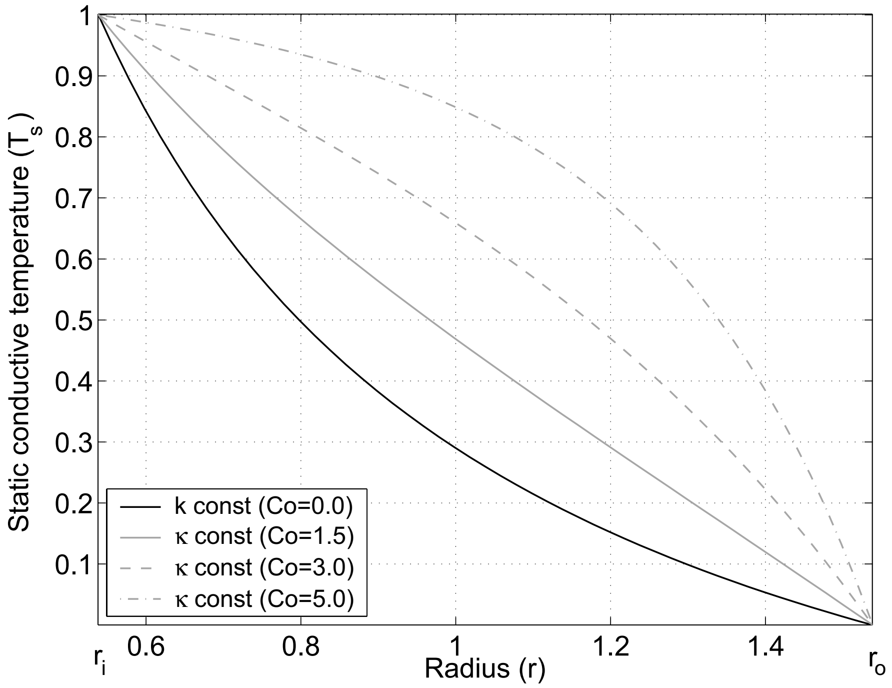

Fig. 2.11: Static conductive temperature profile T_s plotted for different values of Co.

The static conductive profile given in (2.11) is recovered setting $Co = 0$ in the previous solution given by (2.12), (2.13) and (2.14).

The figure 2.11 shows the static conductive temperature profile T_s for different values of Co. The profiles were truncated at $n = 100$ although at $n = 20$ they had already converged. The black solid line corresponds to $Co = 0$ (i.e. incompressible case) as well as when $\hat{k}$ is constant. This profile has the steepest gradient at the inner boundary. When $\hat{\kappa}$ is constant, the profile of $\hat{k}$ changes with Co resulting therefore in different profiles of T_s. The profiles display a transition in which the steepest gradient moves from the inner to the outer boundary with growing Co.

Glatzmaier and Gilman (1981a) found convection adjacent to the outer boundary for their models with $\hat{\nu}$ and $\hat{\kappa}$ constant. In another study, the same authors found convection adjacent to the inner boundary when $\hat{\mu}$ and $\hat{k}$ were considered as constant (Glatzmaier and Gilman, 1981c). According to them, the differences in the solutions appear because in the latter model the velocity was damped in the outer region due to high viscosities. Drew, Zhang and Jones (1995) studied different models where $\hat{\nu}$ and $\hat{\mu}$ were constant, both with constant $\hat{k}$. They found convection concentrated near the inner boundary but they didn't investigate further why in their models convection sets in near the inner boundary while the results by Glatzmaier and Gilman (1981a) show onset near the outer boundary.

Obtaining the static conductive temperature profile is a necessary requirement to study onset of convection as long as the thermal conductivity is not constant. However, this might not be an easy task depending on the form of $\hat{k}$. A qualitative method to see whether convection might set in adjacent to the inner boundary or not comes from a closer inspection to the equatorial cuts of temperature for the cases A and C. In these cases, $\hat{k}$ is larger at the inner boundary than at the outer boundary. We see that there is a large region from the interior of the shell where heat is transported through conduction until the most convectively unstable regions are reached and then heat is more efficiently transported through convection. Therefore, looking at the thermal conductivity profile gives a rough estimate of where convection will set in.

2.4 Summary and conclusions

The onset of convection in rotating spherical systems has been widely studied in Boussinesq models. The well-known asymptotic laws (2.5) that describe convection onset in incompressible fluids, may roughly hold in compressible models as the results in figures 2.3, 2.4 and 2.5 suggest.

In incompressible models with constant gravity background, the dimensionless numbers do not change across the shell. In the presence of density stratification, the diffusivities of the system may be radially dependent and therefore, the dimensionless numbers may eventually have a different value depending on the radius chosen to define them. This complicates the comparison between different cases and in particular with the Boussinesq models. However, when the kinematic viscosity $\hat{\nu}$ and the thermal diffusivity $\hat{\kappa}$ are constant (Case A) all the dimensionless numbers do not change throughout the shell. This particular case not only allows a more direct comparison between compressible and incompressible results but also, provides an appropriate model to describe compressible fluids from a physical point of view. From statistical physics considerations for an ideal gas (see e.g. Reif, 1967), kinematic viscosity and thermal diffusivity are proportional. Therefore, if they change with density, they do it in the same fashion.

The convective instability takes place near the inner boundary in the Boussinesq models as well as in the stratified cases with constant thermal conductivity (Cases B and D). For the models with constant thermal diffusivity (Cases A and C), a transition in the convection onset from near the inner boundary at low Co to near the outer boundary at large Co is accompanied by a sharp increase in the critical wave number m_c. The profiles of static conductive temperature T_s (figure 2.11) show this transition as well and therefore, they can be used to predict where the convection will set in. For all the anelastic models, an increasingly confinement of the convection flow to narrower regions, either adjacent to the inner boundary or to the outer boundary, is observed with growing Co followed by an increase of the wave numbers.

3 3D structure close to onset

3.1 Reformulating the Taylor-Proudman theorem

In §2.2.1 we considered the Navier-Stokes equation (1.37) in the Boussinesq limit of constant density (i.e. $\hat{\rho} = 1$) and under the assumptions of steady and infinitesimal motions, and inviscid and highly rotating fluid, the equation reduced to the geostrophic balance (2.3) which led to the Taylor-Proudman theorem (2.4) after taking the curl.
Let us follow the same steps under the same assumptions for a fluid with an arbitrary reference density $\hat{\rho}(r)$. The geostrophic balance is given by

$$2\hat{\boldsymbol{z}} \times \boldsymbol{u} = -\boldsymbol{\nabla} P \tag{3.1}$$

where P is the reduced pressure given in (1.34). Taking the curl of (3.1) we obtain

$$\boldsymbol{\nabla} \times (\hat{\boldsymbol{z}} \times \boldsymbol{u}) = \hat{\boldsymbol{z}} \boldsymbol{\nabla} \cdot \boldsymbol{u} - \underbrace{\boldsymbol{u} \boldsymbol{\nabla} \cdot \hat{\boldsymbol{z}}}_{=0} + \underbrace{(\boldsymbol{u} \cdot \boldsymbol{\nabla}) \hat{\boldsymbol{z}}}_{=0} - (\hat{\boldsymbol{z}} \cdot \boldsymbol{\nabla}) \boldsymbol{u} = 0, \tag{3.2}$$

where the term with $\boldsymbol{\nabla} \cdot \boldsymbol{u}$ that vanishes in the incompressible case, remains in the compressible case. The anelastic condition $\boldsymbol{\nabla} \cdot (\hat{\rho} \boldsymbol{u}) = 0$ results in

$$\boldsymbol{\nabla} \cdot \boldsymbol{u} = -\frac{1}{\hat{\rho}} \boldsymbol{u} \cdot \boldsymbol{\nabla} \hat{\rho}, \tag{3.3}$$

and therefore, the Taylor-Proudman theorem reformulated for the compressible case when $\hat{\rho} = \hat{\rho}(r)$ is

$$\frac{\partial \boldsymbol{u}}{\partial z} = \frac{u_r}{H_\rho} \hat{\boldsymbol{z}}, \tag{3.4}$$

where H_ρ is the density scale height given in (1.21). Written in cylindrical components, (3.4) is given by

$$\frac{\partial u_s}{\partial z} = 0 \qquad \frac{\partial u_\varphi}{\partial z} = 0 \qquad \frac{\partial u_z}{\partial z} = \frac{u_r}{H_\rho}. \tag{3.5}$$

Thus, (3.5) expresses that the flow perpendicular to the rotation axis is z-independent, while the flow parallel to it is not. The traditional Taylor-Proudman theorem that holds for the incompressible case is recovered when $H_\rho \to \infty$, corresponding to a constant density background.

As we have already discussed in §2.2.1, for an incompressible fluid in fast rotation in a sphere or spherical shell, the non-penetration condition imposes a z-dependence to u_r and u_θ (or to u_s and u_z in cylindrical coordinates) leaving the azimuthal flow as the only truly geostrophic motion when convection develops. This also holds if the fluid is compressible since u_φ is z-independent according to (3.5).

3.2 Is the mass flux geostrophic?

To answer this question, let us follow the same steps under the same assumptions as previously done in section §3.1 but now for the mass flux $\hat{\rho}\boldsymbol{u}$. The geostrophic balance is then given by

$$2\hat{\boldsymbol{z}} \times (\hat{\rho}\boldsymbol{u}) = -\hat{\rho}\boldsymbol{\nabla} P. \tag{3.6}$$

Taking the curl of (3.6) and using the anelastic condition $\boldsymbol{\nabla} \cdot (\hat{\rho}\boldsymbol{u}) = 0$ results in

$$\frac{\partial(\hat{\rho}\boldsymbol{u})}{\partial z} = \frac{1}{2}\boldsymbol{\nabla}\hat{\rho} \times \boldsymbol{\nabla} P, \tag{3.7}$$

which written in cylindrical components gives

$$\frac{\partial(\hat{\rho}u_s)}{\partial z} = -\frac{1}{2s}\frac{\partial\hat{\rho}}{\partial z}\frac{\partial P}{\partial\varphi} \qquad \frac{\partial(\hat{\rho}u_\varphi)}{\partial z} = \frac{1}{2}\left(\frac{\partial\hat{\rho}}{\partial z}\frac{\partial P}{\partial s} - \frac{\partial\hat{\rho}}{\partial s}\frac{\partial P}{\partial z}\right) \qquad \frac{\partial(\hat{\rho}u_z)}{\partial z} = \frac{1}{2s}\frac{\partial\hat{\rho}}{\partial s}\frac{\partial P}{\partial\varphi} \tag{3.8}$$

where

$$\frac{\partial\hat{\rho}}{\partial z} = -\frac{\hat{\rho}}{H_\rho}\frac{z}{\sqrt{s^2+z^2}} \quad \text{and} \quad \frac{\partial\hat{\rho}}{\partial s} = -\frac{\hat{\rho}}{H_\rho}\frac{s}{\sqrt{s^2+z^2}}. \tag{3.9}$$

As (3.8) expresses, the three components of the mass flux cannot be z-independent simultaneously unless P is constant, or $\boldsymbol{\nabla} P \parallel \boldsymbol{\nabla}\hat{\rho}$, which implies that P varies only with radius. In principle, there are no physical grounds to assume one of the previous conditions to force the mass flux to be z-independent.
Let us express (3.8) in terms of velocity components and their z-derivatives:

$$\frac{\partial(\hat{\rho}u_s)}{\partial z} = \frac{\partial\hat{\rho}}{\partial z}u_s \qquad \frac{\partial(\hat{\rho}u_\varphi)}{\partial z} = \frac{\partial\hat{\rho}}{\partial z}u_\varphi \qquad \frac{\partial(\hat{\rho}u_z)}{\partial z} = \frac{\partial\hat{\rho}}{\partial z}u_z + \hat{\rho}\frac{u_r}{H_\rho} \tag{3.10}$$

where the components of $\frac{\partial\boldsymbol{u}}{\partial z}$ were replaced by (3.5). Only at the equatorial plane (i.e. $z=0$) $\frac{\partial\hat{\rho}}{\partial z} = 0$ however, depending on how large is H_ρ, there can be a region around the equatorial plane characterised by $z \approx 0$ where $\frac{\partial\hat{\rho}}{\partial z} \approx 0$ and therefore, some degree of z-independence is recovered. In the incompressible limit, $H_\rho \to \infty$ and the mass flux, which is actually the velocity, is z-independent recovering the Taylor-Proudman theorem as given in §2.2.1. The figure 3.1 shows a sketch of a spherical shell when the fluid is stratified that can better explain (3.10). A roll of

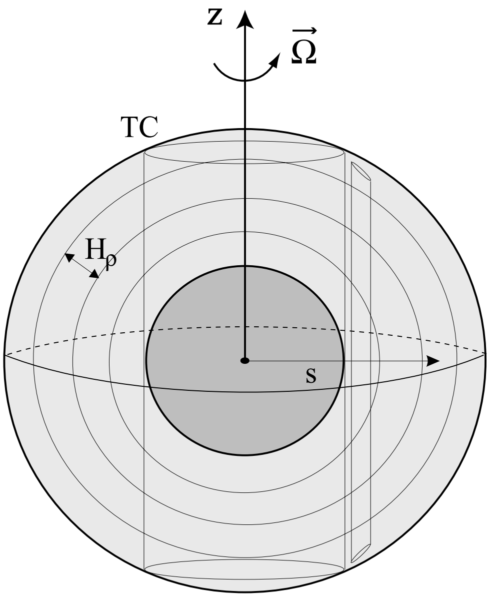

Fig. 3.1: Sketch of the spherical shell for a stratified fluid with $Co = 4$. H_ρ is the density scale height, s is the cylindrical radial coordinate and TC stands for "tangent cylinder", or the cylinder tangent to the inner boundary at the equator.

mass flux adjacent to the TC (tangent cylinder, i.e. cylinder tangent to the inner boundary at the equator) crosses as many density scale heights as given by the value of Co. Around the equatorial region, a roll changes its density by around one H_ρ. When Co increases, this region gets smaller and therefore, there is a strong variation of $\hat{\rho}$ with z. When Co decreases the effect can be resembled to moving the convection roll outwards, crossing therefore less number of scale heights.

Similarly as for the velocity components, $(\hat{\rho}u)_s$ and $(\hat{\rho}u)_z$ cannot be geostrophic due to the non-penetration condition together with the fact that the most unstable convective mode is symmetric with respect to the equatorial plane. Additionally, the condition (3.8) imposes z-dependence to $(\hat{\rho}u)_\varphi$ leaving no geostrophic mass-flux component possible.

Evidences of geostrophy are manifested in the zonal flow obtained as the azimuthal average of the azimuthal flow. In the Boussinesq case, the numerical simulations at $Pr = 1$, $E = 3 \times 10^{-4} - 10^{-5}$ performed by Christensen (2001, 2002) show a striking degree of geostrophy in the zonal flow that persists at very strongly supercritical regime. Zhang (1992), on the other hand, pointed out the role played by the Prandtl number in the generation of zonal flow in which there is an increasing loss of geostrophy with increasing Prandtl number. At moderate-low Prandtl numbers, the geostrophic zonal flow is generated by strong non-linear interactions of the spiralling columnar rolls, while at high Prandtl numbers, the primary mechanism generating zonal flow is the thermal wind, responsible for its z-dependence.

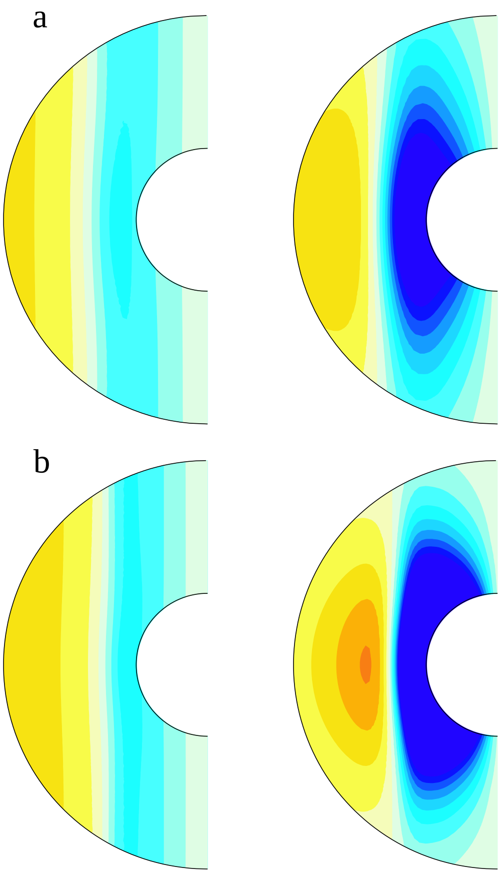

Fig. 3.2: Zonal flow for the velocity (left) and the mass flux (right) for two selected cases at $Ra = 1.1Ra_c$ and $E = 3 \times 10^{-4}$. a) Case A with $Co = 1.5$. b) Case BI with $Co = 3$. The colour table is saturated for the mass flux to highlight its ageotrophic nature. Yellow: prograde, blue: retrograde.

In the compressible case, whether the zonal velocity or the zonal mass flux remains geostrophic can be seen in figure 3.2. It shows zonal flow for the velocity (left column) and for the mass flux (right column) for two selected cases in which weak zonal flow is present close to onset at $Ra = 1.1Ra_c$. The relations (3.5) and (3.8) for the azimuthal flow are fulfilled since these results show a high level of geostrophy for the zonal velocity and a high level of ageostrophy for the zonal mass flux especially at higher latitudes. This behaviour of the zonal flow towards geostrophy persists at more supercritical regimes.

3.3 Velocity vs. mass flux

Since the physically relevant limit in the giant planets' atmospheres is $E \rightarrow 0$ corresponding to fast rotation and low viscosity, the atmospheric interior is believed to be inviscid for energetic considerations. Thus, as Guillot et al. (2004) argued, convective velocities should be larger near the surface of the planet where the density is smaller since low density material requires higher velocities to transport the same energy. On the other hand, it has been often argued in the stellar physics field that motion will conserve the mass flux $\hat{\rho}\boldsymbol{u}$ and therefore produce large velocities near the surface. However, as Gough et al. (1976) pointed out, large damping at low density may result in smaller superficial speeds than those at greater depths.

Figures 3.3, 3.4 and 3.5 show equatorial velocity and mass flux at $Ra = 1.1Ra_c$ for the models A, BI and C respectively. The advantage of looking at the equatorial plane is that the flow has no component perpendicular to that plane, i.e. $u_z = 0$. The size of the arrows emphasises flow structure and therefore, the flow strength cannot be compared between single pictures.

Figure 3.3 shows at $E = 10^{-2}$ and $Co = 1.5$ that convection is global taking place in the entire shell. There is as well, some evidence of larger equatorial velocities close to the outer boundary where the density is smaller. The corresponding Boussinesq case shows a similar increase of velocity close to the outer boundary, however it is not that large compared to the interior as it is when $Co = 1.5$. The mass flux field, on the other hand, seems to be more uniform in the region where convection takes place. At higher values of Co, convection onset is adjacent to the outer boundary and the velocity is damped inwards consistent with the fact that in principle there is no fluid motion in the interior. The mass flux field shows at higher Co also a much more global character with uniform behaviour compared to the velocity. At higher Ekman numbers the region where convection takes place actively is more confined and makes more difficult to discern the behaviour of the fields. However, at $Co = 1.5$ the flow close to the outer boundary seems to be more damped for the mass flux relative to the flow close to the inner boundary, while this seems not to be the case for the velocity. For larger values of Co, it can be recognised that the velocity field decays inwards much more rapidly than the mass flux field.

Figure 3.4 shows equatorial velocity and mass flux for the cases BI and BO. Convection sets adjacent to the inner boundary and the high degree of confinement of the convection makes nearly impossible in the case BO, as well as in the cases DI and DO (not shown), to distinguish any significant difference between velocity and mass flux patterns. For the case BI, the equatorial velocity reveals an azimuthal prograde flow at the outer region which is not evident for the mass flux. This flow is a consequence of the small local Prandtl number ($Pr \ll 1$) closer to the outer boundary. Therefore, the inertia force is larger compared to the interior and as a consequence, the Reynolds stresses (Zhang, 1992b), which are responsible for the generation of axisymmetric azimuthal flow due to non-linear interactions between tilted rolls, are larger as well.

The effect of very low local Prandtl number is also observed in figure 3.5, this time at the inner boundary. The velocity field decays inwards, however in the inner region

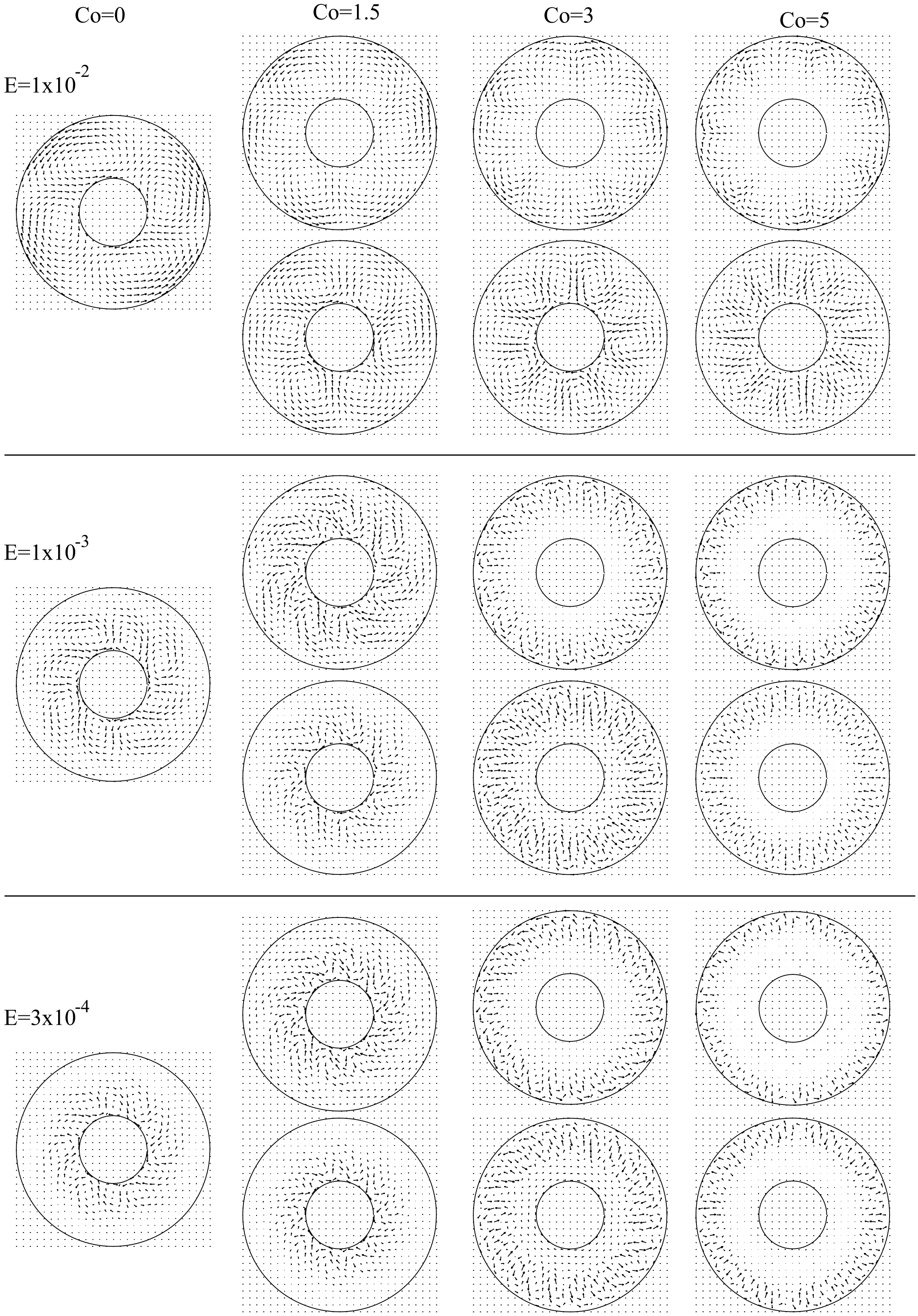

Fig. 3.3: Snapshots at the equatorial plane at $Ra = 1.1Ra_c$ for the case A at $Pr = 1$, $E = 10^{-2}$, $E = 10^{-3}$ and $E = 3 \times 10^{-4}$, and $Co = 0$, $Co = 1.5$, $Co = 3$ and $Co = 5$. For every E velocity is plotted in the upper row and mass flux in the lower one.

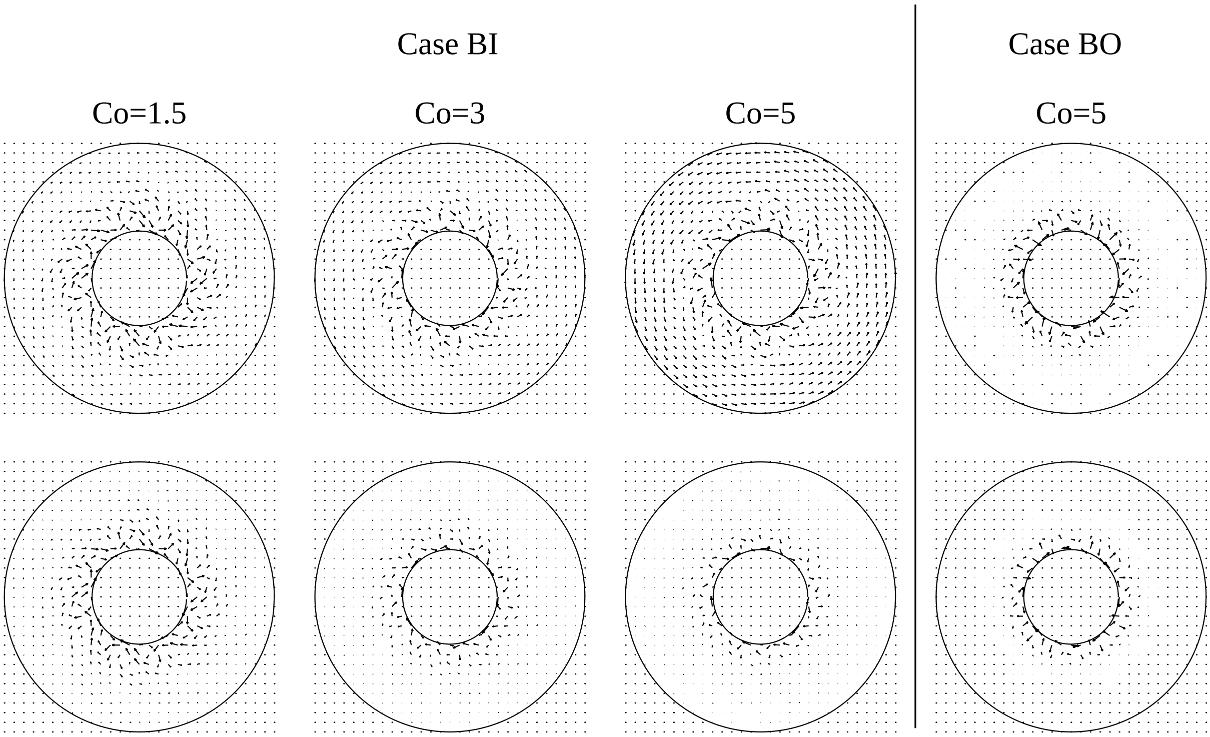

Fig. 3.4: Snapshots at the equatorial plane at $Ra = 1.1Ra_c$, $E = 3 \times 10^{-4}$, and $Co = 1.5$, $Co = 3$ and $Co = 5$ for the cases BI and BO. Velocity field is plotted in the upper row and mass flux in the lower one.

there is retrograde azimuthal flow as the mass flux field shows.

The equatorial flow patterns for the different cases suggest that damped velocities in the interior do not always mean absence of momentum there. If the fluid is not stagnant close to the inner boundary, weak velocities can lead to moderate momentum due to the presence of large ambient density. Or vice-versa, regions of weak momentum close to the outer boundary do not necessarily imply low velocities.

Figures 3.6 and 3.7 show the azimuthal average of $\sqrt{u^2}$ and $\sqrt{(\hat{\rho}u)^2}$ plotted in the meridional plane, where $u = |\boldsymbol{u}|$. The contribution of the zonal flow, i.e. φ-average

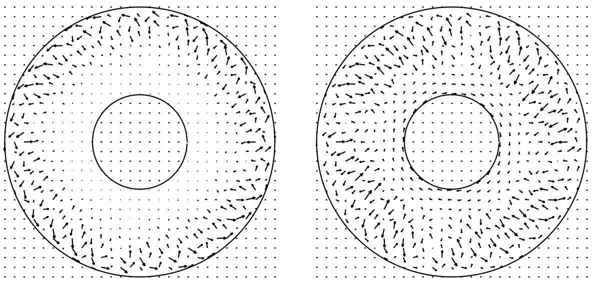

Fig. 3.5: Snapshots at the equatorial plane at $Ra = 1.1Ra_c$, $E_o = 3 \times 10^{-4}$ and $Co = 5$ for the case C. Velocity field is plotted on the left and mass flux on the right.

of the φ-component of the flow, was removed. The contour steps were chosen to highlight differences in flow pattern instead of strength. The increase of velocity towards the outer boundary, observed at $E = 3 \times 10^{-4}$ in figure 3.6 cannot be attributed directly to lower ambient density since the same behaviour is also observed in the Boussinesq case. In all the cases the mass flux shows a tendency to geostrophy around the equatorial plane and increasing ageostrophy at higher latitudes as (3.10) predicted.

3.4 Column bending

A simple model to describe Jovian atmospheres dynamics was proposed by Busse (1976), in which convection columns are organised in concentric layers outside the tangent cylinder. The mechanism producing the zonal flow, or “zones” and “belts” as he said, was related to the non-linear advection of momentum by columnar convection assuming that every layer of convection columns corresponds to a “zone” or a “belt”. Therefore, according to his model, the maximum latitude at which banded appearance is found gives a rough estimate of where is located the molecular/metallic hydrogen boundary.

At onset of convection Glatzmaier and Gilman (1981a) reported that convective columns bend towards the poles with increasing compressibility. The idea that the convective rolls might be curved somehow parallel to the planet’s meridian is already present as a brief discussion in Busse (1976). They are usually called “banana cells”, however, the meaning given to this expression sometimes differ in the literature. For example, Busse and Carrigan (1976) called “banana-shaped convection cells” to the pattern obtain experimentally in a very thin shell of 1/16 width and therefore, this bending towards the poles is more likely to be a geometrical response of convection due to limited space in the shell.

Under the assumption that the simple model of Busse (1976) does give an approximated picture of convection in the Jovian atmospheres, the existence of some degree of bending towards the poles leads to a molecular/metallic hydrogen transition located closer to the exterior than expected.

The bending of the rolls is shown in Glatzmaier and Gilman (1981a) as a plot of axis of helices for different compressibilities included the incompressible case. At $T = 10^2$ ($\equiv E = 2 \times 10^{-1}$), the axes of the rolls are parallel to the spherical surface for the incompressible and compressible cases. At $T = 10^5$ ($\equiv E = 6.3 \times 10^{-3}$) and small stratifications the convective columns are parallel to the rotation axis while at larger stratifications the axes of the columns bend toward the poles at mid-latitudes. The results of Glatzmaier and Gilman (1981a) suggest that large enough compressibilities can overcome the constraint imposed by rotation restoring partially the spherical geometry. We seek for evidence of columns bending towards the poles in our

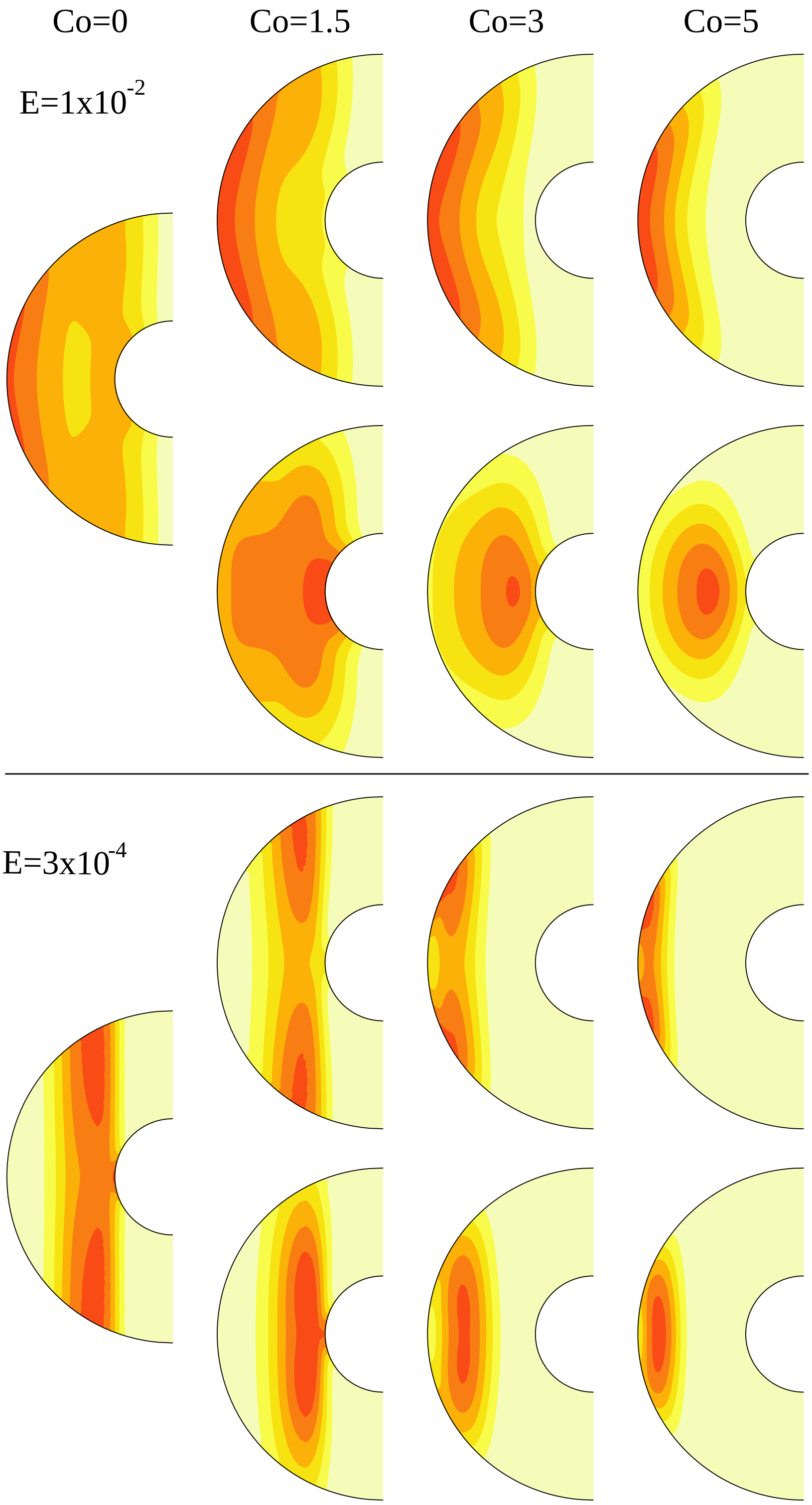

Fig. 3.6: Azimuthal average of $\sqrt{u^2}$ (upper row) and $\sqrt{(\hat{\rho}u)^2}$ (lower row) for the case A at $E = 10^{-2}$ and $E = 3 \times 10^{-4}$, and $Co = 0$, $Co = 1.5$, $Co = 3$ and $Co = 5$. The contour steps were chosen to highlight differences in flow pattern instead of strength.

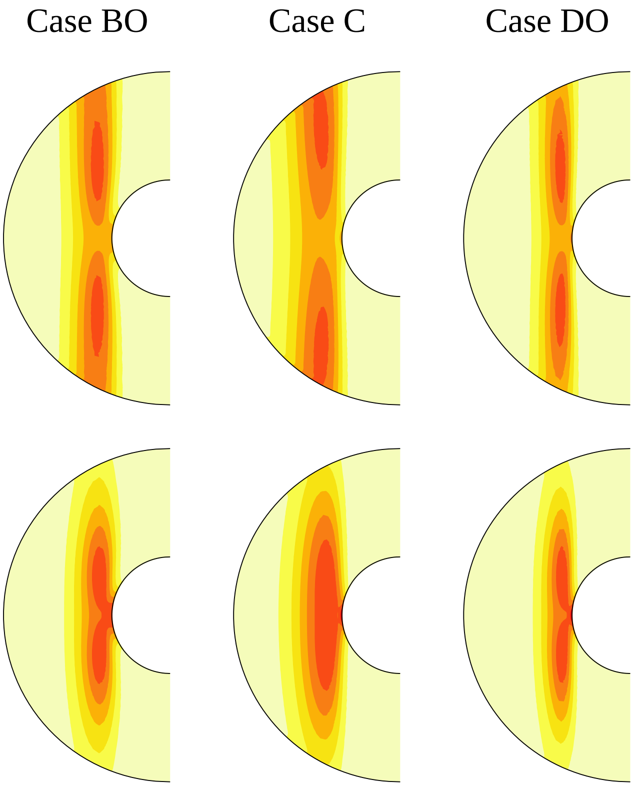

Fig. 3.7: Azimuthal average of $\sqrt{u^2}$ (upper row) and $\sqrt{(\hat{\rho} u)^2}$ (lower row) for the cases BO, C and DO at $E = 3 \times 10^{-4}$ (E_o for the cases C and DO) for $Co = 1.5$. The contour steps were chosen following the same criterion as in figure 3.6.

results at low rotation rates trying to emulate what Glatzmaier and Gilman (1981a) did. Therefore, we considered $\hat{\kappa}$ and $\hat{\nu}$ constant, $Pr = 1$ and low rotation rates as they did.

Figure 3.8 shows meridional slices of azimuthal velocity u_φ (upper row), and z-vorticity (lower row, left) and temperature (lower row, right) at the equatorial plane at $Ra = 1.1 Ra_c$, $Pr = 1$, for $E = 10^{-1}$ and $E = 10^{-2}$, in the Boussinesq case and compressible case A. The Boussinesq case is ageostrophic at $E = 10^{-1}$ although the convection pattern remains quite symmetric with respect to the equatorial plane as a consequence of the rotation, even if it is slow. The presence of columns bending towards the poles is not manifested in every slice. The usual concept of convective "column" from rotating convection is not easily identified in a system that develops $m = 2$ azimuthal symmetry with global convection taking place in the entire shell. At $E = 10^{-2}$ the meridional slices in the Boussinesq case exhibit a striking degree of geostrophy characteristic of a fast rotation regime and the equatorial z-vorticity already shows the spiral shape characteristic at higher rotation rates for moderate Prandtl number.

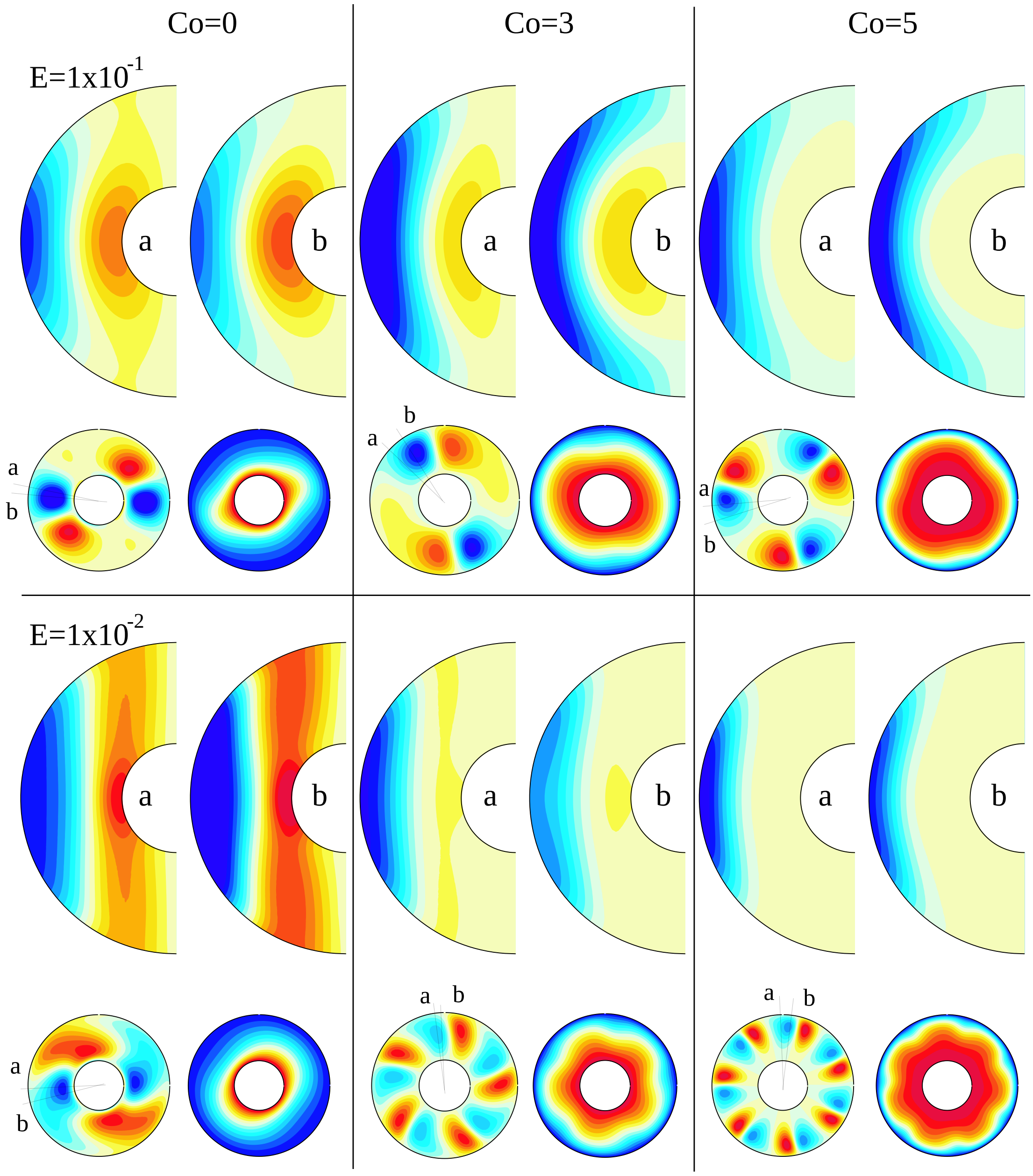

Fig. 3.8: Meridional slices of u_φ (upper row), and z-vorticity (lower row, left) and temperature (lower row, right) at the equatorial plane at $E = 10^{-1}$ and $E = 10^{-2}$ for the cases $Co = 0$, $Co = 3$ and $Co = 5$, at $Ra = 1.1Ra_c$ and $Pr = 1$ for the case A. Red: prograde, anticlockwise and hot, blue: retrograde, clockwise and cold, for u_φ, z-vorticity and temperature, respectively.

The compressible results at $E = 10^{-1}$ seem to show convection with higher degree of bending towards the poles compared to the Boussinesq case. However, whether there is bending or not at $E = 10^{-2}$ is not clear from the slices. The influence of

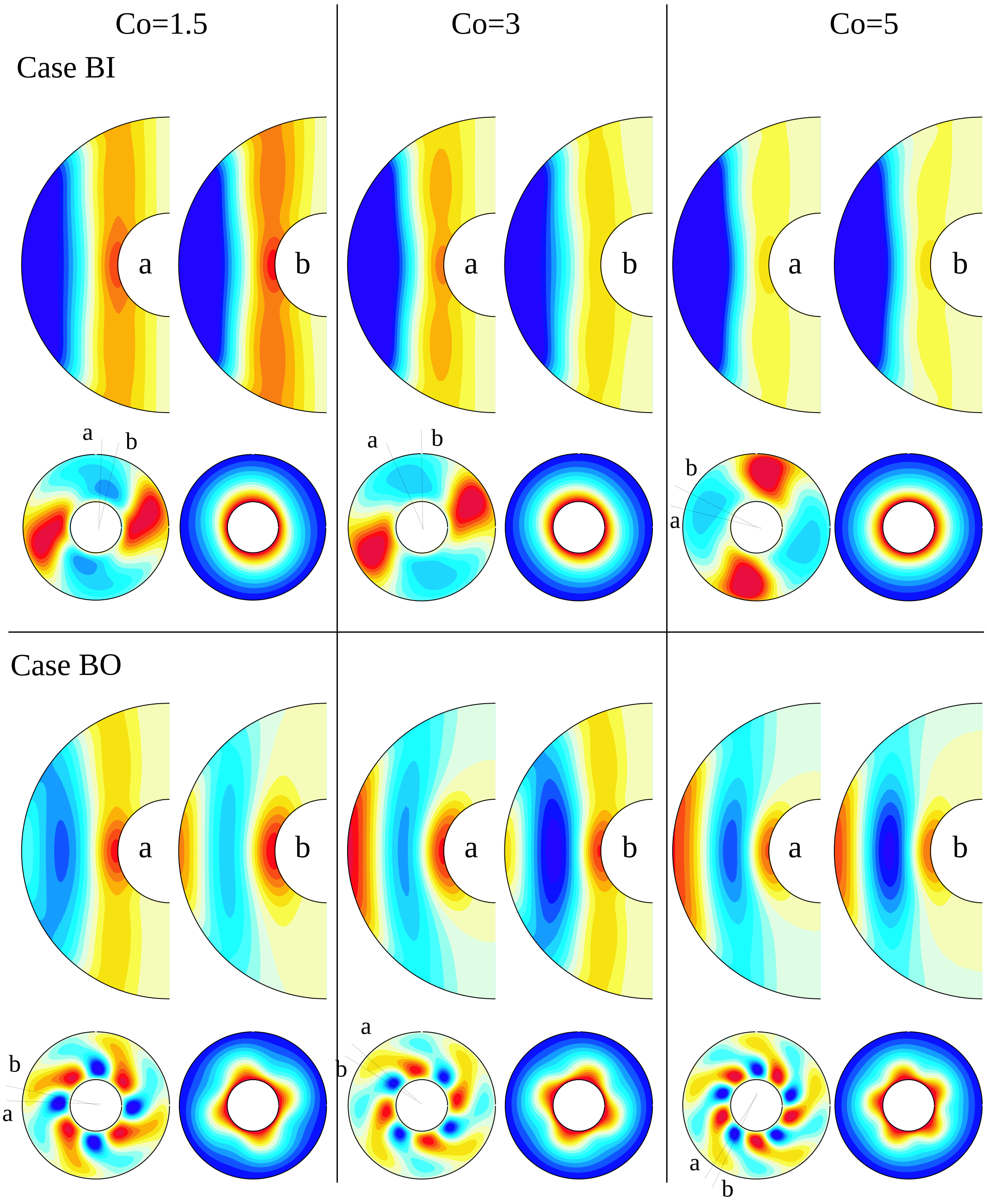

Fig. 3.9: Meridional slices of u_φ (upper row), and z-vorticity (lower row, left) and temperature (lower row, right) at the equatorial plane at $E = 10^{-2}$, $Co = 1.5$, $Co = 3$ and $Co = 5$, at $Ra = 1.1Ra_c$ for the cases BI and BO. Red: prograde, anticlockwise and hot, blue: retrograde, clockwise and cold, for u_φ, z-vorticity and temperature, respectively.

compressibility to bend the convection pattern towards the poles seems to be present at very low rotation rates, however, the high degree of column bending observed by Glatzmaier and Gilman (1981a) is not evident in our results. In addition, the fact that the convection pattern sets closer to the outer boundary at higher compressibilities may impose a bending in the convection pattern as a result of the curved outer boundary when the constraint of rotation is not that strong.

To reduce the effects on the convection pattern that may appear in the case A at moderate-large compressibilities due to convection onset closer to the outer boundary, we studied the cases BO and BI. The Ekman number was chosen as 10^{-2} since rotation is still low and the pattern of convection is more columnar-like. The results in figure 3.9 shows the influence of the Prandtl number in the convection. For the case BI, despite of the low level of azimuthal symmetry ($m = 2$) the pattern exhibits a high degree of geostrophy while for the case BO, the slices show ageostrophy with eventually bending towards the poles and apparent bending towards the outer boundary. This last case points out that the view of a convection column in some cases may be highly idealised and therefore, local changes in the structure of a single "column" could be misinterpreted as a global bending effect.

Glatzmaier and Gilman (1981a) explained the mid-latitude bending of the columns as a consequence of additional terms becoming important in the vorticity equation. Since H_ρ drops off near the outer boundary, and φ-gradients are large due to the small longitudinal dimension (i.e. large m), the Taylor-Proudman condition does not apply for high rotation rates and large stratifications as they argued. Following these arguments, it is, however, not clear which is the mechanism producing the bending at lower T where m is much smaller.

The little evidence of column bending in our results could be related to the fact that the density scale height H_ρ is constant in our model, and radially decreasing in Glatzmaier and Gilman (1981a)'s model. A few simulations were performed with $\hat{g} = r/r_o$ since the density scale height decreases linearly with radius[1]. With a degree of stratification Co_{glin} with the same density ratio $\hat{\rho}_i/\hat{\rho}_o$ as for $Co = 5$ when the background density is constant, the results at $E = 10^{-2}$ for the cases A, BI and BO (not shown) do not show a much different behaviour than the respective results with constant reference gravity. This suggests that outside from local differences and flow strength, radially dependent scale height does not influence much the flow pattern.

3.5 Summary and conclusions

The Taylor-Proudman theorem for an incompressible fluid reveals the tendency of convective motions to be nearly z-independent. The non-penetration condition together with the fact that the most unstable convective solution is symmetric with respect to the equatorial plane leaves the azimuthal flow as the only motion component that can be geotrophic in a spherical system. For a compressible fluid with radial density background, the original Taylor-Proudman theorem modifies according to (3.5), but the azimuthal velocity remains z-independent. For the mass flux, on the other hand, there is no possible geostrophic component as reveals the modified Taylor-Proudman theorem (3.10) obtained with the mass flux as motion variable.

---

[1] When $\hat{g} = r/r_o$ the reference density is $\hat{\rho} = \exp\left[\frac{Co}{2dr_o}(r_o^2 - r^2)\right]$ which gives a radial density scale height $\left(H_\rho\right)_{glin} = \frac{d}{Co}\frac{r_o}{r} = \frac{d}{Co_{glin}}$.

The ageostrophy in the mass flux can be seen in the zonal flow (figure 3.2) as well as in the azimuthal average of the total flow (figures 3.6 and 3.7). However, the equatorial mass flux patterns (figures 3.3, 3.4 and 3.5) exhibit a tendency to be more uniform compared to their velocity counterparts.

The bending of the columns towards the poles by Glatzmaier and Gilman (1981a) suggests that the constraint imposed by rotation can be overcomed when the compressibility is large enough. Although this is an interesting feature, our results show no significant column bending. The global character of the convection as well as the very low azimuthal symmetry result in a loss of the usual concept of column. In the cases where a columnar convection structure is observed, local distortions of the flow may be misinterpreted as bending. In the cases where convection sets in closer to the outer boundary, a bending towards the poles may be the response to the curved outer boundary at low rotation rates.

The number of density scale heights in the molecular hydrogen envelope of the giant planets is uncertain. However, there are some estimates from mixing length theory of the pressure scale height H_P in Jupiter. In the uppermost atmosphere $H_P \sim 20km$ while in the deeper molecular region $H_P \sim 3000km$ (Guillot et al., 2004). Thus, H_P is very much smaller close to the outer boundary.

A very rough estimate of how many density scale heights there are in Jupiter's molecular envelope can be performed using that $H_\rho = \gamma H_P$ for an ideal gas. Taking $H_P \sim 3000km$ and $\gamma = 7/5$, value for a diatomic gas, it results $H_\rho \sim 4200km$. Assuming that H_ρ is constant in the outer 20% of the planet (which is $\sim 14000km$ of $\sim 70000km$ of planetary radius) the number of density scale heights is around 4. Since H_ρ is much smaller close to the outer boundary, this estimate gives only a rough idea of the minimum number of density scale heights.

The Ekman number is very low, $\sim 10^{-15}$ for Jupiter (Guillot et al., 2004). Under the assumption that column bending is a response of large compressibilities over rotation (Glatzmaier and Gilman, 1981a), it could be speculated whether it manifests in the giant planets if it would be possible to estimate more accurately how H_ρ changes with radius and in consequence the number of density scale heights.

4 Finite amplitude convection

In previous chapters it was investigated the onset of compressible convection for different fluid properties. In the non-linear regime, the Rayleigh number adds an additional degree of freedom to the parameter space, therefore, only cases at constant local Ekman number were studied to limit the number of calculations.

4.1 General features of incompressible convection

Thermal convection in rotating spherical systems has been widely explored in the non-linear regime in the Boussinesq approximation (Zhang, 1992b; Sun et al., 1993; Zhang, 1994; Tilgner and Busse, 1997; Ardes et al., 1997; Grote and Busse, 2001; Christensen, 2001; Christensen, 2002; Simitev and Busse, 2003). Increasing the Rayleigh number, various scenarios occur depending on the choice of the other parameters. Three main groups can be distinguished depending on the Prandtl number (see §2.2.2).
(I) At $Pr \lesssim 1$, the different non-linear regimes in the spiralling-columnar convection are the following:

- **drifting columns**, characteristic close to onset;
- **vacillating convection** in amplitude, where eventually, some transitions in the vacillating regime are identified increasing Ra;
- **chaotic convection**, characteristic at moderate Ra, where the symmetry about the equatorial plane is still retained to a good degree;
- **intermittency** in time, where bursts of convection fill the entire volume outside the tangent cylinder; and
- **chaotic convection** in the strongly supercritical regime, which fills the entire volume, although, some degree of symmetry about the equatorial plane is still present.

Close to onset, convection forms outside the tangent cylinder where the Taylor-Proudman condition is less restricting: the gravity vector is perpendicular to the rotation axis at the equatorial plane. In the polar regions, on the other hand,

i.e. inside the tangent cylinder, vertical motions are inhibited due to the constraint of rotation. Therefore, polar regions are nearly stagnant until the Rayleigh number is several times supercritical. The required Ra for onset of convection inside the tangent cylinder depends on E and Pr (Sun et al., 1993; Tilgner and Busse, 1997; Ardes et al., 1997; Grote and Busse, 2001; Christensen, 2001).
(II) At $Pr > 1$ the scenario for the rotating non-linear convection is by far not as detailed as at $Pr \lesssim 1$. The Prandtl number is believed to be moderate to small in many geophysical systems, with the exception of planetary mantles since Pr is very large due to very high viscosity. However,

- **drifting columns** and
- **vacillating convection** have been identified in the weakly non-linear regime (Zhang, 1992a; Tilgner and Busse, 1997), as well as
- **chaotic convection** up to moderate Ra (Tilgner and Busse, 1997).

(III) The transition between thermal inertial waves and spiralling-columnar convection was studied by Ardes et al. (1997). Thermal inertial waves are preferred at onset when $E > E_c$ and spiralling-columnar modes for $E < E_c$, where $E_c \sim P^{1/2}$. Thus, thermal inertial waves are more likely at small Pr since E is generally small for the problems considered here. In the non-linear regime, some aspects of the thermal inertial waves have been studied by Simitev and Busse (2003) for $Pr = 0.025$ and Ekman numbers of order 10^{-5}, where

- **drifting convection**,
- **vacillations** and
- **chaotic convection** have been identified as well as a tendency to
- **intermittency** in time.

4.2 Supercritical compressible convection

4.2.1 Global measures of the solution

Kinetic energy density

The total kinetic energy density E_k is given by

$$E_k = \frac{\dfrac{1}{2V_s}\displaystyle\int_{V_s} \hat{\rho} u^2 dV}{\dfrac{1}{V_s}\displaystyle\int_{V_s} \hat{\rho} dV} \tag{4.1}$$

where V_s is the volume of the spherical shell. The kinetic energy density is the sum of the poloidal and the toroidal kinetic energy densities, E_{pol} and E_{tor}, as given in §C.2. E_{pol} is a measure of the vigour of the convection since the radial component of the flow enters only in the poloidal scalar potential. The axisymmetric part of the toroidal kinetic energy density, given by the terms with $m = 0$, describes the kinetic energy in the zonal flow.

Nusselt number

The Nusselt number Nu is a dimensionless number that measures the efficiency of the convection as mechanism to transport heat. It is defined as

$$Nu = \frac{\text{spherically averaged total heat flux}}{\text{conductive heat flux}}, \tag{4.2}$$

where the conductive heat flux is $-\hat{k}\boldsymbol{\nabla}T_s$ with $T_s = T_s(r)$. At the boundaries, the total heat flux is transported only through conduction and therefore, the Nusselt number at the boundaries can be written as

$$Nu_{(i,o)} = \frac{-\hat{k}\dfrac{\partial T}{\partial r}\Big|_{(r_i,r_o)}}{-\hat{k}\dfrac{dT_s}{dr}\Big|_{(r_i,r_o)}} \tag{4.3}$$

where $\partial T/\partial r$ is the average over a spherical surface. When convection takes place Nu is larger than 1, while $Nu = 1$ indicates that the heat is transported only through conduction.

For the Boussinesq case or the anelastic case with $\hat{k} = 1$,

$$Nu_i = -\eta\frac{\partial T}{\partial r}\Big|_{r_i} \quad \text{and} \quad Nu_o = -\frac{1}{\eta}\frac{\partial T}{\partial r}\Big|_{r_o}. \tag{4.4}$$

For the anelastic case with $\hat{k} = \exp\left(Co\dfrac{(r_o - r)}{d}\right)$,

$$Nu_i = \frac{\eta^2\exp(Co)}{A(1-\eta)^2}\frac{\partial T}{\partial r}\Big|_{r_i} \quad \text{and} \quad Nu_o = \frac{1}{A(1-\eta)^2}\frac{\partial T}{\partial r}\Big|_{r_o}, \tag{4.5}$$

where the constant A is given in (2.13) in §2.3.3.

4.2.2 Starting conditions and numerical resolution

At $Ra = 1.1Ra_c$ the calculations were started imposing a temperature perturbation with $(\ell, m) = (m_c, m_c)$ and maximum at mid-depths. However, in a few cases with onset of convection close to the outer boundary, the maximum perturbation was set close to the outer boundary. For some higher supercritical calculations, a previous calculation obtained at lower Ra was taken as initial state. In all the simulations, no assumed azimuthal symmetry was imposed, and the calculations were integrated in time until the stationary or chaotic equilibrated state was reached.

A proper resolution test is difficult to perform because all the different aspects of the solution have to be compared. However, Christensen et al. (1999) and Glatzmaier (1988) suggested that the spectral power of kinetic energy spectra is a good proxy for the convergence of the solution. For the Boussinesq case, Christensen et al. (1999) established that the calculations can be assumed reasonably resolved when the spectral power of kinetic energy drops by more than 2 orders of magnitude. To check whether this criterion also applies in our case, we performed a resolution study comparing the quantitative behaviour of time-averaged properties of the solution with different resolutions in a similar way as Christensen et al. (1999) did.

Table 4.1 shows time-averaged global properties for the case A at $Ra = 2.2Ra_c$, for different resolutions at $Co = 1.5$ and $Co = 5$. The time series exhibit a chaotic behaviour in both cases (see figures 4.2 and 4.6), and the essential difference between $Co = 1.5$ and $Co = 5$ is that convection sets in close to the inner or outer boundary respectively (see §2.3.1). In both cases, the differences in energy densities drop to less than 1% for the highest two resolutions. Figure 4.1 shows the time-averaged spectrum of kinetic energy density for $Co = 5$ with resolution given by $(n_r, n_j, \ell_{max}) = (49, 160, 53)$, where n_r is the number of radial grid points, n_j is the number of grid points in θ and ℓ_{max} is the maximum harmonic degree ℓ. A decay in the spectral power of the kinetic energy of at least 4 orders of magnitude is required to resolve the calculations adequately.

At low to moderate Rayleigh numbers this criterion is fulfilled in nearly all the calculations. In extreme cases where the time step had to be very small, with the consequent increase of calculation time, the choice of a less finer grid made the calculation possible in a reasonable computing time. In some other cases where the small

Test	(n_r, n_j, ℓ_{max})	E_k	$(E_{tor}^{m=0}/E_k) \times 100$	$(E_{pol}/E_k) \times 100$	Nu
$Ra = 2.2Ra_c$,	(33,96,32)	8.85×10^2	72.73	12.60	1.269
$Co = 1.5$	(41,128,42)	3.33×10^3	67.68	12.42	1.119
	(49,160,53)	3.35×10^3	67.72	12.39	1.119
$Ra = 2.2Ra_c$,	(49,160,53)	1.35×10^2	67.15	18.27	1.141
$Co = 5.0$	(65,192,64)	1.39×10^2	67.90	17.84	1.145
	(65,240,80)	1.40×10^2	68.19	17.67	1.145

Table 4.1: Resolution test for the compressible case at $Ra = 2.2Ra_c$, $Co = 1.5$ and $Co = 5$, for the case A. The resolution is given by (n_r, n_j, ℓ_{max}) where n_r is the number of radial grid points, n_j is the number of grid points in θ and ℓ_{max} is the maximum harmonic degree ℓ.

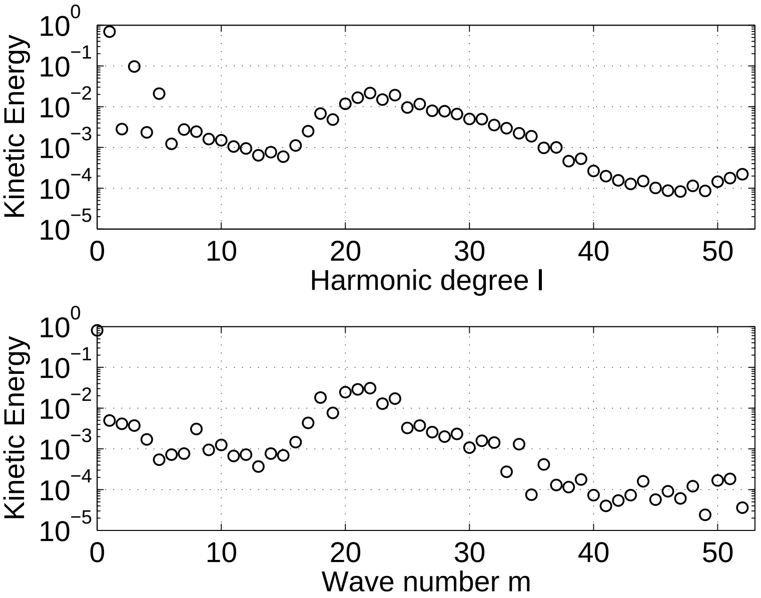

Fig. 4.1: Time-averaged spectrum of kinetic energy density at $Ra = 2.2Ra_c$, $Co = 5$ for the case A with resolution given by $(n_r, n_j, \ell_{max}) = (49, 160, 53)$. The spectrum is normalised with the total energy.

scale of the convection requires very high truncations, the criterion was somewhat relaxed to save computing time.

4.2.3 Numerical simulations

The time-averaged properties of the numerical solutions are listed at the end of the chapter in table 4.2 for the incompressible case, and in tables 4.3 and 4.4 for the compressible cases A and BI respectively. The radius ratio is $\eta = 0.35$ as explained in §2.3 and the Ekman number is $E = 3 \times 10^{-4}$. The Prandtl number is $Pr = 1$ for the Boussinesq case and case A, and in the case BI it is fixed to $Pr_i = 1$ at the inner boundary and decreases with radius.

4.3 Flow structure in compressible convection

4.3.1 Weak compressibility

The comparison between the incompressible and compressible cases is difficult for the models where the dimensionless numbers change with radius since it is hard to decide whether a certain feature is consequence of locally different parameters or other compressible effects. However, the compressible case A, where $\hat{\nu}$ and $\hat{\kappa}$ are constant is an exception since the dimensionless numbers remain also constant.

Time series of kinetic energy density and Nusselt number are plotted for $Co = 0$ and $Co = 1.5$ at $Ra = 2.2Ra_c$, $2.8Ra_c$ and $4Ra_c$ in figure 4.2. They show remarkable differences between incompressible and compressible cases. The bifurcation scenario is shortened in the Ra space where the solution becomes chaotic, and ultimately, intermittent in time at much lower Ra than the Boussinesq case. While at $Ra = 1.5Ra_c$ the solution is still drifting, chaotic behaviour is already present at $Ra = 2.2Ra_c$ for $Co = 1.5$. Vacillating convection was not observed, although it may exist in a very small region of the Ra space. At $Ra = 2.8Ra_c$, an additional slow variation is present that dominates time variation at $Ra = 4Ra_c$. In the Boussinesq case, on the other hand, solutions drift at $Ra = 2.2Ra_c$ but vacillate with a well defined frequency at $Ra = 2.8Ra_c$ and $Ra = 4Ra_c$. The slow variation can be found at larger Ra (Grote and Busse, 2001; Christensen, 2001; Christensen, 2002) and corresponds to the intermittent behaviour identified by Grote et al. (2001) and Christensen (2001).

Convection intermittent in time is characterised by a periodic exchange of energy between the convection columns and the zonal flow (Grote and Busse, 2001; Christensen, 2001). The vigour of the convection changes between periods of quiescence interrupted by short and intense bursts. When the convective flow is insignificant, the zonal flow decays since there are no Reynolds stresses to sustain it. When it has become very weak, convection columns grow in amplitude very quickly replenishing the energy in the zonal flow and the cycle repeats. At $Co = 1.5$, this type of behaviour is observed at $Ra = 4Ra_c$ (see figure 4.2), with peaks in E_{pol} and Nu where $E_{tor}^{m=0}$ is lowest.

The figure 4.3 shows time variation of equatorial z-vorticity for $Co = 0$ and $Co = 1.5$ at $Ra = 2.8Ra_c$ and $Ra = 4Ra_c$. The regularly spaced pattern in the Boussinesq cases, dominated by one or two wave numbers, is opposed by a much more complex pattern in the compressible cases, where more small-scale structures are present. Convection, close to the inner boundary at onset, tries to invade the shell at larger Ra at intermittent times, which becomes very concentrated in localised regions at $Ra = 4Ra_c$. Large regions don't take part in the radial convective flow even when the convection bursts take place. In the Boussinesq case, motionless regions (except for the zonal flow) were observed by Grote et al. (2001) at larger Ra. However, when the intermittent behaviour dominated, they were no longer present. In the compressible case, they although persist.

Selected meridional slices are shown in figure 4.4 for the azimuthal convective flow, given by $u_\varphi - \langle u_\varphi \rangle_\varphi$[1]. The degree of ageostrophy is remarkably higher in the compressible case, characterised by concentrated flow close to the outer boundary. Looking at the flow in the equatorial plane can now be misleading. Even when the flow

---

[1] $\langle u_\varphi \rangle_\varphi$: azimuthal average of u_φ.

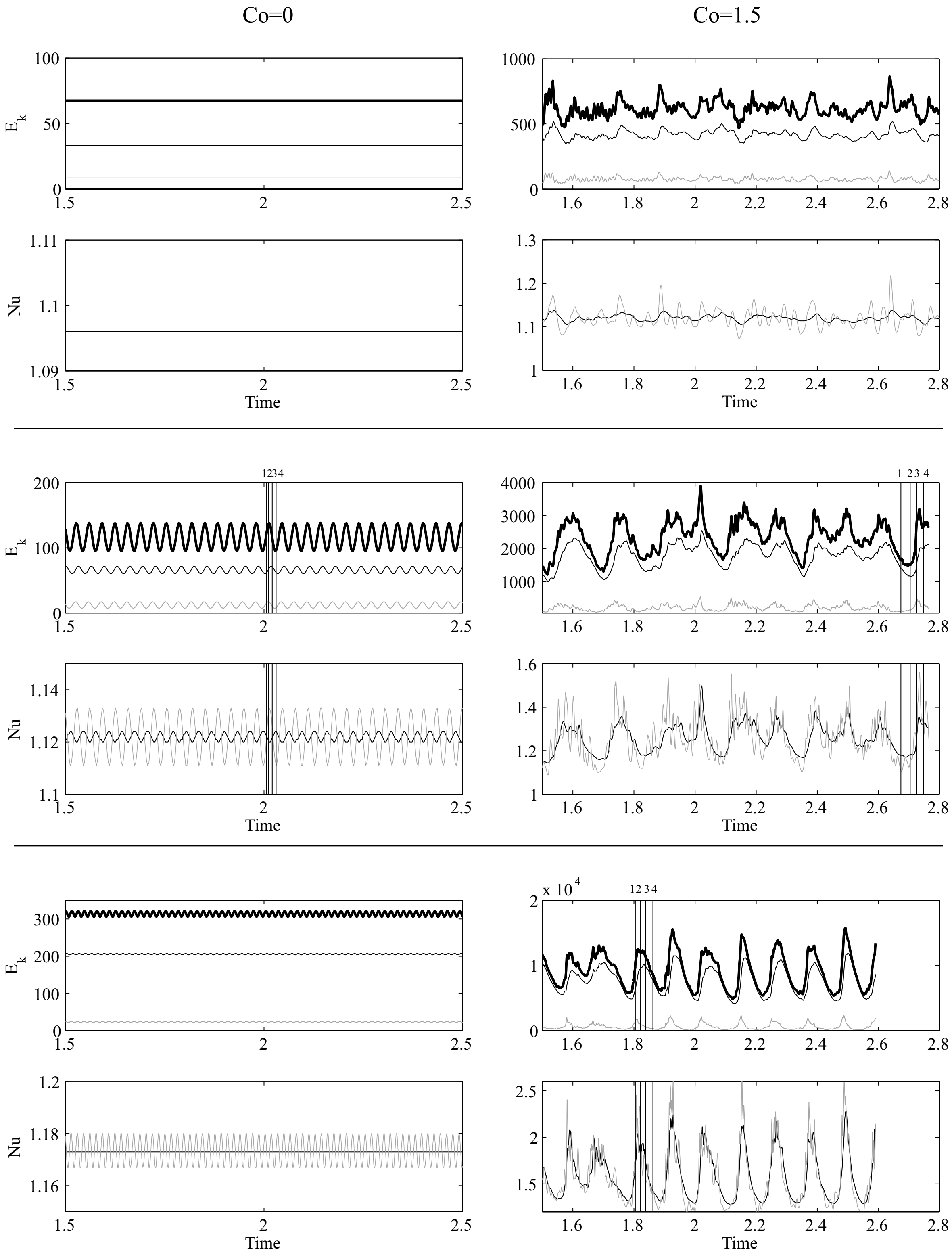

Co=0

Co=1.5

Fig. 4.2: Time series of kinetic energy density and Nusselt number for $Co = 0$ (left) and $Co = 1.5$ for the case A (right), at $Ra = 2.2Ra_c$, $2.8Ra_c$ and $4Ra_c$ from top to bottom. Plots above in each panel: the thick black line corresponds to E_k, the thin black line to $E_{tor}^{m=0}$, and the gray thin line to E_{pol}. Plots below in each panel: the thin black line is Nu_o and the thin gray line Nu_i.

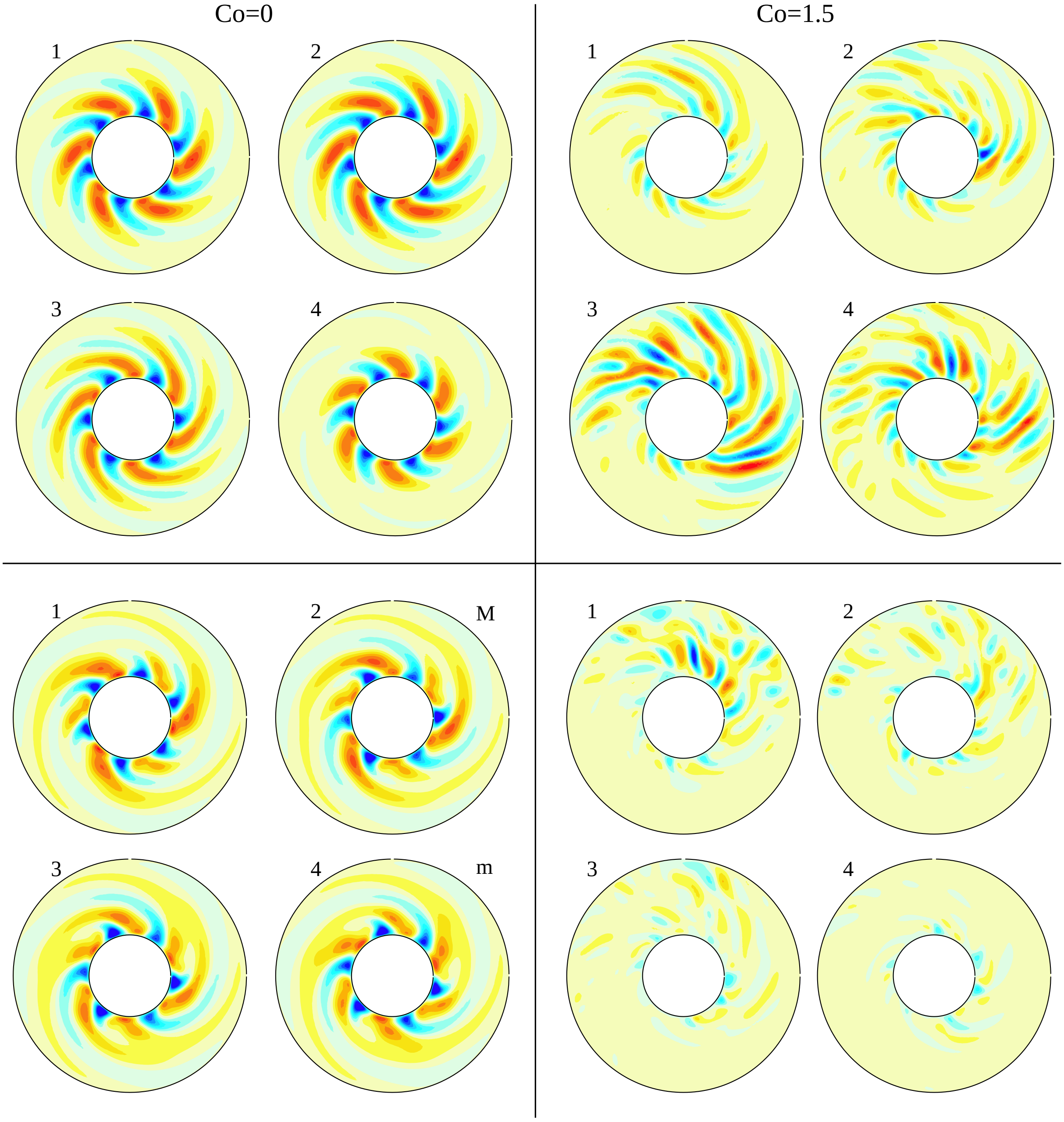

Fig. 4.3: Equatorial z-vorticity at $Ra = 2.8Ra_c$ (top) and $Ra = 4Ra_c$ (bottom) for the Boussinesq case (left) and the compressible case A with $Co = 1.5$ (right). M (m): maximum (minimum) E_{pol}. Red: positive, blue: negative. Contour step: $Co = 0$: ~ 72 at $Ra = 2.8Ra_c$, ~ 108 at $Ra = 4Ra_c$; $Co = 1.5$: ~ 290 at $Ra = 2.8Ra_c$, ~ 1080 at $Ra = 4Ra_c$.

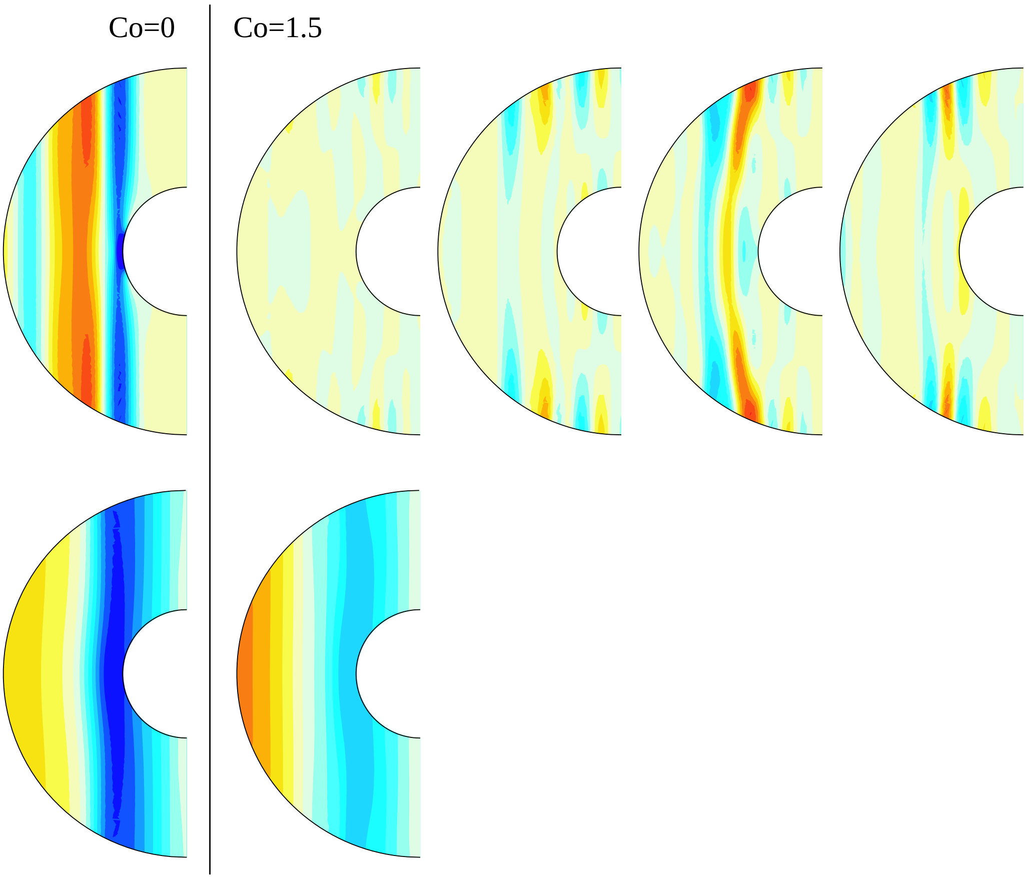

Fig. 4.4: Meridional slices of azimuthal convective velocity $u_\varphi - \langle u_\varphi \rangle_\varphi$ (above), and zonal flow $\langle u_\varphi \rangle_\varphi$ (below) for $Co = 0$ and $Co = 1.5$ at $Ra = 4Ra_c$. The slices correspond to the equatorial cut 1 for $Co = 0$ and 4 for $Co = 1.5$ given in figure 4.3. Red: prograde, blue: retrograde. Contour step: ~ 3.2 for $Co = 0$; ~ 16 for $Co = 1.5$.

is weak in the equatorial plane (see figure 4.3) may be much stronger at higher latitudes (see figure 4.4).

The onset of convection inside the tangent cylinder begins at much lower Ra than the Boussinesq case. At $E = 3 \times 10^{-4}$, incompressible convection remains insignificant inside the tangent cylinder for Rayleigh numbers as large as $Ra = 10Ra_c$ (see also Grote et al., 2001). In the compressible case, polar convection is already present for $Ra = 4Ra_c$ (see figure 4.5).

4.3.2 Intermediate to strong compressibility

Here, we compare cases with $Co = 3$ and $Co = 5$ for the compressible model A. Convection sets in adjacent to the outer boundary in these cases, although in the non-linear regime convection may become more global.

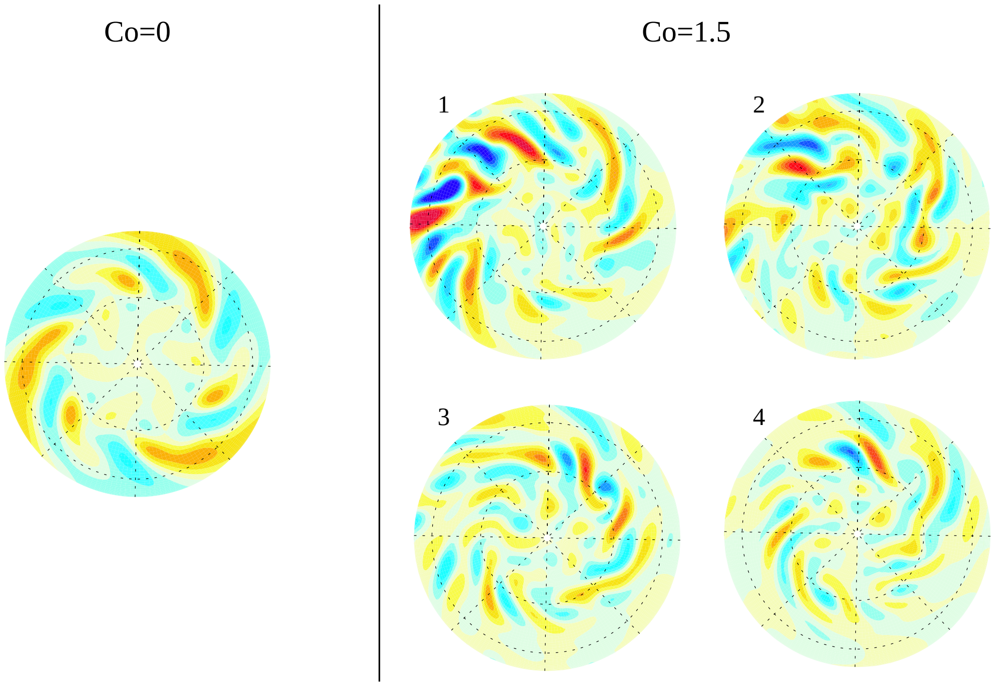

Fig. 4.5: North-polar views of radial velocity u_r at mid-depth at $Ra = 4Ra_c$ for $Co = 0$ and $Co = 1.5$ for the case A. Red: outwards, blue: inwards. Contour step: ~ 3.2 for $Co = 0$; ~ 16 for $Co = 1.5$.

Figure 4.6 shows time series of kinetic energy density and Nusselt number for these cases at $Ra = 2.2Ra_c$ and $Ra = 2.8Ra_c$. The intermittent type of convection is reached at even lower Rayleigh numbers for $Co = 3$ than for $Co = 1.5$. For $Co = 5$ the behaviour is chaotic at $Ra = 2.2Ra_c$, with some degree of intermittent behaviour at $Ra = 2.8Ra_c$ although not as clear as for $Co = 3$.

Time variation of equatorial z-vorticity is shown in figure 4.7. Convection becomes more small-scale with increasing compressibility although it is not much more space filling. The similarities between $Co = 3$ and $Co = 5$ at onset, governed by the convective instability at the outer boundary, have disappeared in the non-linear regime. For $Co = 3$, the patterns resemble somehow the ones at $Co = 1.5$, with convection filling only a fraction of the shell. Instead, at $Co = 5$ the flow is still concentrated adjacent to the outer boundary but has lost part of its azimuthal regularity. A characteristic azimuthal symmetry is still recognised with a wave number that has decreased from $m_c = 31$ at onset to ~ 20. The density and thermal conductivity is 148 times larger at the inner than at the outer boundary. The Rayleigh number, then is not high enough to achieve convection in the region where the thermal conductivity is very large.

Some selected meridional slices are shown in figure 4.8 for the azimuthal convective velocity. The degree of ageostrophy is also high for $Co = 3$ and $Co = 5$, with flow concentrated close to the outer boundary at higher latitudes. This can also be seen

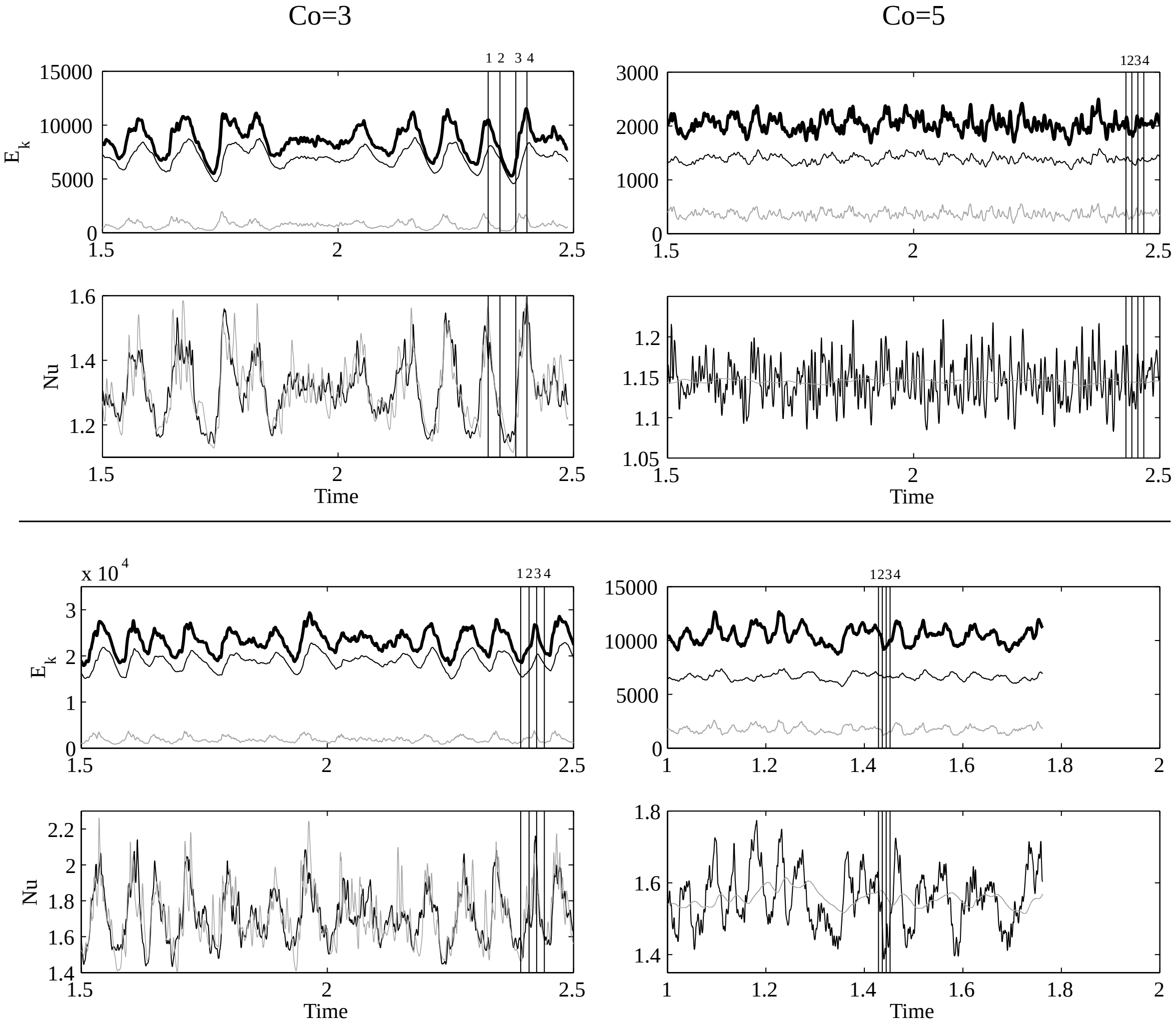

Fig. 4.6: Time series of kinetic energy density and Nusselt number plotted for the case A with $Co = 3$ (left) and $Co = 5$ (right), for $Ra = 2.2Ra_c$ (top) and $Ra = 2.8Ra_c$ (bottom). Plots above in each panel: the thick black line corresponds to E_k, the thin black line to $E_{tor}^{m=0}$, and the gray thin line to E_{pol}. Plots below in each panel: the thin black line is Nu_o and the thin gray line Nu_i.

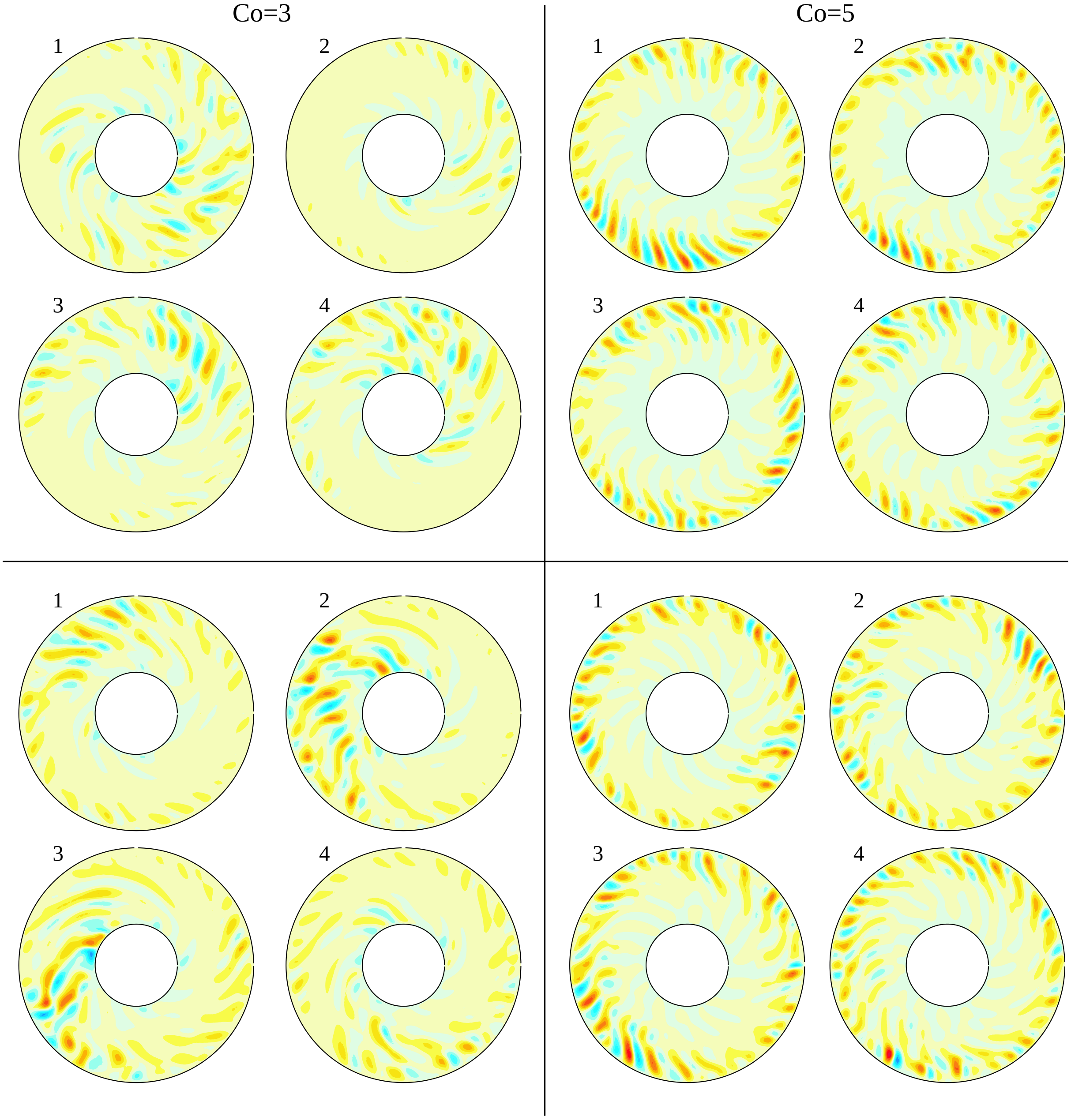

Fig. 4.7: Equatorial z-vorticity at $Ra = 2.2Ra_c$ (top) and $Ra = 2.8Ra_c$ (bottom) for the case A with $Co = 3$ (left) and $Co = 5$ (right). Red: positive, blue: negative. Contour step: $Co = 3$: ~ 950; $Co = 5$: ~ 610 at $Ra = 2.2Ra_c$, ~ 830 at $Ra = 2.8Ra_c$.

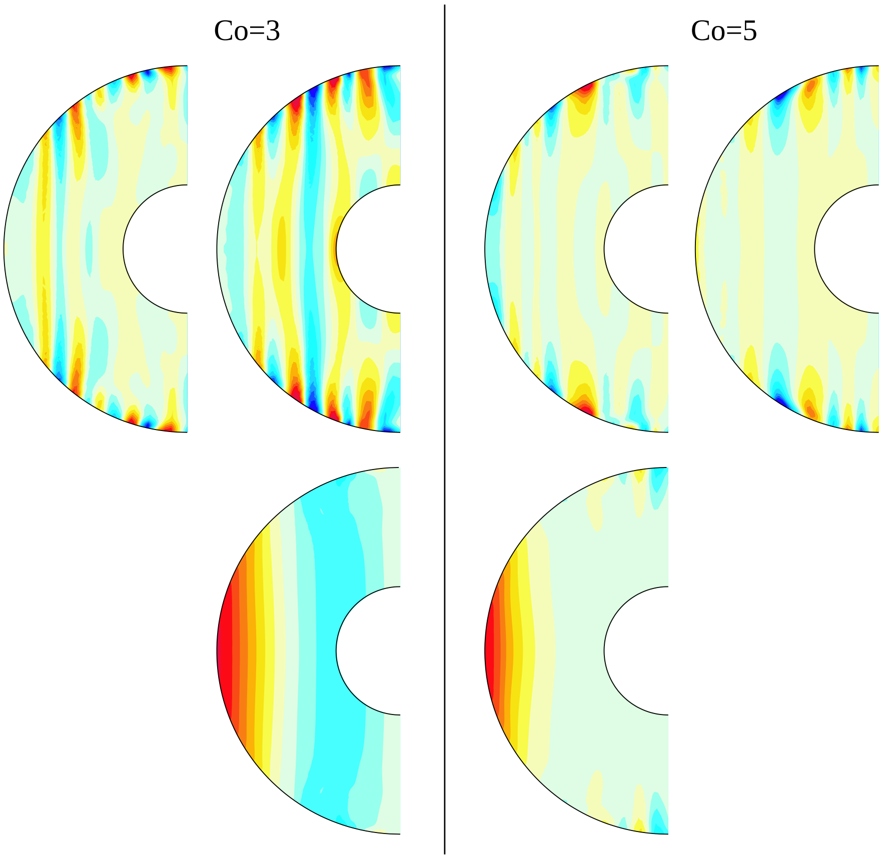

Fig. 4.8: Meridional slices of azimuthal convective velocity $u_\varphi - \langle u_\varphi \rangle_\varphi$ (above), and zonal flow $\langle u_\varphi \rangle_\varphi$ (below) for $Co = 3$ and $Co = 5$ at $Ra = 2.8Ra_c$. The slices correspond to the equatorial cuts labelled as 1 in figure 4.7. Red: prograde, blue: retrograde. Contour step: ~ 37.

in the north-polar views where the strength of the convection inside the tangent cylinder is larger at a quarter-depth than at mid-depth (see figure 4.9).

4.4 Effects of depth dependent thermal diffusivity

Depth dependent thermal diffusivity with constant kinematic viscosity gives a model where the local Prandtl and Rayleigh numbers change with depth. The interpretation is difficult since the effects of depth dependent dimensionless numbers cannot be separated from other compressibility effects. In particular, the model BI was explored, where some novel features were found.

Time series of kinetic energy density and Nusselt number are shown in figure 4.10 for $Ra = 2.2Ra_c$ and $Ra = 4Ra_c$, at $Co = 1.5$ and $Co = 3$. While chaotic behaviour dominated the case A at $Ra = 2.2Ra_c$ (see figures 4.2 and 4.6), the convection

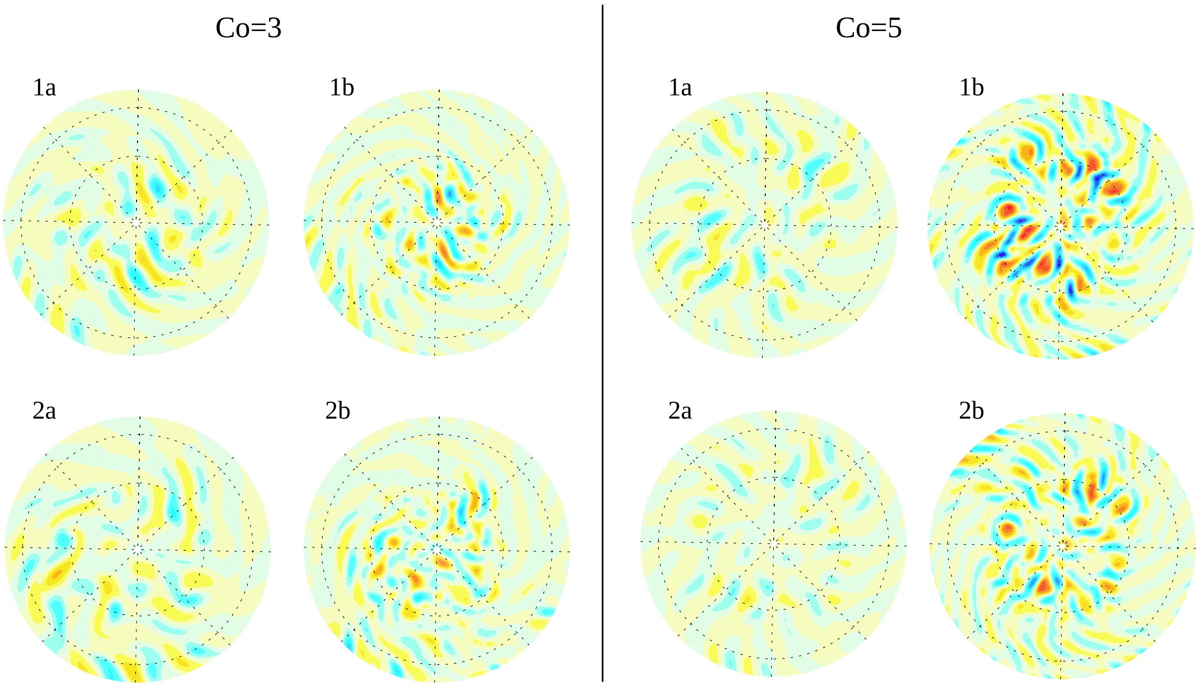

Fig. 4.9: North-polar views of radial velocity u_r at mid-depth (a) and a quarter-depth (b) at $Ra = 2.8Ra_c$ for the case A at $Co = 3$ (left) and $Co = 5$ (right). Red: outwards, blue: inwards. Contour step: ~ 37 for $Co = 3$; ~ 27 for $Co = 5$.

pattern is vacillating at $Co = 1.5$ and drifting at $Co = 3$ for the case BI. At $Ra = 4Ra_c$ the pattern is already chaotic, while for the model A the time behaviour is intermittent at $Co = 1.5$ (figure 4.2). The bifurcation scenario is not as shortened in the Ra space as it is in the model A. A convincing reason for this is not easy to identify since the two models cannot be directly compared.

Time sequences of equatorial z-vorticity are shown in figure 4.11 at $Ra = 2.2Ra_c$ and $Ra = 4Ra_c$, for $Co = 1.5$ and $Co = 3$. At $Ra = 4Ra_c$ a still visible spatial regularity is observed for both compressibilities despite the chaotic time behaviour. In particular, for $Co = 3$, the convection is more global with flow organised in apparently two layers. Meridional slices of azimuthal convective velocity in figure 4.12 seem to agree with this view. The inner layer is more time-dependent than the outer one and a relative drift is not evident in this time sequence.

If the compressibility is further increased to $Co = 5$ the separation in two different layers is even more pronounced, as figure 4.13 clearly demonstrates at $Ra = 2.2Ra_c$. Close to onset, convection can only be found close to the inner boundary (see figure 2.8). At $Ra = 2.2Ra_c$ the inner convective layer persists but an additional layer has formed close to the outer boundary. This outer convective layer forms at a much lower effective Prandtl number than the inner layer. At $Co = 5$, Pr varies from $Pr = 1$ at the inner to $Pr = 6.76 \times 10^{-3}$ at the outer boundary. It thus seems

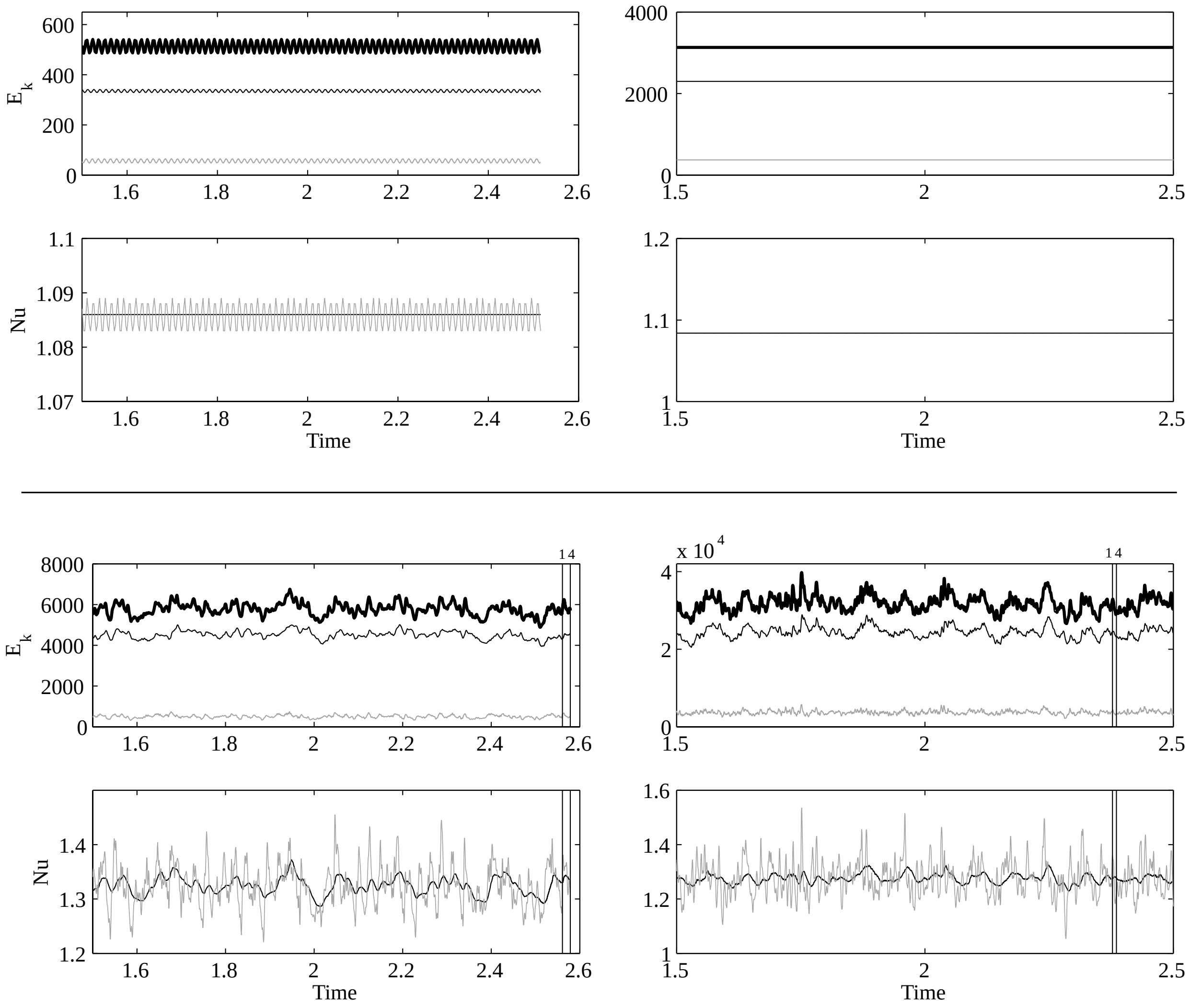

Fig. 4.10: Time series of kinetic energy density and Nusselt number plotted for the case BI with $Co = 1.5$ (left) and $Co = 3$ (right), for $Ra = 2.2Ra_c$ (top) and $Ra = 4Ra_c$ (bottom). Plots above in each panel: the thick black line corresponds to E_k, the thin black line to $E_{tor}^{m=0}$, and the gray thin line to E_{pol}. Plots below in each panel: the thin black line is Nu_o and the thin gray line Nu_i.

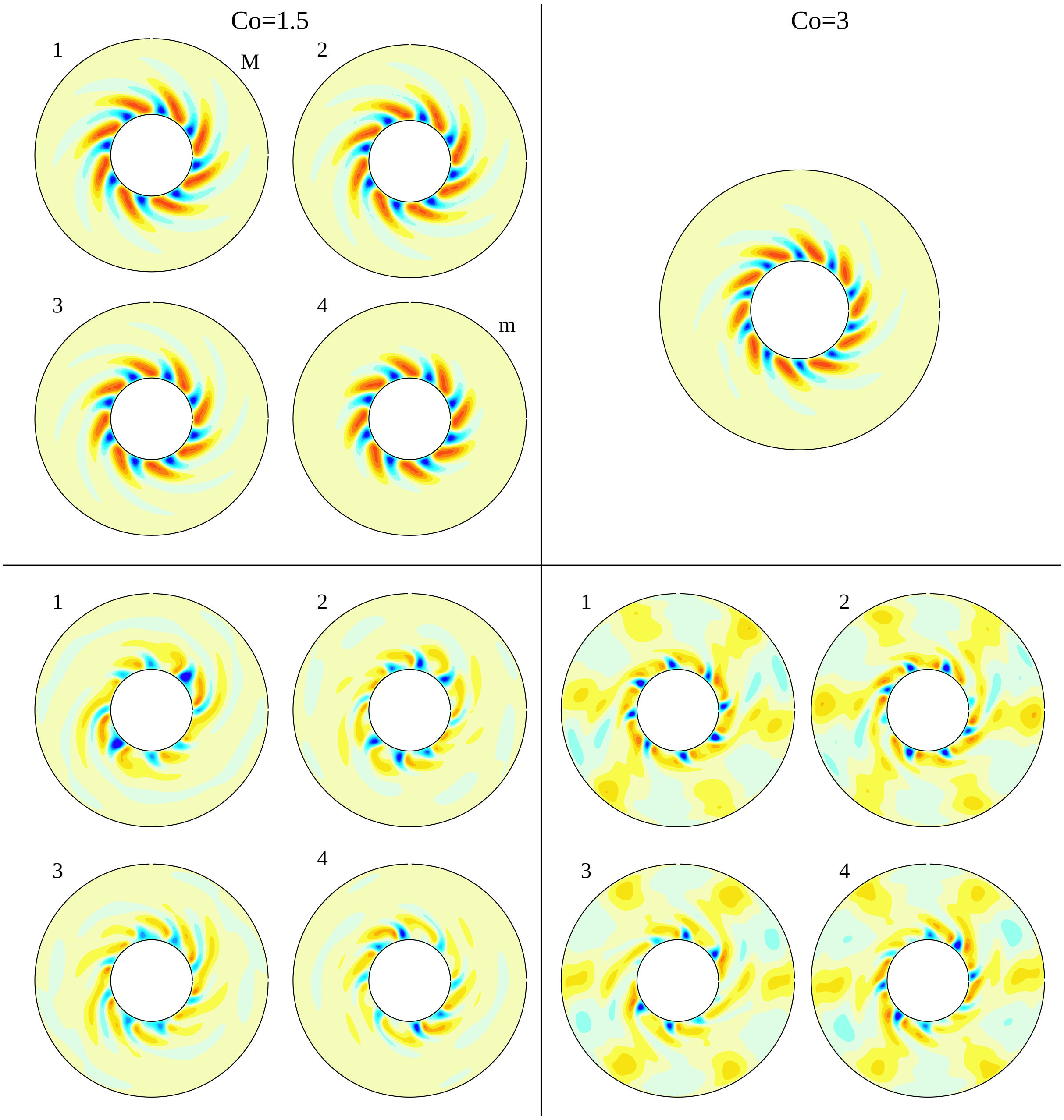

Fig. 4.11: Equatorial z-vorticity at $Ra = 2.2Ra_c$ (top) and $Ra = 4Ra_c$ (bottom) for the case BI with $Co = 1.5$ (left) and $Co = 3$ (right). Red: positive, blue: negative. Contour step: $Co = 1.5$: ~ 140 at $2.2Ra_c$, ~ 550 at $4Ra_c$; $Co = 3$: ~ 260 at $Ra = 2.2Ra_c$, ~ 740 at $Ra = 4Ra_c$.

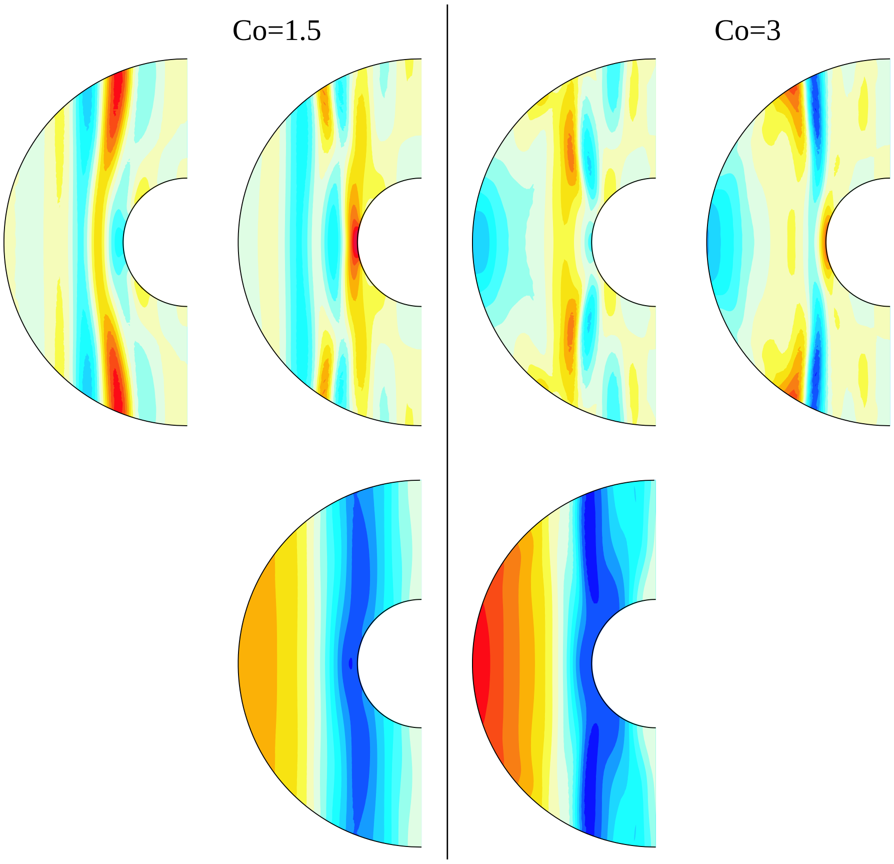

Fig. 4.12: Meridional slices of azimuthal convective velocity $u_\varphi - \langle u_\varphi \rangle_\varphi$ (above), and zonal flow $\langle u_\varphi \rangle_\varphi$ (below) for $Co = 1.5$ and $Co = 3$ at $Ra = 4Ra_c$. The slices correspond to the equatorial cuts labelled as 1 in figure 4.11. Red: prograde, blue: retrograde. Contour step: ~ 18 for $Co = 1.5$; ~ 23 for $Co = 3$.

likely that convection in the outer layer is a thermal inertial wave, typical for small Prandtl numbers (Zhang, 1994; Zhang, 1995).

Characteristic features of thermal inertial waves (Zhang, 1993; Zhang, 1994; Zhang, 1995) are given in §2.2.2 and can be summarised here in the following way:

- convective motions are trapped in the equatorial region, receiving thus the name of "wall-attached convection",
- they propagate faster than the convective modes, i.e. characteristic convective time scale is shorter than for the columnar convection,
- they are symmetric with respect the equatorial plane,
- the scale of the convection is large compared to the columns.

The outer convective layer is symmetric about the equatorial plane (see figure 4.16), and the scale of the convection is larger than in the inner columnar convective layer.

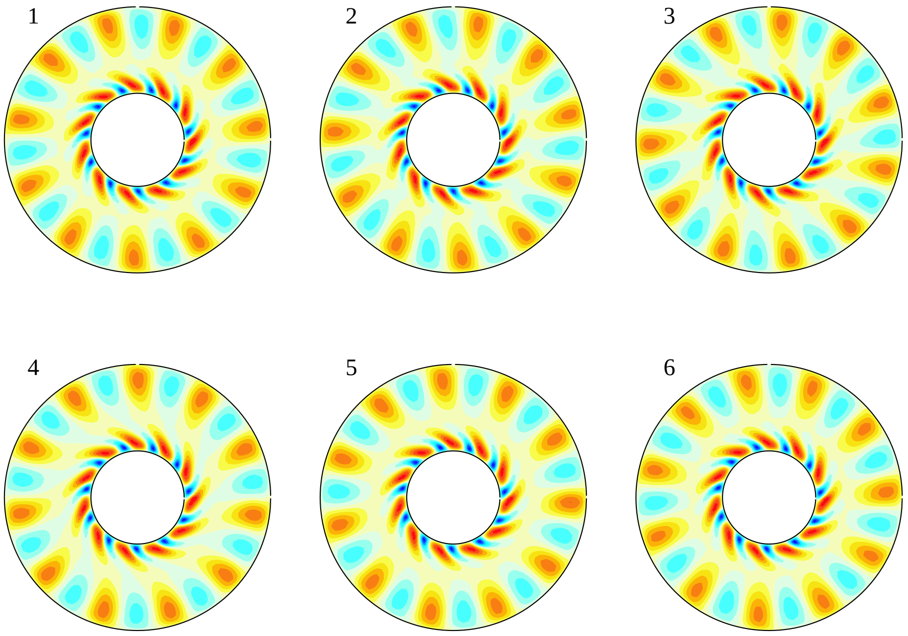

Fig. 4.13: Equatorial z-vorticity at $Ra = 2.2Ra_c$ for the case BI with $Co = 5$. Red: positive, blue: negative. Contour step: ~ 338.

Moreover, the corresponding wave number $m = 11$ is much lower than the values ~ 30 associated to columnar convection adjacent to the outer boundary, indicating also a larger scale of convection.

The faster propagation of the outer convective flow with respect to the inner columnar convection is clearly seen in figure 4.13. The outer pattern has propagated in the prograde direction such that the last plot is identical to the first one. There is in consequence a periodic behaviour in the whole pattern that results from the interaction between the two convective layers which manifests in small amplitude oscillations in the corresponding times series of kinetic energy density (figure 4.14). The characteristic time scale of the inner columnar convection can be estimated as $T_i = \frac{2\pi m}{\omega}$. Since the pattern drifts and the wave number m is the same as at onset, a first approach to ω is given by its critical value (table 2.4). For the outer convective layer, the characteristic time scale can be roughly estimated as $T_o \sim T \times m$, where T is the oscillation period in the time series. Thus, it results $T_i \sim 5\, T_o$.

Convection in the outer layer describes the features that characterise thermal inertial waves and in consequence it is very likely that this is the type of convection. The two different convective regimes, i.e. columnar convection and thermal inertial waves, can be present in the shell in the model BI because the local Prandtl number changes with radius, decreasing from 1 at the inner boundary to much smaller values at the outer boundary. For the model A, although convection adjacent to the outer boundary has been identified, no thermal inertial waves are possible since $Pr = 1$, constant throughout the shell.

At larger Rayleigh numbers, much of the regularly spaced pattern is lost for the wall-attached convection (see figure 4.15). Selected meridional slices of azimuthal convective velocity also show less organised convection compared to $Ra = 2.2Ra_c$ (see figure 4.16). In incompressible convection, the azimuthal symmetry of the thermal inertial waves is well preserved up to $Ra \sim 13Ra_c$ for $Pr = 0.025$ and $E = 1 \times 10^{-5}$ (Simitev and Busse, 2003). At even higher Ra, the pattern is more irregular with equatorially attached convection spreading into the interior and eventually detaching from the equator (Simitev and Busse, 2003). In the compressible case, there is not much resemblance to non-linear wall-attached convection as in Simitev and Busse (2003)'s studies. The time step required for this kind of simulations is very small and therefore, the time series given in figure 4.14 may be not long enough to reach the equilibrated state. Before concluding that the loss of symmetry is an effect of the compressibility, the corresponding time series have to be extended.
Convection inside the tangent cylinder (figures 4.17 and 4.18) is promoted at larger values of Ra with respect to the model A.

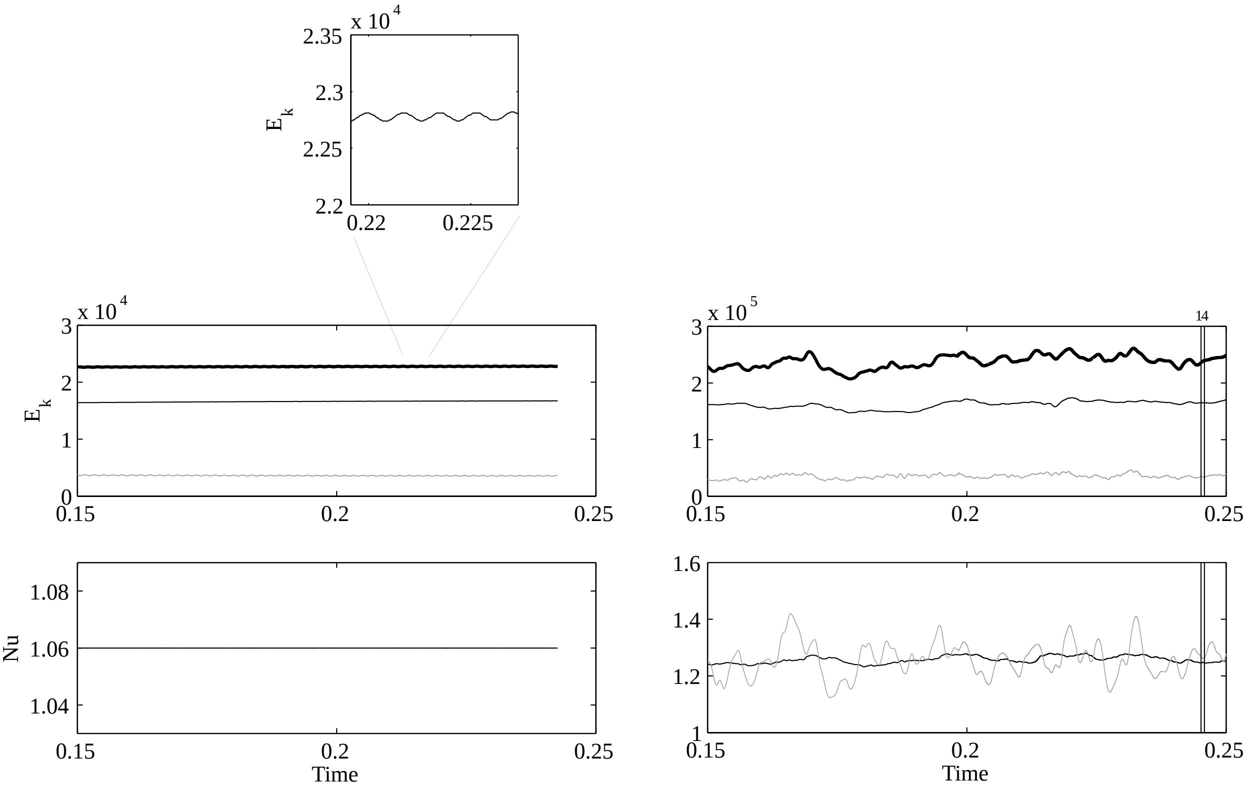

Fig. 4.14: Time series of kinetic energy density and Nusselt number plotted for the case BI for $Co = 5$ at $Ra = 2.2Ra_c$ (left) and $Ra = 4Ra_c$ (right). Upper plots: the thick black line corresponds to E_k, the thin black line to $E_{tor}^{m=0}$, and the gray thin line to E_{pol}. Lower plots: the thin black line is Nu_o and the thin gray line Nu_i.

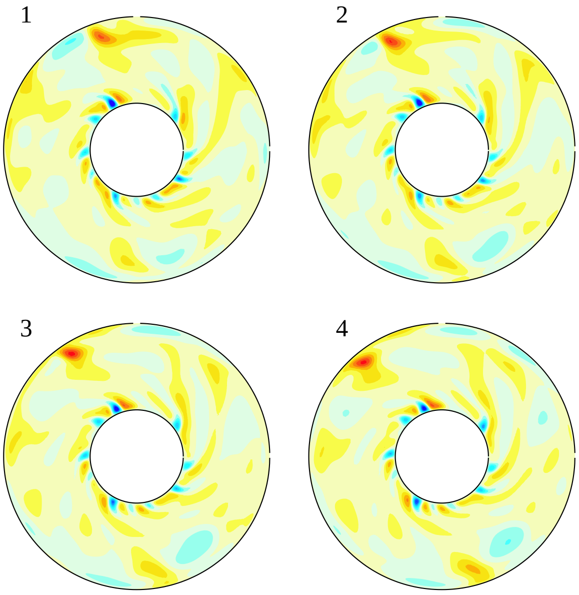

Fig. 4.15: Equatorial z-vorticity at $Ra = 4Ra_c$ for the case BI with $Co = 5$. Red: positive, blue: negative. Contour step: ~ 1430.

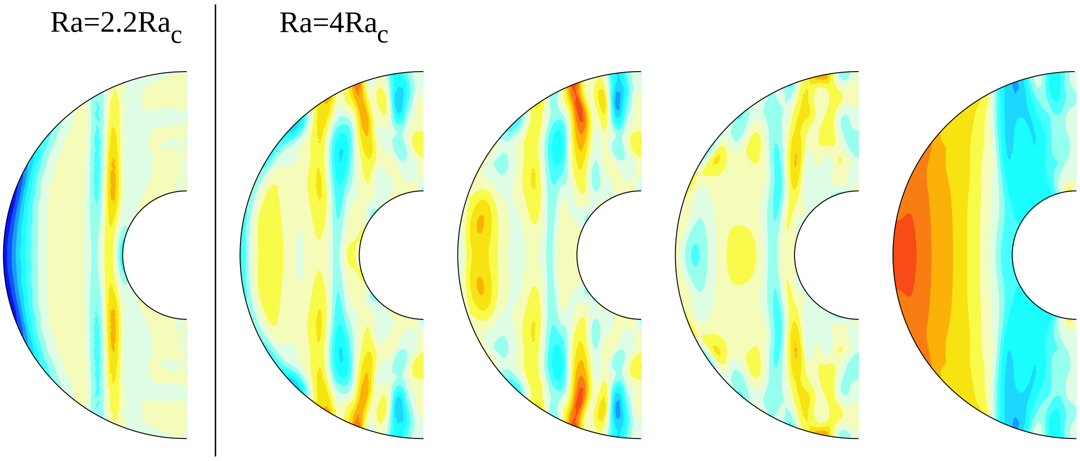

Fig. 4.16: Meridional slices of azimuthal convective velocity $u_\varphi - \langle u_\varphi \rangle_\varphi$ for the case BI for $Co = 5$ at $Ra = 2.2Ra_c$ and $Ra = 4Ra_c$. The zonal flow $\langle u_\varphi \rangle_\varphi$ at $Ra = 4Ra_c$ is plotted on the right. The slices correspond to the equatorial cuts labelled as 1 in figures 4.13 and 4.15. Contour steps: ~ 13 at $Ra = 2.2Ra_c$, ~ 57 at $Ra = 4Ra_c$.

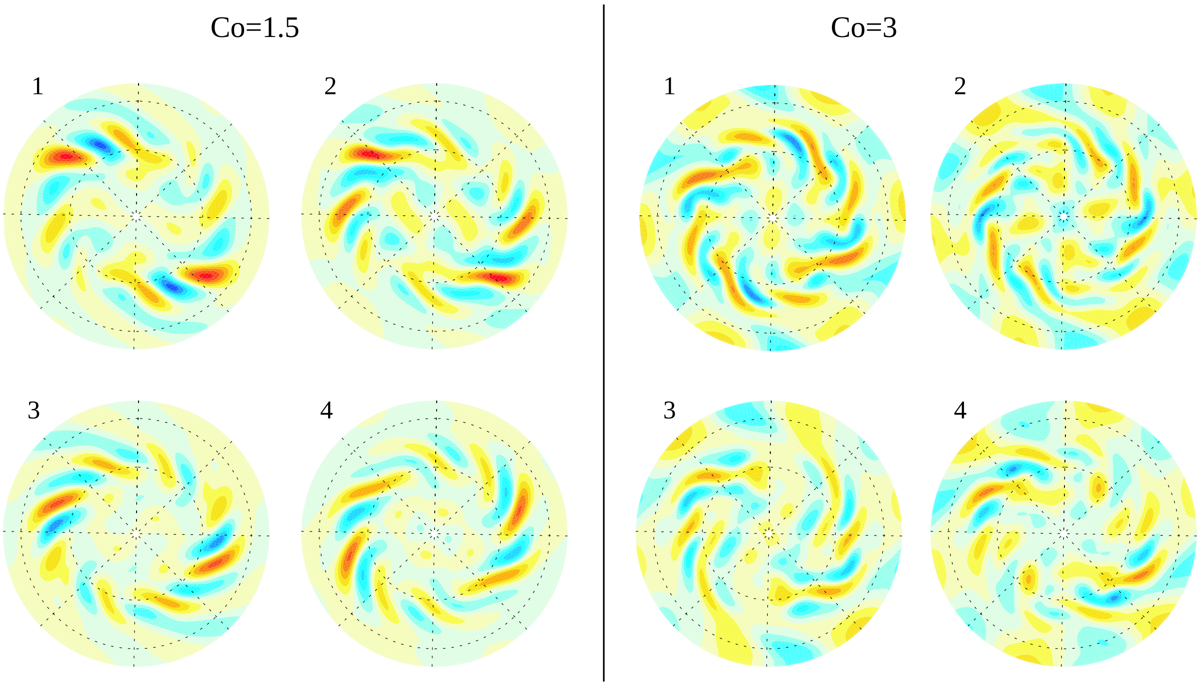

Fig. 4.17: North-polar views of radial velocity u_r at mid-depth at $Ra = 4Ra_c$ for the case BI at $Co = 1.5$ (left) and $Co = 3$ (right). Red: outwards, blue: inwards. Contour step: ~ 18 for $Co = 1.5$; ~ 23 for $Co = 3$.

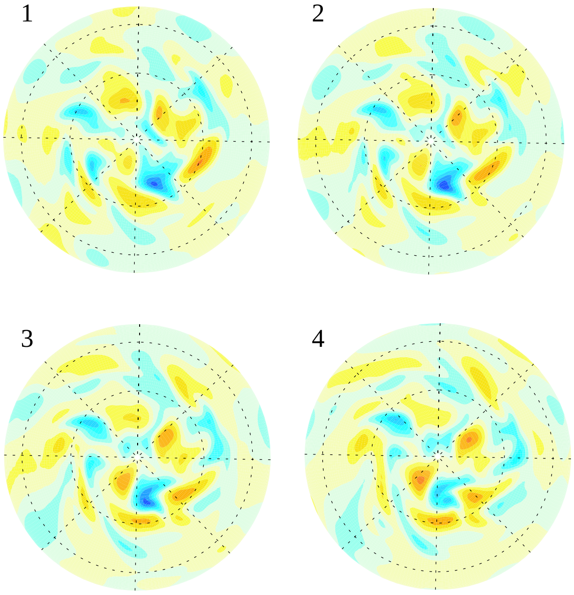

Fig. 4.18: North-polar views of radial velocity u_r at mid-depth for the case BI at $Co = 5$ and $Ra = 4Ra_c$. Red: outwards, blue: inwards. Contour step: ~ 57.

4.5 Global properties of compressible convection

4.5.1 Constant dimensionless numbers, case A

Time-averaged global properties for the compressible model A (table 4.3) were plotted vs. Ra/Ra_c and Co together with the properties for the Boussinesq cases (table 4.2).

Figure 4.19 shows $E_{tor}^{m=0}/E_k$ and E_{pol}/E_k plotted vs. Ra/Ra_c. The gradual increase of energy in the zonal flow up to moderate Rayleigh numbers is a known feature in the incompressible convection (see e.g. Christensen, 2001; Christensen, 2002). The non-linear term $(\boldsymbol{u} \cdot \boldsymbol{\nabla})\boldsymbol{u}$ in the Navier-Stokes equation generates Reynolds stresses (see e.g. Tritton, 1988) due to the correlation between u_φ and u_s that results from the curvature of the outer boundary (Busse, 1983; Busse, 1994). Thus, this mechanism transfers kinetic energy from the small-scale convective flow into the large-scale zonal flow.

For the compressible cases, the same behaviour at $Co = 0$ is observed at $Co = 1.5$ and $Co = 3$, with energies in the zonal flow that increased in some cases by more than 20% with respect to the Boussinesq cases. At $Co = 5$ the zonal energy is larger than at $Co = 0$ although it is smaller than at $Co = 3$. This may be connected with the fact that in the non-linear regime up to $Ra = 2.8Ra_c$ convection is not global being still concentrated closer to the outer boundary (see figure 4.7). There is an initial increase of zonal flow energy followed by a decrease at $Ra = 2.8Ra_c$. This trend has to be confirmed with simulations at larger Ra.

Reynolds stresses may also be responsible for the energy input in the zonal flow when the ambient density is not constant. It is however not clear why the energy in the zonal flow increases with compressibility (up to $Co = 3$) despite the loss of geostrophy of the convective flow (see figures 4.4 and 4.12). For $Co = 5$, Reynolds stresses may have lost part of the efficiency to generate zonal flow since convection is still very much localised close to the outer boundary. A detailed study of Reynolds stresses is required to analyse the role of radially varying ambient density.

Figure 4.20 shows $E_{tor}^{m=0}/E_k$ and E_{pol}/E_k plotted vs. Co. At $Ra = 1.1Ra_c$ the energy in the zonal flow does not exceed 20%. At larger Ra, it has increased to more than 50% and the increase of $E_{tor}^{m=0}/E_k$ with Co is evident up to $Co = 3$. At $Co = 5$ the zonal energies have decreased with respect to $Co = 1.5$ and $Co = 3$.

The effect of compressibility in the zonal flow can also be seen in figures 4.4 and 4.8, where $\langle u_\varphi \rangle_\varphi$ was plotted at $Ra = 4Ra_c$ and $Ra = 2.8Ra_c$ respectively. Increasing Co, the strength of the retrograde zonal flow decreases with respect to the prograde flow. Geostrophy is preserved, and at $Co = 5$ only a equatorial prograde flow is present.

Time averaged Nu plotted vs. Ra/Ra_c is shown in 4.21. The sudden change in slope

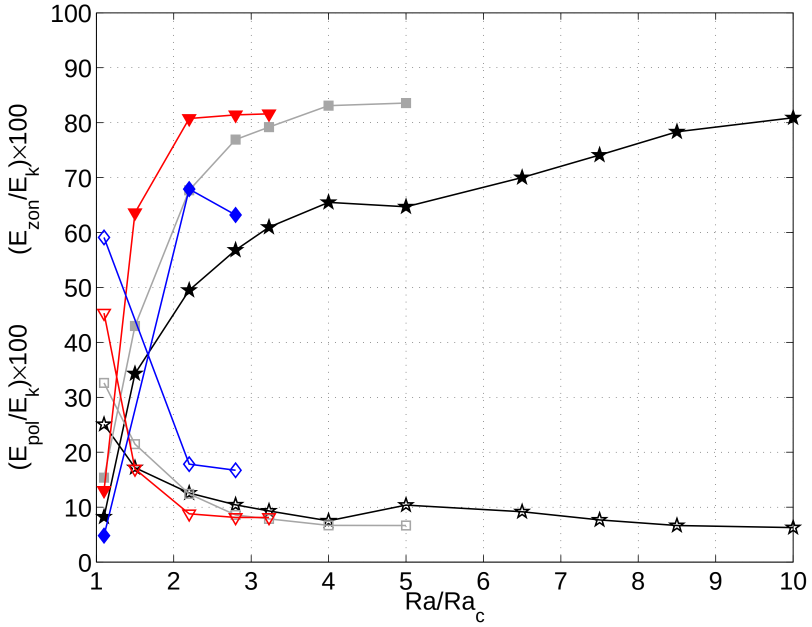

Fig. 4.19: Time-averaged % axisymmetric toroidal kinetic energy density $E_{tor}^{m=0}/E_k$ (filled symbols) and % poloidal kinetic energy density E_{pol}/E_k (open symbols) plotted vs. Ra/Ra_c for the case A. ($\star$): $Co = 0$; (gray $\Box$): $Co = 1.5$; (red $\triangledown$): $Co = 3$; (blue $\Diamond$): $Co = 5$.

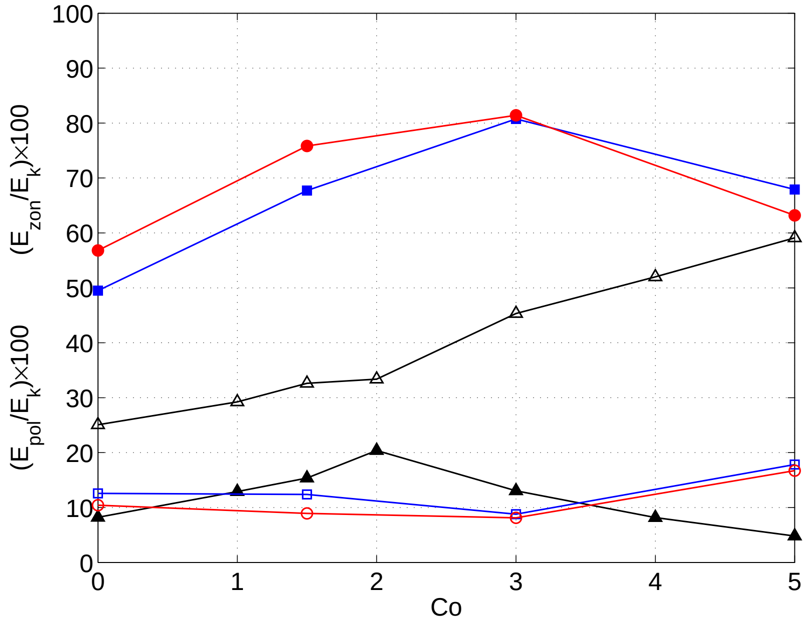

Fig. 4.20: Time-averaged % axisymmetric toroidal kinetic energy density $E_{tor}^{m=0}/E_k$ (filled symbols) and % poloidal kinetic energy density E_{pol}/E_k (open symbols) plotted vs. Co for the case A. (black $\triangle$): $Ra = 1.1Ra_c$; (blue $\Box$): $Ra = 2.2Ra_c$; (red $\circ$): $Ra = 2.8Ra_c$.

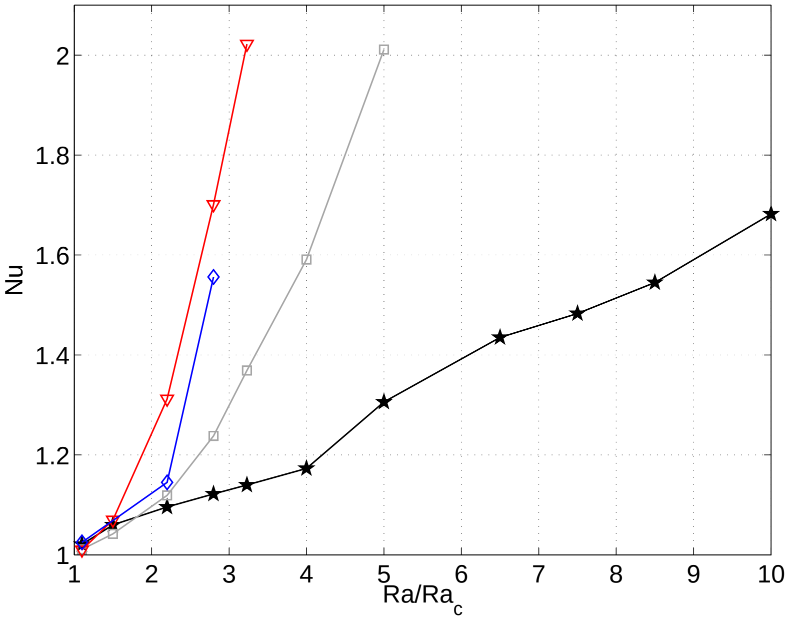

Fig. 4.21: Time-averaged Nusselt number Nu plotted vs. Ra/Ra_c for the case A. ($\star$): $Co = 0$; (gray $\Box$): $Co = 1.5$; (red $\bigtriangledown$): $Co = 3$; (blue $\Diamond$): $Co = 5$.

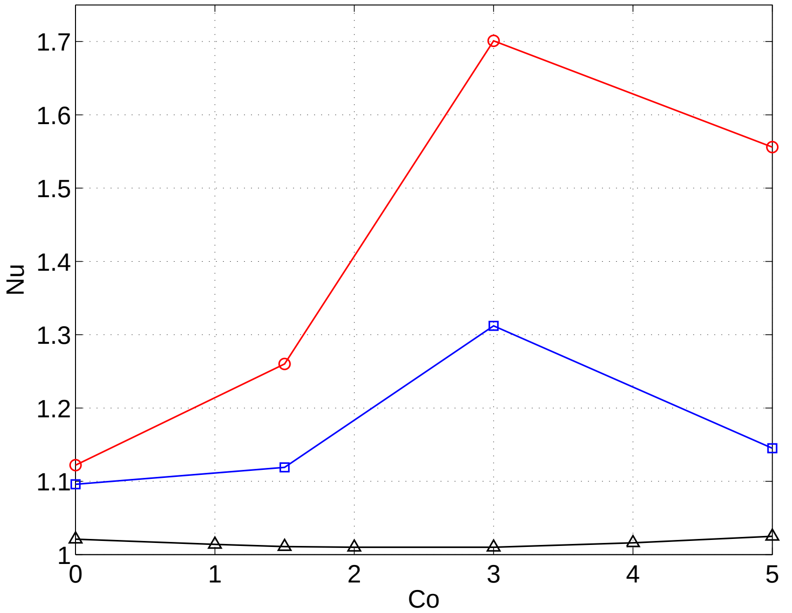

Fig. 4.22: Time-averaged Nusselt number Nu plotted vs. Co for the case A. (black $\bigtriangleup$): $Ra = 1.1Ra_c$; (blue $\Box$): $Ra = 2.2Ra_c$; (red $\circ$): $Ra = 2.8Ra_c$.

noticed in all the curves is connected with the onset of strong time dependence, already observed by Tilgner and Busse (1997) in the Boussinesq case. Chaotic convection becomes more efficient in transporting heat in the compressible case than in the incompressible case, reflected by the larger values of Nu. Figure 4.22 shows Nu as function of Co for different values of Ra. The increase of Nu with Co is observed up to $Co = 3$. At $Co = 5$ convection has become less efficient with respect to $Co = 3$.

Time averaged total kinetic energy E_k is plotted vs. Ra/Ra_c in figure 4.23, and vs. Co in figure 4.24. The values are larger in the compressible case, increasing with Co and Ra. In some cases, E_k is around two orders of magnitude larger than the corresponding incompressible counterpart. At $Co = 5$, E_k is lower than the values at $Co = 1.5$ and $Co = 3$. There is therefore a decrease in all the global properties at $Co = 5$ with respect to the values at $Co = 3$ or even $Co = 1.5$, which is likely connected to the localised convection close to the outer boundary up to $2.8Ra_c$. Simulations at larger Ra are required to see whether this behaviour of the global properties remains.

4.5.2 Depth dependent thermal diffusivity, case BI

In the same way as for the model A, time-averaged global properties were plotted for the model BI (table 4.4) vs. Ra/Ra_c and Co together with the properties for the Boussinesq cases (table 4.2).

Figures 4.25 and 4.26 show $E_{tor}^{m=0}/E_k$ and E_{pol}/E_k plotted vs. Ra/Ra_c and Co respectively. There are no significant qualitative differences compared to the curves for the case A despite the differences between the models. The zonal energy increases with Ra and with Co. A decrease in zonal energy with respect to $Co = 3$ is observed at $Co = 5$ for $Ra = 4Ra_c$. Like for the model A, to explore whether this trend persists, simulations at larger Ra are required for $Co = 5$. Figures 4.12 and 4.16 show zonal flow at $Ra = 4Rac$. The strength of the equatorial prograde flow increases with Co but on the contrary to the model A, the zonal flow stays more global.

The time-averaged Nusselt number Nu also shows a sudden change in slope when plotted vs. Ra/Ra_c in connection with the onset of chaotic time behaviour (see figure 4.27). There is as well as in model A, a loss of efficiency in transporting heat at $Co = 5$ as show the curves of Nu vs. Co in figure 4.28.

Figures 4.29 and 4.30 show total kinetic energy density E_k plotted vs. Ra/Ra_c and Co, respectively. Compared to the model A, the curves show a different behaviour: the decrease in energy from $Co = 3$ to $Co = 5$ in the model A is not observed here. Instead, E_k smoothly increases with Ra and Co. Apparently, the decrease of global properties at high compressibilities is therefore, a feature not always present.

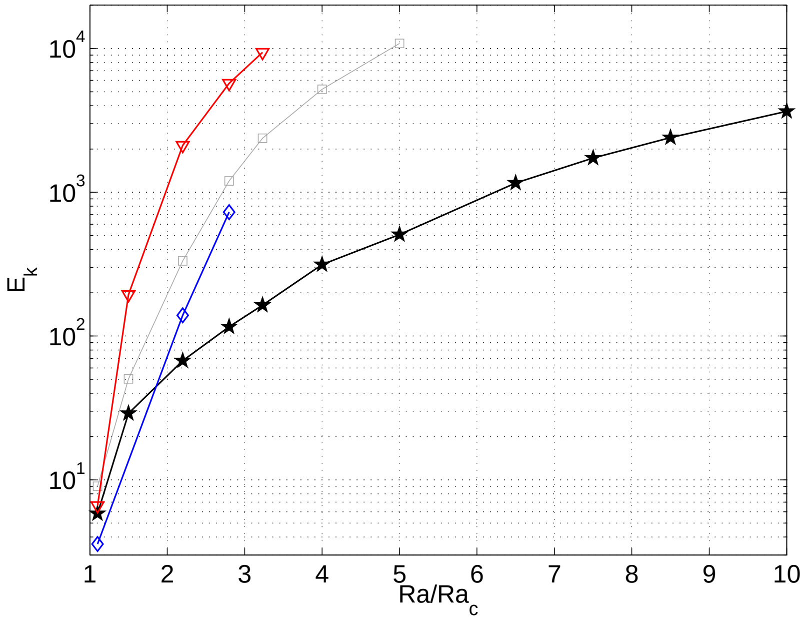

Fig. 4.23: Time-averaged kinetic energy density E_k plotted vs. Ra/Ra_c for the case A. ($\star$): $Co = 0$; (gray $\square$): $Co = 1.5$; (red $\triangledown$): $Co = 3$; (blue $\Diamond$): $Co = 5$.

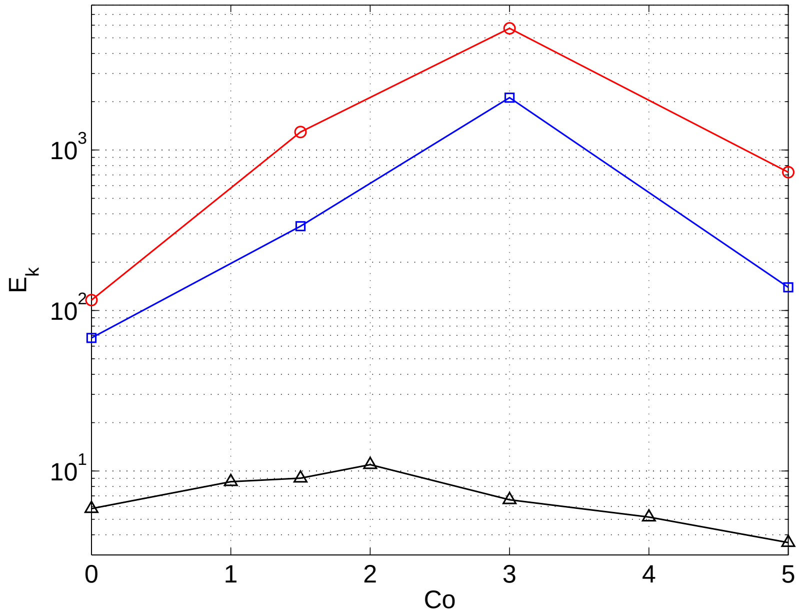

Fig. 4.24: Time-averaged kinetic energy density E_k plotted vs. Co for the case A. (black $\triangle$): $Ra = 1.1Ra_c$; (blue $\square$): $Ra = 2.2Ra_c$; (red $\circ$): $Ra = 2.8Ra_c$.

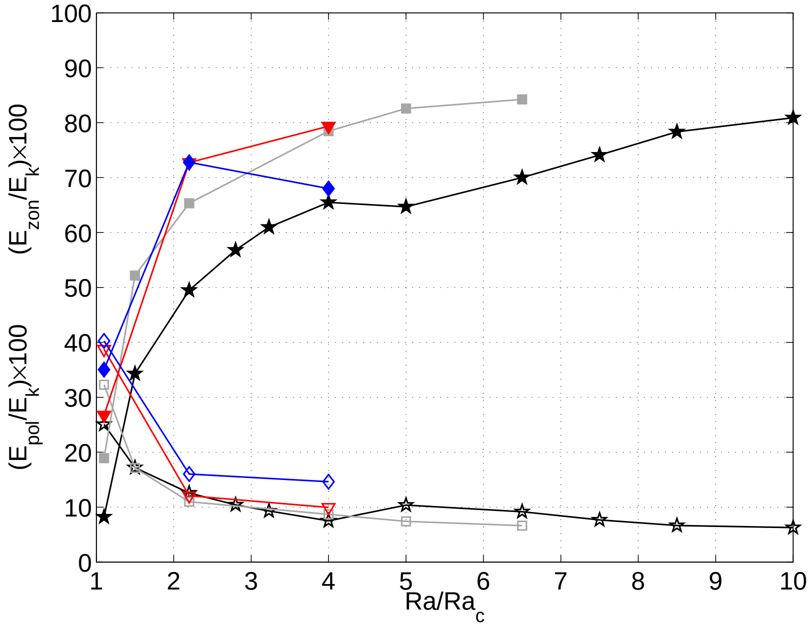

Fig. 4.25: Time-averaged % axisymmetric toroidal kinetic energy density $E_{tor}^{m=0}/E_k$ (filled symbols) and % poloidal kinetic energy density E_{pol}/E_k (open symbols) plotted vs. Ra/Ra_c for the case BI. ($\star$): $Co = 0$; (gray $\Box$): $Co = 1.5$; (red $\triangledown$): $Co = 3$; (blue $\Diamond$): $Co = 5$.

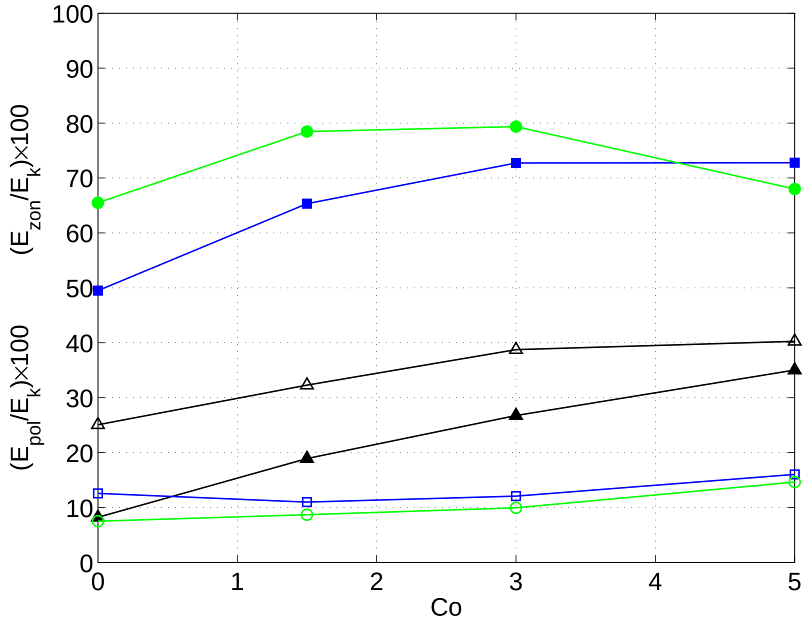

Fig. 4.26: Time-averaged % axisymmetric toroidal kinetic energy density $E_{tor}^{m=0}/E_k$ (filled symbols) and % poloidal kinetic energy density E_{pol}/E_k (open symbols) plotted vs. Co for the case BI. (black $\triangle$): $Ra = 1.1Ra_c$; (blue $\Box$): $Ra = 2.2Ra_c$; (green $\circ$): $Ra = 4Ra_c$.

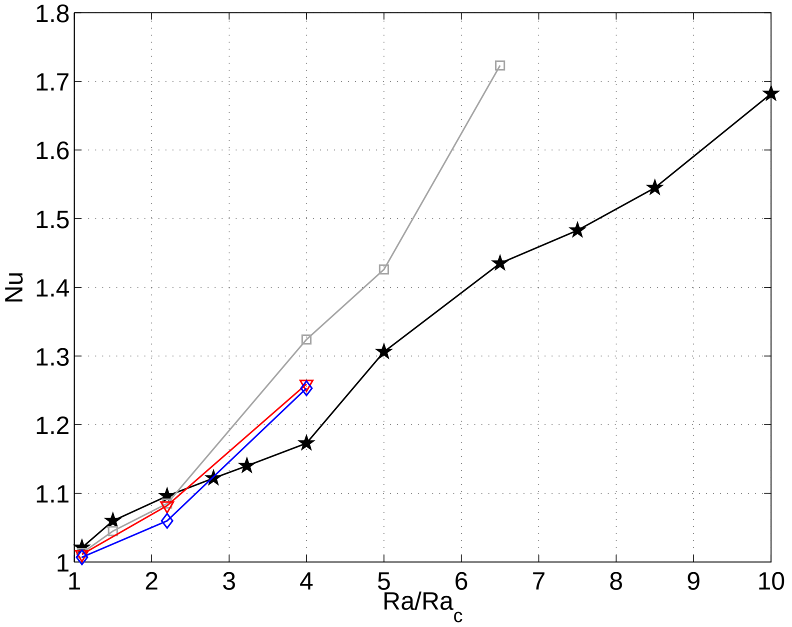

Fig. 4.27: Time-averaged Nusselt number Nu plotted vs. Ra/Ra_c for the case BI. ($\star$): $Co = 0$; (gray $\Box$): $Co = 1.5$; (red $\triangledown$): $Co = 3$; (blue $\Diamond$): $Co = 5$.

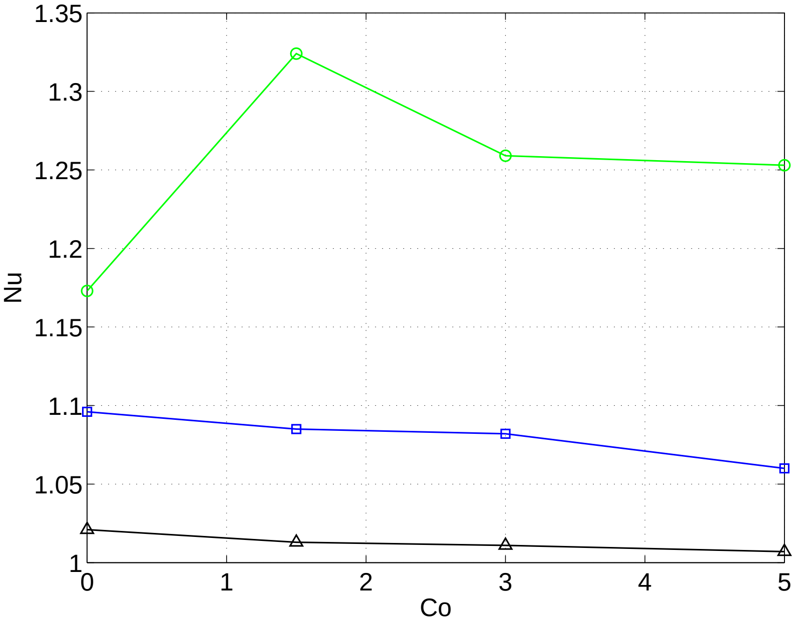

Fig. 4.28: Time-averaged Nusselt number Nu plotted vs. Co for the case BI. (black $\triangle$): $Ra = 1.1Ra_c$; (blue $\Box$): $Ra = 2.2Ra_c$; (green $\circ$): $Ra = 4Ra_c$.

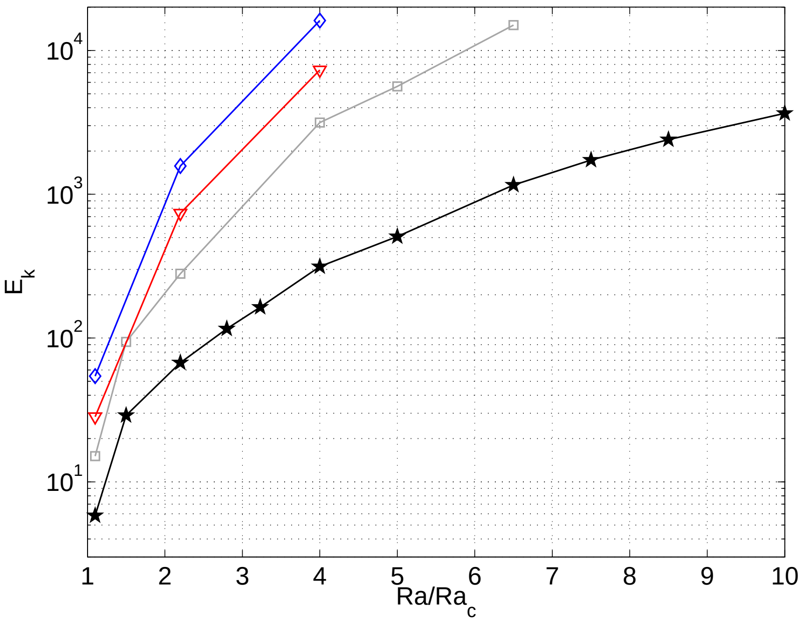

Fig. 4.29: Time-averaged kinetic energy density E_k plotted vs. Ra/Ra_c for the case BI. ($\star$): $Co = 0$; (gray □): $Co = 1.5$; (red ▽): $Co = 3$; (blue ◇): $Co = 5$.

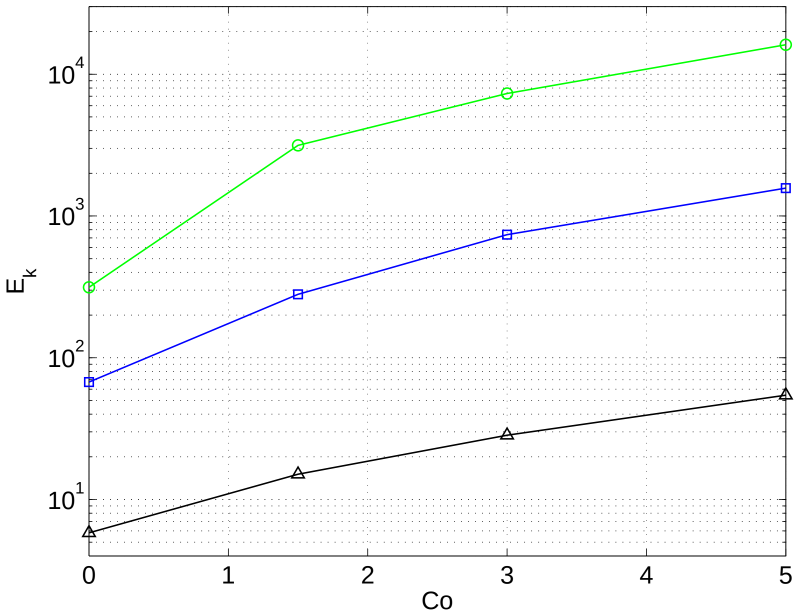

Fig. 4.30: Time-averaged kinetic energy density E_k plotted vs. Co for the case BI. (black △): $Ra = 1.1Ra_c$; (blue □): $Ra = 2.2Ra_c$; (green ○): $Ra = 4Ra_c$.

For the model A, this decrease was associated to the localised convection at the outer boundary. For the case BI, it could be instead a response to the presence of thermal inertial waves. Global properties of additional models have to be explored at high compressibilities and larger Rayleigh numbers to discern whether this is a characteristic feature of high compressibility.

4.6 Tables with results

The list of results presented in this chapter are given in table 4.2 for the Boussinesq case, table 4.3 for the compressible model A and table 4.4 for the compressible model BI. The Ekman number is $E = 3 \times 10^{-4}$ and the radius ratio is $\eta = 0.35$. The Prandtl number is $Pr = 1$ in the Boussinesq case and model A, and varies from $Pr_i = 1$ at the inner boundary to $Pr_o = 0.22$, $Pr_o = 0.05$ or $Pr_o = 6.76 \times 10^{-3}$ for $Co = 1.5$, $Co = 3$ and $Co = 5$ respectively.

Ra/Ra_c	E_k	$(E_{tor}^{m=0}/E_k) \times 100$	$(E_{pol}/E_k) \times 100$	Nu
1.10	5.82×10^0	8.22	25.07	1.021
1.50	2.90×10^1	34.31	17.19	1.060
2.20	6.74×10^1	49.50	12.58	1.096
2.80	1.16×10^2	56.81	10.43	1.122
3.23	1.64×10^2	60.97	9.31	1.140
4.00	3.14×10^2	65.48	7.52	1.173
5.00	5.08×10^2	64.68	10.38	1.306
6.50	1.16×10^3	70.01	9.16	1.435
7.50	1.73×10^3	74.09	7.67	1.483
8.50	2.40×10^3	78.33	6.66	1.545
10.0	3.66×10^3	80.89	6.28	1.682

Table 4.2: Time-averaged properties in the supercritical regime for the Boussinesq case at $Pr = 1$ and $E = 3 \times 10^{-4}$.

Co	Ra/Ra_c	E_k	$(E_{tor}^{m=0}/E_k) \times 100$	$(E_{pol}/E_k) \times 100$	Nu
1.0	1.10	8.57×10^0	12.90	29.23	1.014
1.5	1.10	9.02×10^0	15.37	32.62	1.011
	1.50	5.04×10^1	43.00	21.48	1.042
	2.20	3.35×10^2	67.72	12.39	1.119
	2.80	1.29×10^3	75.83	8.94	1.260
	3.23	2.38×10^3	79.20	7.86	1.369
	4.00	5.20×10^3	83.09	6.68	1.591
	5.00	1.08×10^4	83.56	6.67	2.011
2.0	1.10	1.09×10^1	20.39	33.38	1.010
3.0	1.10	6.61×10^0	13.06	45.32	1.010
	1.50	1.94×10^2	63.60	16.95	1.070
	2.20	2.12×10^3	80.75	8.80	1.312
	2.80	5.73×10^3	81.41	8.13	1.701
	3.23	9.40×10^3	81.60	8.12	2.022
4.0	1.10	5.16×10^0	8.17	52.01	1.016
5.0	1.10	3.58×10^0	4.81	59.11	1.025
	2.20	1.39×10^2	67.90	17.84	1.145
	2.80	7.28×10^2	63.20	16.72	1.556

Table 4.3: Time-averaged properties in the supercritical regime for the case A at $Pr = 1$ and $E = 3 \times 10^{-4}$.

Co	Ra/Ra_c	E_k	$(E_{tor}^{m=0}/E_k) \times 100$	$(E_{pol}/E_k) \times 100$	Nu
1.5	1.10	1.51×10^1	18.92	32.29	1.013
	1.50	9.40×10^1	52.17	17.15	1.045
	2.20	2.80×10^2	65.31	10.98	1.085
	4.00	3.15×10^3	78.45	8.69	1.324
	5.00	5.63×10^3	82.57	7.43	1.426
	6.50	1.50×10^4	84.22	6.64	1.723
3.0	1.10	2.84×10^1	26.76	38.76	1.011
	2.20	7.39×10^2	72.73	12.08	1.082
	4.00	7.31×10^3	79.36	9.94	1.259
5.0	1.10	5.44×10^1	35.04	40.26	1.007
	2.20	1.57×10^3	72.78	16.04	1.060
	4.00	1.61×10^4	67.99	14.63	1.253

Table 4.4: Time-averaged properties in the supercritical regime for the case BI at $E = 3 \times 10^{-4}$.

4.7 Summary and conclusions

The qualitative aspects of the dynamics in the compressible models show a preference of the flow to concentrate in certain regions. This can be a fraction of the shell viewed in an equatorial cut or the region close to the outer boundary at higher latitudes in a meridional view. The bifurcation scenario is shortened in the Ra space and therefore, chaotic convection is achieved at lower Ra than in the Boussinesq case. Convection was never space-filling, however, the Rayleigh numbers were not that large. Convection inside the tangent cylinder is always present at lower Ra in the chaotic regime, while in the Boussinesq case it is not present up to $Ra = 10Ra_c$, even in the chaotic regime (see also Grote et al., 2001).

One of the most striking features is indeed connected to the capability of the system to develop thermal inertial waves and columnar convection simultaneously. A local Prandtl number that decreases with radius allows for regions close to the inner boundary with moderate Pr for columnar convection, and very small Pr close to the outer boundary for wall-attached convection. The numerical studies of Simitev and Busse (2003) for incompressible fluids have shown that thermal inertial waves persist in the non-linear regime. Our results at larger Ra do not show much resemblance to the non-linear results in Simitev and Busse (2003)'s studies. Convection is still present close to the outer boundary, although much of the regularly spaced pattern is lost.

The kinetic energy in the zonal flow increases with Co although the convective velocities have lost part or much of their geostrophy. A rigorous study of the Reynolds stresses will reveal the role played by the reference density in the generation and maintenance of zonal flow.

The zonal winds in the upper atmosphere of the giant planets are characterised by a fast equatorial prograde jet with weaker jets at higher latitudes, alternating in direction for Jupiter and mostly prograde for Saturn, as figure 0.2 shows (Ingersoll et al., 1981). This intensity difference between equatorial to higher latitudes flow is qualitatively captured by the compressible models, especially at large Co. Further studies of the parameter space, specially in thinner shells, have to be performed to see whether alternating zonal flow is promoted when the background density is no longer constant. The presence of strong prograde zonal flow at $Co = 5$ for the case A opens the door to new scenarios to explain Saturn's surface-dynamics.

Conclusions and perspectives

The increase in computing power during the last years made possible to study time-dependent, three-dimensional solutions of more complex and more realistic models in still manageable times and with adequate resolutions. The widely assumed Boussinesq approximation can now be extended to include compressibility effects for studies of, for example, the molecular envelope of the giant planets.

The commonly employed anelastic approximation (Ogura and Phillips, 1962; Gough, 1969) includes the effects of compressibility but filters out fast acoustic waves which would otherwise require a much smaller numerical time step. In the limit of vanishing Grüneisen parameter, the thermal effects due to compressibility, i.e. adiabatic and viscous heatings, do not contribute. This limit simplifies the traditional anelastic approximation, leading to a problem with a nearly unmodified temperature equation, and the same number of non-linearities as in the Boussinesq case. This new approach to the compressible problem was employed here. Since it hasn't been developed before, programming to implement the new theory and various testings were necessary. Whether it is reasonable to neglect the adiabatic and viscous heatings for the molecular envelope of the giant planets remains to be clarified, since the required estimate of the Dissipation number (see §1.3.2) is not yet avaliable.

The dimensionless numbers, i.e. the control parameters of the system, are constant throughout the shell in the Boussinesq case. In the compressible case, on the other hand, they change locally with radius according to the radial variation of the background density and other fluid properties (see §1.4.2). This complicates the interpretation of the solution since it is hard to distinguish whether a certain feature is the consequence of locally different parameters or other compressibility effects. However, the particular choice of constant kinematic viscosity and thermal diffusivity leads to a model (named A in the study) where the dimensionless parameters are independent of depth.

An ideal gas was assumed for simplicity. This assumption is possibly not valid in deeper regions of the molecular envelope where the fluid behaves progressively more non-ideal due to high temperatures and pressures. According to the statistical physics of an ideal gas, kinematic viscosity and thermal diffusivity are proportional and therefore, they must obey the same radial dependence. The assumption that both are constant leads to the simplest compressible model as already discussed.

The onset of convection has been explored in previous anelastic studies (Glatzmaier and Gilman, 1981a; Drew et al., 1995). However, some aspects of the solution like the location of the convective instability depending on the radially dependent fluid properties and the degree of stratification remained unclear. This point is further investigated in our work exploring onset of convection for different models (see §2.3.1 and §2.3.2).

The convective instability takes place near the inner boundary of the shell in the Boussinesq case. For compressible models this is not necessarily the case. When the thermal conductivity remained constant, we found onset of convection near the inner boundary for every degree of stratification of the fluid. However, in models where it depends linearly on the density background (which implies that thermal diffusivity remained constant), the convective instability locates close to the outer boundary at moderate to large compressibilities. In the Boussinesq case, the location of the convective instability is intimately related to the temperature profile before convection sets in, when the heat is transported only by thermal conduction. This also holds for the compressible case, where the conductive temperature profile depends on the compressibility and thermal conductivity of the fluid (see §2.3.3).

Onset close to the outer boundary is a remarkable effect of compressible convection. However, compressibility not only affects the location of the convective instability. The scale of the flow reduces with compressibility no matter where the convection is located. As a consequence, a higher degree of flow confinement towards one of the boundaries is observed with increasing stratification.

Asymptotic laws in the limit of high rotation describe convection onset in the Boussinesq case (Roberts, 1968; Busse, 1970). Our results, though in the moderate rotation regime ($E = 10^{-3} - 3 \times 10^{-4}$), suggest that these laws may roughly hold in the compressible case.

Beyond onset, in the non-linear regime, different time behaviours of the flow have been identified in the Boussinesq case (see e.g. Grote and Busse, 2001; Christensen, 2002; Simitev and Busse, 2003). Drifting, vacillating, chaotic and intermittent convection are successively observed when increasing the Rayleigh number to ultimately reach strongly chaotic convection, filling the whole volume of the shell. In the compressible case, drifting, chaotic and intermittent convection have been identified. Vacillating convection may exist in a very small region of the Rayleigh number space not covered by the calculations. Chaotic space filling convection was not observed, however, the Rayleigh numbers were not too large ($< Ra = 5 \times Ra_c$). These different transitions occur at much lower Ra than in the Boussinesq case: when the regime is still drifting in the Boussinesq case, it is already chaotic in the compressible case (§4.3).

The flow structure shows large motionless regions (except for the zonal flow) in the equatorial plane which partly extend to the rest of the shell. Near the outer boundary at high latitudes convection is much stronger than at the equatorial plane. Examining the flow at the equatorial plane, a common practice in the incompressible convection, can therefore be misleading in compressible convection. The polar regions which exhibit insignificant flow in the Boussinesq case (see also Grote et al., 2001) are convecting in the compressible case. In addition, the scale of the convection is much smaller compared to the corresponding incompressible counterpart.

Spiralling columnar convection and thermal inertial waves are different convective modes, which are preferred depending mainly on the Prandtl number. They have different characteristics and do not appear together in the Boussinesq case. Compressible convection allows for regions with different local Prandtl numbers, and therefore, these two different modes can be present at the same time in the shell as we have observed (§4.5.2). This finding is remarkable since it is the first time that these two types of convection are seen together in a convecting shell. Whether this scenario is plausible for the giant planets is unclear. In particular, this result have little physical relevance for an ideal gas since the linear relationship between thermal diffusivity and kinematic viscosity is violated in the respective model. However, the molecular hydrogen envelope of the giant planets do not resemble an ideal gas in deeper regions and, therefore, the relationship between the fluid properties might be changed.

The zonal winds in the upper atmosphere of the giant planets are characterised by a fast equatorial prograde jet with weaker jets at higher latitudes, alternating in direction for Jupiter and mostly prograde for Saturn (Ingersoll et al., 1981). This intensity difference between equatorial to higher latitudes flow is qualitatively captured by the compressible models, especially at large compressibilities. Recent incompressible models for Jupiter were able to capture the alternating zonal flow structure at higher latitudes (Heimpel et al., 2005), which had not been reproduced in previous studies (Christensen, 2001; Aurnou and Olson, 2001). They assumed a shell with a thickness of only 10% ($\eta = 0.9$) of the total planetary radius as suggested by recent estimates (Guillot et al., 2004). A pair of stronger jets developed outside the tangent cylinder and weaker multiple jets inside it. Different flow regimes inside and outside the tangent cylinder, thus, explain the difference in jet amplitude. Although we didn't observe alternating zonal flows, a strong decrease of the flow with latitude is an inherent feature at large compressibility even for thicker shells. Therefore, compressible models with parameters describing as best as possible the current estimates for the giant planets are required to study the jet structure as well as the wind intensity for each planet.

A Fully compressible equations in spherical coordinates

A.1 Continuity equation

$$\frac{\partial \rho}{\partial t} + \frac{1}{r^2}\frac{\partial}{\partial r}(r^2 \rho u_r) + \frac{1}{r\sin\theta}\frac{\partial}{\partial\theta}(\sin\theta \rho u_\theta) + \frac{1}{r\sin\theta}\frac{\partial}{\partial\varphi}(\rho u_\varphi) = 0 \tag{A.1}$$

A.2 Navier-Stokes equation

$$\begin{aligned}\hat{r}: \quad & \rho\Big(\frac{\partial u_r}{\partial t} + u_r\frac{\partial u_r}{\partial r} + \frac{u_\theta}{r}\frac{\partial u_r}{\partial\theta} + \frac{u_\varphi}{r\sin\theta}\frac{\partial u_r}{\partial\varphi} - \frac{u_\theta^2}{r} - \frac{u_\varphi^2}{r}\Big) = \\ & \qquad -\frac{\partial p}{\partial r} - \rho g + 2\rho\Omega u_\varphi \sin\theta + F_r\end{aligned} \tag{A.2}$$

$$\begin{aligned}\hat{\theta}: \quad & \rho\Big(\frac{\partial u_\theta}{\partial t} + u_r\frac{\partial u_\theta}{\partial r} + \frac{u_\theta}{r}\frac{\partial u_\theta}{\partial\theta} + \frac{u_\varphi}{r\sin\theta}\frac{\partial u_\theta}{\partial\varphi} + \frac{u_r u_\theta}{r} - \frac{u_\varphi^2\cot\theta}{r}\Big) = \\ & \qquad -\frac{1}{r}\frac{\partial p}{\partial\theta} + 2\rho\Omega u_\varphi \cos\theta + F_\theta\end{aligned} \tag{A.3}$$

$$\begin{aligned}\hat{\varphi}: \quad & \rho\Big(\frac{\partial u_\varphi}{\partial t} + u_r\frac{\partial u_\varphi}{\partial r} + \frac{u_\theta}{r}\frac{\partial u_\varphi}{\partial\theta} + \frac{u_\varphi}{r\sin\theta}\frac{\partial u_\varphi}{\partial\varphi} + \frac{u_r u_\varphi}{r} + \frac{u_\theta u_\varphi\cot\theta}{r}\Big) = \\ & \qquad -\frac{1}{r\sin\theta}\frac{\partial p}{\partial\varphi} - 2\rho\Omega(u_\theta\cos\theta + u_r\sin\theta) + F_\theta\end{aligned} \tag{A.4}$$

where F_r, F_θ, F_φ are the spherical components of the viscous force.

A.2.1 Viscous force

The components of the viscous force in spherical coordinates are obtained with

$$\begin{aligned}F_r &= \frac{1}{r^2}\frac{\partial}{\partial r}(r^2\tau_{rr}) + \frac{1}{r\sin\theta}\frac{\partial}{\partial\theta}(\sin\theta\tau_{r\theta}) + \frac{1}{r\sin\theta}\frac{\partial\tau_{r\varphi}}{\partial\varphi} - \frac{\tau_{\theta\theta}}{r} - \frac{\tau_{\varphi\varphi}}{r} \\ F_\theta &= \frac{1}{r^2}\frac{\partial}{\partial r}(r^2\tau_{r\theta}) + \frac{1}{r\sin\theta}\frac{\partial}{\partial\theta}(\sin\theta\tau_{\theta\theta}) + \frac{1}{r\sin\theta}\frac{\partial\tau_{\theta\varphi}}{\partial\varphi} + \frac{\tau_{r\theta}}{r} - \frac{\cot\theta\tau_{\varphi\varphi}}{r} \\ F_\varphi &= \frac{1}{r^2}\frac{\partial}{\partial r}(r^2\tau_{r\varphi}) + \frac{1}{r\sin\theta}\frac{\partial}{\partial\theta}(\sin\theta\tau_{\theta\varphi}) + \frac{1}{r\sin\theta}\frac{\partial\tau_{\varphi\varphi}}{\partial\varphi} + \frac{\tau_{r\varphi}}{r} + \frac{\cot\theta\tau_{\theta\varphi}}{r}\end{aligned} \tag{A.5}$$

where τ_{ij} are the components of the deviatoric stress tensor in spherical coordinates. For a Newtonian, isotropic fluid the relation between deviatoric stress tensor τ_{ij} and strain rate tensor e_{ij} is

$$\tau_{ij} = 2\mu e_{ij} + \Big(k_B - \frac{2}{3}\mu\Big)(\boldsymbol{\nabla}\cdot\boldsymbol{u})\delta_{ij} \tag{A.6}$$

where k_B is known as bulk viscosity. The bulk viscosity is a measure of the dissipation under compression or expansion, which is very small for many fluids. For that reason we will neglect k_B, assumption often referred in the literature as Stokes assumption. The dilatation $\boldsymbol{\nabla}\cdot\boldsymbol{u}$ is equal to e_{kk} where the Einstein convention for summation applies.

The components of the tensor (A.6) written in spherical coordinates are

$$\begin{array}{lll} \tau_{rr} = 2\mu(e_{rr} - \frac{1}{3}\boldsymbol{\nabla}\cdot\boldsymbol{u}) & \tau_{r\theta} = 2\mu e_{r\theta} & \tau_{r\varphi} = 2\mu e_{r\varphi} \\ & \tau_{\theta\theta} = 2\mu(e_{\theta\theta} - \frac{1}{3}\boldsymbol{\nabla}\cdot\boldsymbol{u}) & \tau_{\theta\varphi} = 2\mu e_{\theta\varphi} \\ & & \tau_{\varphi\varphi} = 2\mu(e_{\varphi\varphi} - \frac{1}{3}\boldsymbol{\nabla}\cdot\boldsymbol{u}) \end{array} \tag{A.7}$$

where the components of e_{ij} expressed in spherical coordinates are

$$\begin{array}{lll} e_{rr} = \dfrac{\partial u_r}{\partial r} & e_{r\theta} = \dfrac{r}{2}\dfrac{\partial}{\partial r}(\dfrac{u_\theta}{r}) + \dfrac{1}{2r}\dfrac{\partial u_r}{\partial \theta} & e_{r\varphi} = \dfrac{r}{2}\dfrac{\partial}{\partial r}(\dfrac{u_\varphi}{r}) + \dfrac{1}{2r\sin\theta}\dfrac{\partial u_r}{\partial \varphi} \\ & e_{\theta\theta} = \dfrac{1}{r}\dfrac{\partial u_\theta}{\partial \theta} + \dfrac{u_r}{r} & e_{\theta\varphi} = \dfrac{\sin\theta}{2r}\dfrac{\partial}{\partial \theta}(\dfrac{u_\varphi}{\sin\theta}) + \dfrac{1}{2r\sin\theta}\dfrac{\partial u_\theta}{\partial \varphi} \\ & & e_{\varphi\varphi} = \dfrac{1}{r\sin\theta}\dfrac{\partial u_\varphi}{\partial \varphi} + \dfrac{u_r}{r} + \dfrac{u_\theta\cot\theta}{r} \end{array} \tag{A.8}$$

$$\begin{array}{lll} e_{rr} = \frac{\partial u_r}{\partial r} & e_{r\theta} = \frac{r}{2}\frac{\partial}{\partial r}(\frac{u_\theta}{r}) + \frac{1}{2r}\frac{\partial u_r}{\partial \theta} & e_{r\varphi} = \frac{r}{2}\frac{\partial}{\partial r}(\frac{u_\varphi}{r}) + \frac{1}{2r\sin\theta}\frac{\partial u_r}{\partial \varphi} \\ & e_{\theta\theta} = \frac{1}{r}\frac{\partial u_\theta}{\partial \theta} + \frac{u_r}{r} & e_{\theta\varphi} = \frac{\sin\theta}{2r}\frac{\partial}{\partial \theta}(\frac{u_\varphi}{\sin\theta}) + \frac{1}{2r\sin\theta}\frac{\partial u_\theta}{\partial \varphi} \\ & & e_{\varphi\varphi} = \frac{1}{r\sin\theta}\frac{\partial u_\varphi}{\partial \varphi} + \frac{u_r}{r} + \frac{u_\theta\cot\theta}{r} \end{array} \tag{A.9}$$

When the components of the viscous force in (A.5) are formally developed, one can find the spherical components of $\boldsymbol{D}(\boldsymbol{\nabla}\mu, \boldsymbol{u}, \partial\boldsymbol{u})$ in the viscous force (1.4):

$$\begin{aligned} D_r = {} & 2\frac{\partial \mu}{\partial r}\Big(\frac{\partial u_r}{\partial r} - \frac{1}{3}(\boldsymbol{\nabla}\cdot\boldsymbol{u})\Big) + \frac{1}{r}\frac{\partial \mu}{\partial \theta}\Big(r\frac{\partial}{\partial r}(\frac{u_\theta}{r}) + \frac{1}{r}\frac{\partial u_r}{\partial \theta}\Big) \\ & + \frac{1}{r\sin\theta}\frac{\partial \mu}{\partial \varphi}\Big(r\frac{\partial}{\partial r}(\frac{u_\varphi}{r}) + \frac{1}{r\sin\theta}\frac{\partial u_r}{\partial \varphi}\Big) \end{aligned}$$

$$\begin{aligned} D_\theta = {} & \frac{\partial \mu}{\partial r}\Big(r\frac{\partial}{\partial r}(\frac{u_\theta}{r}) + \frac{1}{r}\frac{\partial u_r}{\partial \theta}\Big) + \frac{2}{r}\frac{\partial \mu}{\partial \theta}\Big(\frac{1}{r}\frac{\partial u_\theta}{\partial \theta} + \frac{u_r}{r} - \frac{1}{3}(\boldsymbol{\nabla}\cdot\boldsymbol{u})\Big) \\ & + \frac{1}{r\sin\theta}\frac{\partial \mu}{\partial \varphi}\Big(\frac{\sin\theta}{r}\frac{\partial}{\partial \theta}(\frac{u_\varphi}{\sin\theta}) + \frac{1}{r\sin\theta}\frac{\partial u_\theta}{\partial \varphi}\Big) \end{aligned} \tag{A.10}$$

$$D_\varphi = \frac{\partial \mu}{\partial r}\Big(r\frac{\partial}{\partial r}(\frac{u_\varphi}{r}) + \frac{1}{r\sin\theta}\frac{\partial u_r}{\partial \varphi}\Big) + \frac{1}{r}\frac{\partial \mu}{\partial \theta}\Big(\frac{\sin\theta}{r}\frac{\partial}{\partial \theta}(\frac{u_\varphi}{\sin\theta}) + \frac{1}{r\sin\theta}\frac{\partial u_\theta}{\partial \phi}\Big)$$
$$+ \frac{2}{r\sin\theta}\frac{\partial \mu}{\partial \varphi}\Big(\frac{1}{r\sin\theta}\frac{\partial u_\varphi}{\partial \varphi} + \frac{u_r + u_\theta cot\theta}{r} - \frac{1}{3}(\boldsymbol{\nabla}\cdot\boldsymbol{u})\Big)$$

A.3 Energy equation

$$\rho C_p\frac{DT}{Dt} - \alpha T\frac{Dp}{Dt} = \\ \frac{1}{r^2}\frac{\partial}{\partial r}\Big(kr^2\frac{\partial T}{\partial r}\Big) + \frac{1}{r^2\sin\theta}\frac{\partial}{\partial \theta}\Big(k\sin\theta\frac{\partial T}{\partial \theta}\Big) + \frac{1}{r^2(\sin\theta)^2}\frac{\partial}{\partial \varphi}\Big(k\frac{\partial T}{\partial \varphi}\Big) + \Phi, \tag{A.11}$$

where D/Dt is the substantive time derivative

$$\frac{D}{Dt} = \frac{\partial}{\partial t} + u_r\frac{\partial}{\partial r} + \frac{u_\theta}{r}\frac{\partial}{\partial \theta} + \frac{u_\varphi}{r\sin\theta}\frac{\partial}{\partial \varphi}. \tag{A.12}$$

A.3.1 Viscous dissipation

The viscous dissipation Φ is given by

$$\Phi = \tau_{ij}\frac{\partial u_i}{\partial x_j}, \tag{A.13}$$

which for a Newtonian, isotropic fluid is described by

$$\Phi = 2\mu e_{ij}e_{ij} + \Big(k_B - \frac{2}{3}\mu\Big)(\boldsymbol{\nabla}\cdot\boldsymbol{u})^2. \tag{A.14}$$

B Anelastic approximation with zero Grüneisen parameter: Detailed scale analysis

The scale analysis shown here follows Gilman and Glatzmaier (1981) 's derivations for the standard anelastic case.

Each dependent variable f is expressed as the sum of the reference state $\widetilde{f}$ and the perturbations resulting from convection f':

$$\begin{aligned} \rho(r,\theta,\varphi,t) &= \widetilde{\rho}(r) + \rho'(r,\theta,\varphi,t) \\ p(r,\theta,\varphi,t) &= \widetilde{p}(r) + p'(r,\theta,\varphi,t) \\ T(r,\theta,\varphi,t) &= \widetilde{T}_o + T'(r,\theta,\varphi,t). \end{aligned} \tag{B.1}$$

This scale separation is introduced into the fully compressible fluid equations. The terms ordered ϵ^0 give the reference state equations and the terms up to the next lowest order give the perturbation equations. Therefore, to perform formally the scale analysis the order in ϵ of all the variables, fluid properties and operators has to be determined[1]. These results are summarised in Table B.1.

The fluid velocity $\boldsymbol{u}$ is of order $\epsilon^{1/2}$ as it can be deduced from (1.26). The same result can be found following energetic considerations (Gough, 1969; Gilman and Glatzmaier, 1981). Since $\boldsymbol{u}$ is of order $\epsilon^{1/2}$, the convective time scale is of order $\epsilon^{-1/2}$ causing $\dfrac{\partial}{\partial t} \sim \epsilon^{1/2}$.

The convective velocity scales as $\widetilde{\nu}/d$ where d is the thickness of the shell. Because $\boldsymbol{u} \sim \epsilon^{1/2}$ then $\widetilde{\nu} \sim \epsilon^{1/2}$. Since $\widetilde{\mu} = \widetilde{\rho\nu}$ then $\widetilde{\mu} \sim \epsilon^{1/2}$. Similar arguments hold for $\widetilde{\kappa}$ and $\widetilde{k}$.

The angular velocity $\boldsymbol{\Omega}$ is of order $\epsilon^{1/2}$ (Gilman and Glatzmaier, 1981). A simple way to see this is taking into account that p' scales with $\widetilde{\rho}\Omega\widetilde{\nu}$.

Perturbations in ν' and κ' will be set to zero since the uncertainty in these fluid properties is great (Gilman and Glatzmaier, 1981).

---

[1] See also DeRosa (2001).

Order in ϵ	Quantities	Operators
ϵ^0	$\widetilde{\rho}$, $\widetilde{p}$, $\widetilde{\boldsymbol{g}}$	$\boldsymbol{\nabla}$,$\boldsymbol{\nabla}\cdot$, $\boldsymbol{\nabla}\times$
$\epsilon^{1/2}$	$\boldsymbol{u}$, $\widetilde{\mu}$, $\widetilde{\nu}$, $\widetilde{k}$, $\widetilde{\kappa}$, $\boldsymbol{\Omega}$	$\dfrac{\partial}{\partial t}$
ϵ	ρ', p', T', $\boldsymbol{g'}$	–

Table B.1: Order in ϵ for all thermodynamic variables, fluid properties and operators appearing in the fully compressible formalism.

B.1 Equation of state

Introducing the scale separation (B.1) into the equation of state of an ideal gas (1.5) we obtain

$$\underbrace{p'}_{\sim\epsilon} = \underbrace{\underbrace{\widetilde{\rho}R^*\widetilde{T}_o - \widetilde{p}}_{=0}}_{\sim\epsilon^0} + \underbrace{\widetilde{\rho}R^*T' + \rho'R^*\widetilde{T}_o}_{\sim\epsilon} + \underbrace{\rho'R^*T'}_{\epsilon^2}. \tag{B.2}$$

Rearranging the first-order terms (ϵ^1) we obtain

$$\frac{p'}{\widetilde{p}} = \frac{\rho'}{\widetilde{\rho}} + \frac{T'}{\widetilde{T}_o} \tag{B.3}$$

which can also be written as

$$\rho = \widetilde{\rho}(1 - \widetilde{\alpha}T' + \widetilde{\chi}_T p') = \widetilde{\rho} + \rho' \tag{B.4}$$

using that for an ideal gas $1/\widetilde{T}_o = \widetilde{\alpha}$ and $1/\widetilde{p} = \widetilde{\chi}_T$.

B.2 Continuity equation

The continuity equation (1.1) can be written as

$$\underbrace{\frac{\partial\widetilde{\rho}}{\partial t}}_{=0} + \underbrace{\frac{\partial\rho'}{\partial t}}_{vanishes} + \underbrace{\boldsymbol{\nabla}\cdot(\widetilde{\rho}\boldsymbol{u})}_{\sim\epsilon^{1/2}} + \underbrace{\boldsymbol{\nabla}\cdot(\rho'\boldsymbol{u})}_{\sim\epsilon^{3/2}} = 0, \tag{B.5}$$

where the condition of vanishing $\dfrac{\partial\rho'}{\partial t}$ is imposed to filter out acoustic waves. Looking closely, $\dfrac{\partial\rho'}{\partial t} \sim \epsilon^{3/2}$. This is a consequence of (1.26) and removes sound waves from the problem since the term is of higher order. However, we explicitly insist that $\dfrac{\partial\rho'}{\partial t}$ must vanish because in the anelastic approximation the condition (1.10) has to be fulfilled no matter the order in ϵ of this term.

B.3 Navier-Stokes equation

The Navier-Stokes equation (1.2) can be written as

$$\underbrace{\widetilde{\rho}\frac{\partial \boldsymbol{u}}{\partial t} + \widetilde{\rho}(\boldsymbol{u}\cdot\boldsymbol{\nabla})\boldsymbol{u}}_{\sim\epsilon} + \underbrace{\rho'\frac{\partial \boldsymbol{u}}{\partial t} + \rho'(\boldsymbol{u}\cdot\boldsymbol{\nabla})\boldsymbol{u}}_{\sim\epsilon^2} = \underbrace{\underbrace{-\boldsymbol{\nabla}\widetilde{p} + \widetilde{\rho}\widetilde{\boldsymbol{g}}}_{=0}}_{\sim\epsilon^0}$$
$$\underbrace{-\boldsymbol{\nabla}p' + \rho'\widetilde{\boldsymbol{g}} + \widetilde{\rho}\boldsymbol{g'} - 2\widetilde{\rho}\boldsymbol{\Omega}\times\boldsymbol{u} + \boldsymbol{F_a}}_{\sim\epsilon} + \underbrace{\rho'\boldsymbol{g'} - 2\rho'\boldsymbol{\Omega}\times\boldsymbol{u} + \boldsymbol{F'}}_{\sim\epsilon^2}. \tag{B.6}$$

The viscous force $\boldsymbol{F}$ given in (1.4) is separated in

$$\boldsymbol{F_a} = \widetilde{\rho}\widetilde{\nu}\boldsymbol{\nabla}^2\boldsymbol{u} + \frac{1}{3}\widetilde{\rho}\widetilde{\nu}\boldsymbol{\nabla}(\boldsymbol{\nabla}\cdot\boldsymbol{u}) + \frac{d(\widetilde{\rho}\widetilde{\nu})}{dr}\Big[\frac{1}{r}\boldsymbol{\nabla}(ru_r) + r\frac{\partial}{\partial r}(\frac{\boldsymbol{u}}{r}) - \frac{2}{3}(\boldsymbol{\nabla}\cdot\boldsymbol{u})\hat{r}\Big], \tag{B.7}$$

as given in (1.32), and

$$\boldsymbol{F'} = \rho'\widetilde{\nu}\boldsymbol{\nabla}^2\boldsymbol{u} + \frac{1}{3}\rho'\widetilde{\nu}\boldsymbol{\nabla}(\boldsymbol{\nabla}\cdot\boldsymbol{u}) + \boldsymbol{D}(\boldsymbol{\nabla}(\rho'\widetilde{\nu}), \boldsymbol{u}, \partial\boldsymbol{u}) \tag{B.8}$$

with $\boldsymbol{D}$ given in (A.10). The explicit dependence of the shear viscosity μ on density, i.e. $\mu = \rho\nu$ where ν is the kinematic viscosity, was already considered in $\boldsymbol{F_a}$ and $\boldsymbol{F'}$.

B.4 Energy equation

The energy equation (1.3) can be written as

$$\underbrace{\widetilde{\rho}C_p\frac{\partial T'}{\partial t} + \widetilde{\rho}C_p\,\boldsymbol{u}\cdot\boldsymbol{\nabla}T'}_{\epsilon^{3/2}} + \underbrace{\rho' C_p\,\frac{\partial T'}{\partial t}}_{\epsilon^{5/2}} - \underbrace{\widetilde{\alpha}(\widetilde{T}_o + T')\boldsymbol{u}\cdot\boldsymbol{\nabla}\widetilde{p}}_{\epsilon^{3/2}} \tag{B.9}$$
$$-\underbrace{\widetilde{\alpha}\widetilde{T}_o\left(\frac{\partial p'}{\partial t} + \boldsymbol{u}\cdot\boldsymbol{\nabla}p'\right)}_{\epsilon^{3/2}} - \underbrace{\widetilde{\alpha}T'\left(\frac{\partial p'}{\partial t} + \boldsymbol{u}\cdot\boldsymbol{\nabla}p'\right)}_{\epsilon^{5/2}} = \underbrace{\boldsymbol{\nabla}(\widetilde{k}(\boldsymbol{\nabla}T'))}_{\epsilon^{3/2}} + \underbrace{\Phi_a}_{\sim\epsilon^{3/2}} + \underbrace{\Phi'}_{\sim\epsilon^{5/2}},$$

where the viscous heating Φ given in (A.13) is separated in

$$\Phi_a = 2\widetilde{\rho}\widetilde{\nu}e_{ij}e_{ij} + \frac{2}{3}\widetilde{\rho}\widetilde{\nu}(\boldsymbol{\nabla}\cdot\boldsymbol{u})^2, \tag{B.10}$$

and

$$\Phi' = 2\rho'\widetilde{\nu}e_{ij}e_{ij} + \frac{2}{3}\rho'\widetilde{\nu}(\boldsymbol{\nabla}\cdot\boldsymbol{u})^2. \tag{B.11}$$

The viscous and adiabatic heatings are negligible compared to the other terms in the limit of $\mathit{\Gamma} \rightarrow 0$, or equally $Di \rightarrow 0$. Describing the equation in non-dimensional description makes this point evident. Using the shell thickness d as length scale,

$d^2/\widetilde{\nu}_o$ as time scale, the temperature contrast ΔT between the inner and the outer boundary as temperature scale, $\widetilde{\rho}_o$, as density scale, and $\hat{\rho}\Omega\hat{\nu}$ as pressure scale, the equation given in (B.9) to order $\epsilon^{3/2}$ is given by

$$\begin{aligned} Pr\hat{\rho}\Big(\frac{\partial T'}{\partial t} + \boldsymbol{u}\cdot\boldsymbol{\nabla}T'\Big) + Di\hat{\rho}(\hat{T}_o + T)u_r - \frac{DiPr}{RaE}\Big(\frac{\partial p'}{\partial t} + \boldsymbol{u}\cdot\boldsymbol{\nabla}p'\Big) \\ = \boldsymbol{\nabla}\big(\hat{k}\boldsymbol{\nabla}T\big) + \frac{DiPr}{Ra}\Phi_a. \end{aligned} \tag{B.12}$$

Therefore, since the Dissipation number scales the adiabatic and viscous heatings, they are neglected in the limit $Di \rightarrow 0$.

C Derivations in spectral space

C.1 Viscous force

C.1.1 Preliminaries

The horizontal divergence is an operator defined as the divergence in the horizontal direction (or in other words, the direction perpendicular to the radial one) as

$$\boldsymbol{\nabla}_H \cdot \boldsymbol{G} = \boldsymbol{\nabla} \cdot \boldsymbol{G} - \frac{1}{r^2}\frac{\partial}{\partial r}(r^2 G_r) = \frac{1}{r\sin\theta}\Big(\frac{\partial}{\partial\theta}(\sin\theta G_\theta) + \frac{\partial G_\varphi}{\partial\varphi}\Big). \tag{C.1}$$

In deriving the viscous force in the form required by the code the following three identities are very handy:

$$\boldsymbol{\nabla} \cdot \boldsymbol{u} = -\frac{u_r}{\hat\rho}\frac{d\hat\rho}{dr}, \tag{C.2}$$

$$\boldsymbol{\nabla}_H \cdot \big(\hat\rho\boldsymbol{u}\big) = -\frac{1}{r^2}\frac{\partial}{\partial r}\big(r^2\hat\rho u_r\big), \tag{C.3}$$

both arising from the divergence-free mass-flux condition, and

$$\big(\nabla^2\boldsymbol{G}\big)_r = \frac{1}{r^2}\frac{\partial^2}{\partial r^2}\big(r^2 G_r\big) + \frac{1}{r^2}\mathcal{L}^2 G_r - \frac{2}{r}\boldsymbol{\nabla}\cdot\boldsymbol{G} \tag{C.4}$$

where $\mathcal{L}^2$ is given in (1.51). When $\boldsymbol{G} = \hat\rho\boldsymbol{u}$, the last term in the right hand side of (C.4) vanishes due to the divergence-free mass-flux condition.
To simplify the notation we will rename the density gradient as

$$h_\rho = \frac{1}{\hat\rho}\frac{d\hat\rho}{dr} \tag{C.5}$$

which is in fact the inverse of the density scale height (1.21) aside from a possible difference in sign.

C.1.2 $\hat\nu$ constant

The radial component of (1.39), its horizontal divergence and radial curl are written in spectral space as

$$(\boldsymbol{F}_v)_r = -\frac{\ell(\ell+1)}{\hat\rho r^2}\left[-\frac{\partial^2 W}{\partial r^2}+\frac{1}{3}h_\rho\frac{\partial W}{\partial r}+\left[\frac{4}{3}\Big(\frac{1}{r}h_\rho-h_\rho^2+\frac{1}{\hat\rho}\frac{d^2\hat\rho}{dr^2}\Big)+\frac{\ell(\ell+1)}{r^2}\right]\right]W, \tag{C.6}$$

$$\nabla_H \cdot (\boldsymbol{F}_v) = \frac{\ell(\ell+1)}{\hat{\rho} r^2}\Bigg[-\frac{\partial^3 W}{\partial r^3} + h_\rho \frac{\partial^2 W}{\partial r^2} + \left[\frac{2}{r} h_\rho - h_\rho^2 + \frac{1}{\hat{\rho}}\frac{d^2\hat{\rho}}{dr^2} + \frac{\ell(\ell+1)}{r^2}\right]\frac{\partial W}{\partial r} - \left[\frac{2}{3}\frac{1}{r^2} h_\rho + \frac{2}{r^3}\right]\ell(\ell+1)W\Bigg], \tag{C.7}$$

and

$$\big(\boldsymbol{\nabla} \times \boldsymbol{F}_v\big)_r = -\frac{\ell(\ell+1)}{\hat{\rho} r^2}\left[-\frac{\partial^2 Z}{\partial r^2} + h_\rho \frac{\partial Z}{\partial r} + \Big(\frac{2}{r} h_\rho - h_\rho^2 + \frac{1}{\hat{\rho}}\frac{d^2\hat{\rho}}{dr^2} + \frac{\ell(\ell+1)}{r^2}\Big) Z\right] \tag{C.8}$$

respectively.

C.1.3 $\hat{\mu}$ constant

The radial component of (1.42), its horizontal divergence and radial curl are written in spectral space as

$$(\boldsymbol{F}_v)_r = -\frac{\ell(\ell+1)}{\hat{\rho}^2 r^2}\left[-\frac{\partial^2 W}{\partial r^2} + \frac{7}{3} h_\rho \frac{\partial W}{\partial r} + \left[\frac{4}{3}\Big(-2\frac{h_\rho}{r} - 2h_\rho^2 + \frac{1}{\hat{\rho}}\frac{d^2\hat{\rho}}{dr^2}\Big) + \frac{\ell(\ell+1)}{r^2}\right]\right] W, \tag{C.9}$$

$$\nabla_H \cdot (\boldsymbol{F}_v) = \frac{\ell(\ell+1)}{\hat{\rho}^2 r^2}\Bigg[-\frac{\partial^3 W}{\partial r^3} + 2h_\rho \frac{\partial^2 W}{\partial r^2} + \Big(-2h_\rho^2 + \frac{1}{\hat{\rho}}\frac{d^2\hat{\rho}}{dr^2} + \frac{\ell(\ell+1)}{r^2}\Big)\frac{\partial W}{\partial r} + \Big(\frac{1}{3}\frac{h_\rho}{r^2} - \frac{2}{r^3}\Big)\ell(\ell+1)W\Bigg], \tag{C.10}$$

and

$$\big(\boldsymbol{\nabla} \times \boldsymbol{F}_v\big)_r = -\frac{\ell(\ell+1)}{\hat{\rho}^2 r^2}\left[-\frac{\partial^2 Z}{\partial r^2} + 2h_\rho \frac{\partial Z}{\partial r} + \Big(-2h_\rho^2 + \frac{1}{\hat{\rho}}\frac{d^2\hat{\rho}}{dr^2} + \frac{\ell(\ell+1)}{r^2}\Big) Z\right] \tag{C.11}$$

respectively.

C.2 Kinetic energy density

The kinetic energy density $E_k^* = \frac{1}{2V_s}\int_{V_s} \hat{\rho} u^2 dV$ is described in spectral space as

$$2V_s E_k^* = 2V_s(E_{pol}^* + E_{tor}^*) = \sum_{\ell,m} \ell(\ell+1) \int_{r_i}^{r_o} \frac{1}{\hat{\rho}}\left[\frac{\ell(\ell+1)}{r^2}|W_\ell^m|^2 + \left|\frac{dW_\ell^m}{dr}\right|^2\right] dr + \sum_{\ell,m} \ell(\ell+1) \int_{r_i}^{r_o} \frac{1}{\hat{\rho}}|Z_\ell^m|^2 dr, \tag{C.12}$$

where the star represents kinetic energy density not normalised by the total mass $\frac{1}{V_s}\int_{V_s} \hat{\rho} dV$.

Bibliography

Ardes, M., Busse, F., and Wicht, J. (1997). Thermal convection in rotating spherical shells. *Phys. Earth Planet. Int.*, 99:55–67.

Atkinson, D., Pollack, J., and Seiff, A. (1998). The Galileo Probe Doppler Wind Experiment: Measurement of the deep zonal winds on Jupiter. *J. Geophys. Res.*, 103:22911–22928.

Aurnou, J. and Heimpel, M. (2004). Zonal jets in rotating convection with mixed mechanical boundary conditions. *Icarus*, 169:492–498.

Aurnou, J. and Olson, P. (2001). Strong zonal winds from thermal convection in a rotating spherical shell. *Geophys. Res. Lett.*, 28:2557–2559.

Bercovici, D., Schubert, G., and Glatzmaier, G. (1992). Three-dimensional convection of an infinite-Prandtl-number compressible fluid in a basally heated spherical shell. *J. Fluid Mech.*, 239:683–719.

Braginsky, S. and Roberts, P. (1995). Equations governing convection in the Earth's core and the geodynamo. *Geophys. Astrophys. Fluid Dyn.*, 79:1–97.

Busse, F. (1970). Thermal instabilities in rapidly rotating systems. *J. Fluid Mech.*, 44:441–460.

Busse, F. (1976). A Simple Model of Convection in the Jovian Atmosphere. *Icarus*, 29:256–260.

Busse, F. (1983). A model of mean zonal flows in the major planets. *Geophys. Astrophys. Fluid Dyn.*, 23:153–174.

Busse, F. (1994). Convection driven zonal flows and vortices in the major planets. *Chaos*, 4:123–134.

Busse, F. (2002). Convective flows in rapidly rotating spheres and their dynamo action. *Phys. Fluids*, 14:1301–1314.

Busse, F. and Carrigan, C. (1976). Laboratory simulation of thermal convection in rotating planets and stars. *Science*, 191:81–83.

Carrigan, C. and Busse, F. (1983). An experimental and theoretical investigation of the onset of convection in rotating spherical shells. *J. Fluid Mech.*, 126:287–305.

Chabrier, G., Saumon, D., Hubbard, W., and Lunine, J. (1992). The molecular-metallic transition of hydrogen and the structure of Jupiter and Saturn. *Astrophys. J.*, 391:817–826.

Chandrasekhar, S. (1961). *Hydrodynamic and Hydromagnetic Stability.* Clarendon, Oxford.

Christensen, U. (2001). Zonal flow driven by deep convection in the major planets. *Geophys. Res. Lett.*, 28:2553–2556.

Christensen, U. (2002). Zonal flow driven by strongly supercritical convection in rotating spherical shells. *J. Fluid Mech.*, 470:115–133.

Christensen, U., Aubert, J., Cardin, P., Dormy, E., Gibbons, S., Glatzmaier, G., Grote, E., Honkura, Y., Jones, C., Kono, M., Matsushima, M., Sakuraba, A., Takahashi, F., Tilgner, A., Wicht, J., and Zhang, K. (2001). A numerical dynamo benchmark. *Geophys. J. Int.*, 138:393–409.

Christensen, U., Olson, P., and G.A., G. (1999). Numerical modelling of the geodynamo: a systematic parameter study. *Geophys. J. Int.*, 138:393–409.

Christensen, U. and Yuen, D. (1985). Layered convection induced by phase transitions. *J. Geophys. Res.*, 90:10,291–10,300.

DeRosa, M. (2001). *Dynamics in the Upper Solar Convection Zone.* PhD thesis, Department of Astrophysical and Planetary Sciences, University of Colorado.

Dormy, E. (1997). *Modélisation numérique de la dynamo terrestre.* PhD thesis, Institut de Physiqué du Globe de Paris.

Drew, S., Jones, C., and Zhang, K. (1995). Onset of convection in a rapidly rotating compressible fluid spherical shell. *Geophys. Astrophys. Fluid Dynamics*, 80:241–254.

Duffy, T., Vos, W., Zha, C., Hemley, R., and Mao, H. (1994). Sound velocities in dense hydrogen and the interior of Jupiter. *Science*, 263:1590–1593.

Dziewonski, A. and Anderson, D. (1981). Preliminary reference Earth model. *Phys. Earth. Planet. Int.*, 25:297–356.

Elliott, J., Miesch, M., and Toomre, J. (2000). Turbulent solar convection and its coupling with rotation: The effect of Prandtl number and thermal boundary conditions on the resulting differential rotation. *Astrophys. J.*, 533:546–556.

Evonuk, M. and Glatzmaier, G. (2004). 2d studies of various approximations used for modeling convection in giant planets. *Geophys. Astrophys. Fluid Dyn.*, 93:241–255.

Gehrels, T., Baker, L., Blenman, C., Burke, J., Castillo, N., Cofeen, D., DaCosta, B., Degewij, J., Doose, L., Esposito, L., Fountain, J., Gotobed, J., Kenknight, C., Kingston, R., McLaughlin, G., McMillan, R., Murphy, R., Smith, P., Stoll, C., Stickland, R., Tomasko, M., and Wijesinghe, M. (1980). Imaging photopolarimetry on Pionner Saturn. *Science*, 207:434–437.

Gilman, P. and Glatzmaier, G. (1981). Compressible convection in a rotating spherical shell. I. Anelastic equations. *Ap. J. Suppl.*, 45:335–349.

Glatzmaier, G. (1984). Numerical Simulations of Stellar Convective Dynamos. I. the Model and the Method. *J. Comput. Phys.*, 55:461–484.

Glatzmaier, G. (1988). Numerical simulations of mantle convection: time-dependent, three-dimensional, compressible, spherical shell. *Geophys. Astrophys. Fluid Dynamics*, 43:223–264.

Glatzmaier, G. and Gilman, P. (1981a). Compressible convection in a rotating spherical shell. II. A linear anelastic model. *Ap. J. Suppl. Ser.*, 45:351–380.

Glatzmaier, G. and Gilman, P. (1981b). Compressible convection in a rotating spherical shell. III. Analytical model for compressible vorticity waves. *Ap. J. Suppl. Ser.*, 45:381–388.

Glatzmaier, G. and Gilman, P. (1981c). Compressible convection in a rotating spherical shell. IV. Effects of viscosity, conductivity, boundary conditions, and zone depth. *Ap. J. Suppl. Ser.*, 47:103–116.

Gough, D. (1969). The anelastic approximation for thermal convection. *J. Atmos. Sci.*, 26:448–456.

Gough, D., Moore, D., Spiegel, E., and Weiss, N. (1976). Convective instability in a compressible atmosphere. II. *Astrophys. J.*, 206:536–542.

Grote, E. and Busse, F. (2001). Dynamics of convection and dynamos in rotating spherical fluid shells. *Fluid Dynamics Research*, 28:349–368.

Guillot, T. (1999). A comparison of the interiors of Jupiter and Saturn. *Planet. Space Sci.*, 47:1183–1200.

Guillot, T., Chabrier, G., Morel, P., and Gautier, D. (1994a). Nonadiabatic Models of Jupiter and Saturn. *Icarus*, 112:354–367.

Guillot, T., Gautier, D., Chabrier, G., and Mosser, B. (1994b). Are the Giant Planets Fully Convective? *Icarus*, 112:337–353.

Guillot, T., Stevenson, D., Hubbard, W., and Saumon, D. (2004). *Jupiter*, chapter 3. The Interior of Jupiter. Cambridge University Press.

Heimpel, M., Aurnou, J., and Wicht, J. (2005). Multiple zonal jets in a deep convection model of jupiter. *Nature*, accepted.

Hubbard, W. (1968). Thermal structure of Jupiter. *Astrophys. J.*, 152:745–753.

Hubbard, W. (1977). de Sitter's theory flattens Jupiter. *Icarus*, 30:1–9.

Ingersoll, A. (1990). Atmospheric dynamics of the outer planets. *Science*, 248:308–315.

Ingersoll, A., Beebe, R., Mitchell, J., Garneau, G., Yagi, G., and Müller, J.-P. (1981). Interaction of eddies and mean zonal flow on Jupiter as inferred from Voyager 1 and 2 images. *J. Geophys. Res.*, 86:8733–8743.

Jarvis, G. and McKenzie, D. (1980). Convection in compressible fluid with infinite Prandtl number. *J. Fluid Mech.*, 96:515–583.

Latour, J., Spiegel, E., Toomre, J., and Zahn, J.-P. (1976). Stellar convection theory. I. The anelastic modal equations. *Ap. J.*, 207:233–243.

Limaye, S. (1986). Jupiter: New estimates of the mean zonal flow at the cloud level. *Icarus*, 65:335–352.

Lorenz, R. (1999). Speed of sound in outer planet atmospheres. *Planet. Space Sci.*, 47:67–77.

Miesch, M., Elliott, J., Toomre, J., Clune, T., Glatzmaier, G., and Gilman, P. (2000). Three-dimensional spherical simulations of solar convection.I.Differential rotation and pattern evolution achieved with laminar and turbulent states. *Astrophys. J.*, 532:593–615.

Nellis, W., Weir, S., and Mitchell, A. (1999). Minimum metallic conductivity of fluid hydrogen at 140GPa (1.4 Mbar). *Phys. Rev. B*, 59:3434–3449.

Ogura, Y. and Phillips, N. (1962). Scale analysis of deep and shallow convection in the atmosphere. *J. Atmos. Sci.*, 19:173–179.

Orszag, S. (1971). Numerical simulation of incompressible flows within simple boundary conditions: accuracy. *J. Fluid Mech.*, 49:75–112.

Reif, F. (1967). *Statistical Physics - Berkeley Physics Course*, volume 5. McGraw-Hill.

Roberts, P. (1968). On the thermal instability of a self-gravitating fluid sphere containing heat sources. *Philos. Trans. R. Soc. London Ser. A*, 263:93–117.

Saumon, D., Chabrier, G., and Van Horn, H. (1995). An equation of state for low-mass stars and giant planets. *Astrophys. J. Suppl. Ser.*, 99:713–741.

Saumon, D. and Guillot, T. (2004). Shock compression of deuterium and the interiors of Jupiter and Saturn. *Astrophys. J.*, 609:1170–1180.

Schmeling, H. (1989). Compressible convection with constant and variable viscosity: the effect on slab formation, geoid, and topography. *J. Geophys. Res.*, 94:12,463–12,481.

Simitev, R. and Busse, F. (2003). Patterns of convection in rotating spherical shells. *New J. Phys.*, 5:1.1–1.20.

Smith, B., Soderblom, L., Batson, R., Bridges, P., Inge, J., Masursky, H., Shoemaker, E., Beebe, R., Boyce, J., Briggs, G., Bunker, A., Collins, S.A. Hansen, C. J. T., Mitchell, J., R., T., Cook II, A., Cuzzi, J., Pollack, J., Danielson, G.E. Ingersoll, A., Davies, M., Hunt, G., Morrison, D., Owen, T., Sagan, C., Veverka, J., Strom, R., and Suomi, V. (1982). A new look at the Saturn system: The Voyager 2 images. *Science*, 215:504–537.

Smith, B., Soderblom, L., Beebe, R., Boyce, J., Briggs, G., Bunker, A., Collins, S.A. Hansen, C. J. T., Mitchell, J., R., T., Carr, M. Cook II, A., Cuzzi, J., Pollack, J., Danielson, G.E. Ingersoll, A., Davies, M., Hunt, G., Masursky, H., Shoemaker, E., Morrison, D., Owen, T., Sagan, C., Veverka, J., Strom, R., and Suomi, V. (1981). Encounter with Saturn: Voyager 1 imaging science results. *Science*, 212:163–190.

Starchenko, S. and Jones, C. (2002). Typical velocities and magnetic fields strengths in planetary interiors. *Icarus*, 157:426–435.

Steinbach, V., Hansen, U., and Ebel, A. (1989). Compressible convection in the Earth's mantle: a comparison of different approaches. *Geophys. Res. Lett.*, 16:633–636.

Steinbach, V. and Yuen, D. (1998). The influence of surface temperature on upwellings in planetary convection with phase transitions. *Earth Planet. Sci. Lett.*, 162:15–25.

Stevenson, D. (1982). Interiors of the giant planets. *Ann. Rev. Earth Planet. Sci.*, 10:257–295.

Stevenson, D. and Salpeter, E. (1977). The phase diagram and transport properties for hydrogen-helium fluid planets. *Astrophys. J. Suppl.*, 35:221–237.

Sun, Z.-P., Schubert, G., and Glatzmaier, G. (1993). Transitions to chaotic thermal convestion in a rapidly rotating spherical shell. *Geophys. Astrophys. Fluid Dynamics*, 69:95–131.

Tilgner, A. (1999). Spectral methods for the simulation of incompressible flows in spherical shells. *Int. J. Numer. Math. Fluids*, 30:713–724.

Tilgner, A. and Busse, F. (1997). Finite-amplitude convection in rotating spherical fluid shells. *J. Fluid Mech.*, 332:359–376.

Tritton, D. (1988). *Physical Fluid Dynamics.* Clarendon Press, Oxford, 2nd. edition.

Williams, G. (1985). Jovian and comparative atmospheric modelling. *Adv. Geophys.*, 28A:281–349.

Yano, J.-I. (1992). Asymptotic theory of thermal convection in rapidly rotating systems. *J. Fluid Mech.*, 243:103–131.

Zhang, K. (1991). Convection in a rapidly rotating spherical shell at infinite Prandtl number: steadily drifting rolls. *Phys. Earth Planet. Int.*, 68:156–169.

Zhang, K. (1992a). Convection in a rapidly rotating spherical shell at infinite Prandtl number: transition to vacillating flows. *Phys. Earth Planet. Int.*, 72:236–248.

Zhang, K. (1992b). Spiralling columnar convection in rapidly rotating spherical fluid shells. *J. Fluid Mech.*, 236:535–556.

Zhang, K. (1993). On equatorially trapped boundary inertial waves. *J. Fluid Mech.*, 248:203–217.

Zhang, K. (1994). On coupling between Poincaré equation and the heat equation. *J. Fluid Mech.*, 268:211–229.

Zhang, K. (1995). On coupling between Poincaré equation and the heat equation: non-slip boundary condition. *J. Fluid Mech.*, 284:239–256.

Zhang, K. and Busse, F. (1987). On the Onset of Convection in Rotating Spherical Shells. *Geophys. Astrophys. Fluid Dynamics*, 39:119–147.

Zhang, K. and Jones, C. (1993). The influence of Ekman boundary layers on rotating convection. *Geophys. Astrophys. Fluid Dynamics*, 71:145–162.

Acknowledgements

Little by little, one travels far.

J.R.R. Tolkien

First of all I would like to thank my supervisor, Prof. Dr. Ulrich Christensen, who gave me the opportunity to be part of this project and patiently supported my work. It has been an enriching experience which increased my knowledge about Earth and expanded my horizons beyond Earth.

I would like to thank Prof. Dr. Andreas Tilgner who kindly accepted to referee this work as well as Prof. Dr. Wolfgang Glatzel, Prof. Dr. Stefan Dreizler, Prof. Dr. Dirk Ronneberger and Prof. Dr. Wolfram Kollatschny who gave their contribution as members of the examining board.

I am deeply grateful to Dr. Johannes Wicht who was always there to help me solving problems of any kind. Specially in the last stage of this work, when everything seemed to be "black", you helped without being asked, with many hours of priceless discussions, suggestions and comments. The structure of this thesis benefited a lot from your careful reading. Thank you very much, Johannes!

Special thanks to Dr. Julien Aubert for giving me many good hints during my work. Particularly, the linearisation of the compressible code significantly eased the calculations of the onset of convection.

Many thanks to Dr. Alexander Gatzemeier for countless discussions, help with LaTeX, spelling correction of the manuscript, administration problems ... and the list continues.

Thanks a lot to Dr. Carsten Kutzner, Monika Buske and Robert Olejniczak for the help during my first steps of the work and afterwards. My office-mates at the Max-Planck-Institut für Sonnensystemforschung, Monika Buske and Alina Semenova, had to endure many moments of distress in the last period of the thesis. Thank you girls for the support and the nice time we had.

I would like to thank Dr. Dieter Schmitt, coordinator of the Research School, for organising regular seminars and retreats, and giving all the students in the program the great opportunity to learn a lot about other topics.

An Frau Karin Peschke möchte ich “Danke schön” sagen für ihre immer freundliche Hilfe bei vielen Kleinigkeiten, die eventuell “Grossigkeiten” hätten werden können. Thanks to the staff at the GWDG in Göttingen as well as the staff of the computer centre at the Max-Planck-Institut für Sonnensystemforschung in Katlenburg-Lindau and Ulrich Einecke at the Institut für Geophysik in Göttingen for doing a great job in keeping the systems well running.

Las vueltas de la vida me han traído a otras latitudes, pero la distancia no siempre aleja. A muchas personas les quisiera decir muchas gracias por estar a mi lado.

A mi papá y a Susana les debo mi educación universitaria sin la cual ahora no estaría aquí. Infinitas gracias por el apoyo incondicional y constante en esta nueva etapa, desde las palabras de aliento hasta las encomiendas de alfajores.

Gracias a mi mamá por la atención periódica y los buenos consejos sobre todo en la última etapa. A mi Tío Santiago gracias por las llamadas telefónicas dominicales, que en los primeros meses del doctorado en un país extranjero fueron una inyección de energía.

A Verónica y a Severin, gracias por el apoyo y entusiasmo por mi trabajo, el cual no declinó a pesar de mis largos relatos contando los lentos avances de mi tesis en medio de los miles de escollos.

A mis amigos en Argentina y en el resto del mundo, gracias por el aguante.

An Waltraud und Friedel ein riesiges “Danke schön” für eure Hilfe in allen Lebenslagen. Ihr wart immer für mich da und habt dafür gesorgt, dass mir die Decke nicht auf den Kopf fällt ... Es hat schon geklappt.

To Alex, for believing in me, for being always there for me, walking the fascinating roads of life with me. For the moments we shared and for the ones to come ...
New adventures are waiting for us!

Lebenslauf

Persönliche Daten

Name: Denise Aida Tortorella
Geburtsdatum: 26. Januar 1972
Geburtsort: Buenos Aires, Argentinien
Staatsangehörigkeit: argentinisch

Schulbildung

03/1978-12/1979	Grundschule Gregoria Pérez, Buenos Aires
03/1980-12/1981	Grundschule Cornelia Pizarro, Buenos Aires
03/1982-12/1983	Grundschule Juan Larrea, Buenos Aires
03/1984-12/1984	Grundschule Provincia de La Pampa, Buenos Aires
03/1985-12/1989	Handelsschule N° 17, Santa María de los Buenos Aires, Buenos Aires. Abschluss: Perito Mercantil

Studium

03/1990-09/2000	Physikstudium an der *Facultad de Ciencias Exactas y Naturales*, *Universidad de Buenos Aires*
03/1999-09/2000	Diplomarbeit am physikalischen Institut der *Facultad de Ciencias Exactas y Naturales*, *Universidad de Buenos Aires* Thema: "Electrical modelling of a magmatic chamber", in Spanisch
09/2000-10/2001	Wissenschaftlicher Mitarbeiter am physikalischen Institut der *Facultad de Ciencias Exactas y Naturales*, *Universidad de Buenos Aires*
10/2001-05/2003	Wissenschaftlicher Mitarbeiter am Institut für Geophysik, Universität Göttingen
05/2003-06/2005	Wissenschaftlicher Mitarbeiter am Max-Planck-Institut für Sonnensystemforschung, Katlenburg-Lindau
10/2001-06/2005	Doktorarbeit mit dem Thema: "Numerical studies of thermal and compressible convection in rotating spherical shells: an application to the giant planets"